

The Measurement and the Monitoring of the Central Hemodynamics using Non-invasive and Minimally-Invasive Data

by

Mande Tak Man Leung

B.Sc., The University of Alberta, 2004

A THESIS SUBMITTED IN PARTIAL FULFILLMENT OF
THE REQUIREMENTS FOR THE DEGREE OF

DOCTOR OF PHILOSOPHY

in

The Faculty of Graduate Studies

(Electrical and Computer Engineering)

THE UNIVERSITY OF BRITISH COLUMBIA

(Vancouver)

June 2011

© Mande Tak Man Leung 2011

Abstract

According to the World Health Organization (WHO), cardiovascular (CV) diseases are the number one cause of death globally, and are projected to remain the single leading cause of death by 2030. Central pulse pressure and several arterial stiffness indices, especially aortic pulse wave velocity (PWV), are among the strongest predictors of CV events, including stroke, myocardial infarction (heart attack) and angina (chest pain). Therefore, non-invasive methods for the assessment of the central pressure and central arterial stiffness are very important for the diagnosis of CV diseases at their early stage of development.

In this thesis, non-invasive methods are developed to (i) measure the aortic PWV, and (ii) measure the aortic pressure waveform (APW).

In the intensive care unit, cardiac output (CO) is an important measure of the adequacy of circulation among post-operative patients of cardiovascular diseases. Current methods of monitoring use the heart rate, peripheral blood pressure, and urine output as surrogates of CO, but these indices are inadequate. CO can be monitored directly using thermodilution but the procedure is highly invasive.

In this thesis, a minimally-invasive method is developed to monitor the CO using the radial artery pressure waveform.

The underlying algorithms of the methods developed in this thesis are interrelated. In this thesis, the arterial system is modeled as a single uniform lossless transmission line terminated by a complex load. Each measuring and monitoring task is a problem of identification, simulation or data acquisition.

The measurement of the aortic PWV is formulated as an identification problem. The method developed in this thesis was shown to be able to differentiate a group of children with Marfan syndrome from the healthy children.

The monitoring of CO is formulated as a problem of identification and simulation. The method developed in this thesis was applied to five post-surgical infants. It showed clinically acceptable agreement with the more established echocardiographic technique.

The measurement of APW is a problem of data acquisition. A method

was developed to estimate APW from the aortic distension waveform obtained using B-mode ultrasound. This method showed good agreement with carotid artery applanation tonometry when applied to nine healthy children.

Preface

This thesis is based on several manuscripts, resulting from collaboration between multiple researchers.

A version of Chapter 2 has been submitted. This paper was co-authored with Prof Guy Dumont, Dr George Sandor and Dr James Potts. The author's contribution was developing the idea, numerical implementation, processing the raw echocardiographic data and tonometric data, algorithm evaluation, comparing results between the normal subjects and diseased subjects, and preparing the manuscript. Prof Dumont assisted with his insight on the identification technique and optimization algorithm, and edited the manuscript. Dr. Sandor assisted with his insight on the potential clinical use of the technique and processed the echocardiographic data. Dr. Potts provided his expertise on statistics for medical research.

A version of Chapter 3 has been submitted. This paper was co-authored with Prof Guy Dumont, Dr George Sandor and Dr James Potts. The author's contribution was developing the idea, numerical implementation, collecting radial artery pressure data in the intensive care unit, developing a software for data extraction in the intensive care unit, processing the raw echocardiographic and pressure data, algorithm evaluation using simulated data, technique evaluation using data collected from human subjects in the intensive care unit, and preparing the manuscript. Prof Dumont assisted with his insight on the identification technique, suggested reviews on other recently developed similar techniques and edited the manuscript. Dr. Sandor assisted with his insight on the potential clinical use of the technique, assisted with subject selections, evaluated the conditions of the subjects prior to and during data collection, commented on the performance of the technique in a clinical setting. Dr. Potts provided his expertise on statistics for medical research.

A version of Chapter 4 is under preparation for submission. This paper was co-authored with Prof Guy Dumont, Dr George Sandor and Dr James Potts. The author's contribution was developing the idea, numerical implementation, processing the raw echocardiographic data and tonometric data, comparing the proposed technique with the more established tonometric

technique, and preparing the manuscript. Prof Dumont assisted with his insight on the mathematical aspect of the technique. Dr. Sandor assisted with his insight on the potential clinical use of the technique. Dr. Potts provided his expertise on statistics for medical research.

A version of Chapter 2 was accepted and presented as

- M. Leung, G. A. Dumont, J. E. Potts, M. T. Potts and G. G. S. Sandor, “A model-based method to estimate pulse wave velocity,” 11th World Congress of Medical Physics and Biomedical Engineering, Munich, Germany, 2009

Another version of Chapter 2 was accepted and presented as

- M. Leung, G. A. Dumont, G. G. S. Sandor and J. E. Potts, “Estimating arterial stiffness using transmission line model,” 28th IEEE Engineering in Medicine and Biology Conference, New York, 2006

A version of Chapter 4 was accepted and presented as

- M. Leung, G. A. Dumont, G. G. S. Sandor, M. T. Potts and J. E. Potts, “A novel method to estimate the aortic pressure waveform using B-mode ultrasound images acquired from a suprasternal view,” 30th IEEE Engineering in Medicine and Biology Conference, Vancouver, 2008

The data collection for the studies presented in Chapter 2 and Chapter 4 was approved by the University of British Columbia Children’s and Women’s Research Ethics Board. The certificate number is H07-01816. The data collection for the study presented in Chapter 3 was approved by the University of British Columbia Children’s and Women’s Research Ethics Board. The certificate number is H06-038876.

Table of Contents

Abstract	ii
Preface	iv
Table of Contents	vi
List of Tables	x
List of Figures	xi
Abbreviations and Symbols	xiii
Dedication	xviii
1 Introduction	1
1.1 Motivation	1
1.2 Background	3
1.2.1 The mechanism of the pressure and flow waves in the arterial system	3
1.3 Literature review	5
1.3.1 Current non-invasive methods to measure the central pressure waveform	5
1.3.2 Current non-invasive methods to measure aortic pulse wave velocity	8
1.3.3 Current methods to monitor cardiac output	11
1.4 Thesis objectives	14
2 Model-based Aortic Pulse Wave Velocity^{1,2,3}	17
2.1 Introduction	18
2.2 Methods	20
2.2.1 Outline of the model parameter identification algorithm	20

2.2.2	Estimations of the line inductance and the terminating resistance	21
2.2.3	Initial values of the line capacitance, the load capacitance and the line length	21
2.2.4	Estimation of the load resistance	22
2.2.5	Performance index	22
2.2.6	Calculation of the model-based pulse wave velocity	24
2.3	Experiments	24
2.3.1	Data acquisition and processing	24
2.4	Results	27
2.5	Discussion	35
2.5.1	Ability to differentiate the subjects with Marfan syndrome from the healthy subjects	35
2.5.2	Correlations between the pulse wave velocities obtained by different methods	35
2.5.3	Interchangeability between the pulse wave velocities obtained by different methods	36
2.5.4	Performance of the model in predicting ascending aortic flow	36
2.5.5	Large artery compliance to small artery compliance ratio	36
2.6	Conclusions	37
3	Monitoring Cardiac Output using Grey-Box Identification on a State-Space Representation of the Transmission Line Model¹	38
3.1	Introduction	39
3.2	Methods	42
3.2.1	Derivation of the state-space representation of the transmission line model	42
3.2.2	Physiological ranges of the physical model parameters	46
3.2.3	Local identifiability of the proposed state-space model	47
3.2.4	Grey-box identification	50
3.2.5	Estimation of the bias and variance using a Monte-Carlo study	54
3.2.6	Performance of the proposed grey-box identification method using simulated data	55
3.2.7	Estimation of the cardiac output from the radial artery pressure waveform	57
3.3	Experiments	64

3.3.1	Data acquisition	64
3.3.2	Data processing	64
3.3.3	Cardiac output determination	66
3.4	Results	68
3.5	Discussion	70
4	Measuring Aortic Pressure Waveform using Ultrasound B-Mode Imaging^{1,2}	75
4.1	Introduction	75
4.2	Methods	78
4.2.1	Adaptive block matching	78
4.2.2	Gradient-based edge refining	80
4.2.3	Weighted total least-squares fitting	81
4.2.4	Continuity of the aortic wall motion	83
4.2.5	Choosing a cross-section along the arch	83
4.2.6	Estimating the pressure waveform from the distension waveform	83
4.3	Experiments	84
4.3.1	Data acquisition and processing	84
4.3.2	Calibration of the carotid artery pressure waveform obtained using applanation tonometry	85
4.3.3	Comparison of waveforms	85
4.3.4	Calculations of pulse pressure, augmentation index and total arterial compliance	85
4.4	Results	86
4.4.1	Waveform comparisons	87
4.4.2	Comparisons of pulse pressures, augmentation indices and total arterial compliances	87
4.5	Discussion	89
4.6	Conclusion and future work	94
5	Conclusions and Future Work	96
5.1	Contributions	96
5.1.1	Model-based estimation of the aortic pulse wave velocity	96
5.1.2	Minimally-invasive monitoring of the cardiac output	97
5.1.3	Estimation of the aortic pressure waveform using B-mode imaging	99
5.1.4	Suggestions for future work	99

References	101
-----------------------------	-----

Appendices

A The Analogy between a Transmission Line and an Elastic Tube with Incompressible Flow	121
B Implementation of the Transmission Line Model using the Finite Element Method	123
C The Derivation of the Transfer Function from the Ascending Aortic Flow to the Radial Artery Pressure	125

List of Tables

2.1	Clinical characteristics of the subjects of the pulse wave velocity study	28
2.2	Fixed model parameters and initial model parameters	28
2.3	Identified model parameters using white box identification	29
2.4	Pulse wave velocity measured using different methods	29
2.5	Correlations between the echocardiographic pulse wave velocity and different model-based pulse wave velocities	30
2.6	Performance of the transmission line model in predicting the aortic flow	30
3.1	Physiological ranges of the transmission line model parameters	48
3.2	The number of stable models for different time steps and numbers of elements	51
3.3	The estimated bias and variances of the grey-box identification method	56
3.4	Model parameters estimated from the simulated data	58
3.5	Stability of the models identified from the simulated data	59
3.6	Demographics of patients of the cardiac output monitoring project	68
3.7	Identified transmission line model parameters	69
3.8	Cardiac output determinations	70
3.9	Bias and limits of agreement in terms of % error	70
3.10	Bias and limits of agreement in terms of cardiac output	71
3.11	Bias and limits of agreement in terms of cardiac index	71
4.1	Demographics of subjects of the aortic pressure waveform project	86
4.2	Comparisons of the waveforms obtained using applanation tonometry and B-mode imaging in the frequency domain	88
4.3	Comparisons of the derived pulse pressures, augmentation indices and total arterial compliances	90

List of Figures

1.1	The overall objectives	14
2.1	A single uniform transmission line terminated by a complex load	19
2.2	The calculation of the total arterial compliance	23
2.3	The model-predicted ascending aortic flow	25
2.4	Noninvasive data collection of the model-based pulse wave velocity	26
2.5	Box and whisker plots for the model-based pulse wave velocity and echocardiographic pulse wave velocity	31
2.6	Correlation between the model-based pulse wave velocity and echocardiographic pulse wave velocity	32
2.7	Bland-Altman plot of the model-based pulse wave velocity and echocardiographic pulse wave velocity	33
2.8	A sample of the model-predicted ascending aortic flow waveform and the corresponding experimentally-measured ascending aortic flow waveform	34
3.1	A lossless transmission line terminated by a complex load . .	40
3.2	The indexing for the current and the voltage in the finite element representation	43
3.3	The grey-box identification algorithm	54
3.4	The simulated flow waveform used as the input to the transmission line model	60
3.5	The estimated radial artery pressure waveform using simulated flow as the model input	61
3.6	The re-estimation of the terminating resistance	61
3.7	The determination of the time constant of the Windkessel load using the area method	62
3.8	The cardiac output estimation technique	65
3.9	The estimation of the left ventricular outflow tract flow from the Doppler spectrum	66

3.10	A sample of the radial artery pressure waveform	67
3.11	A sample of the measured ascending aortic flow waveform . .	67
3.12	Log of singular value versus system order	69
3.13	Covergence graphs	71
3.14	Bland-Altman plot of the cardiac output determinations . . .	72
3.15	Measured and estimated ascending aortic flow waveforms . .	73
4.1	Block selections for the block matching scheme	78
4.2	Search of the best-matching block	79
4.3	The adaptive block matching scheme	80
4.4	Refining the edges using the gradient of the intensity	81
4.5	Weight assigning scheme for fitting a second degree polyno- mial to the edge	82
4.6	Comparisons of the waveforms obtained using applanation tonometry and B-mode imaging I	91
4.7	Comparisons of the waveforms obtained using applanation tonometry and B-mode imaging II	92

Abbreviations and Symbols

Chapter 2

AAF (cm^3/s)	Ascending aortic flow
AAP (mmHg)	Ascending aortic pressure
BSA (m^2)	Body surface area
MFS	Marfan syndrome
PTT (ms)	Pulse transit time
PWV (cm/s)	Pulse wave velocity
RMSE (cm^3/s)	Root-mean-squared error
TAC (cm^3/mmHg) ...	Total arterial compliance
DP (mmHg)	Diastolic pressure at the brachial artery
MP (mmHg)	Mean arterial pressure
SP (mmHg)	Systolic pressure at the brachial artery
C ($\text{cm}^3/\text{mmHg}/\text{cm}$) ..	Transmission line model unit line capacitance
C_L (cm^3/mmHg)	Transmission line model load capacitance
C_T (cm^3/mmHg)	Transmission line model total capacitance, sum of total line capacitance and load capac- itance
L ($\text{mmHg}\cdot\text{s}^2/\text{cm}^3/\text{cm}$) .	Transmission line model unit line inductance
R_L ($\text{mmHg}\cdot\text{s}/\text{cm}^3$)	Transmission line model load resistance
R_T ($\text{mmHg}\cdot\text{s}/\text{cm}^3$)	Transmission line model terminating resis- tance
l (cm)	Transmission line model line length
A_{ao} (cm^2)	Ascending aortic cross-sectional area
J (cm^6/s)	Performance index
P (mmHg)	Pressure
Q (cm^3/s)	Flow

$Q_{ao,e}$ (cm ³ /s)	Experimentally-measured ascending aortic positive flow
$Q_{ao,m}$ (cm ³ /s)	Model-predicted ascending aortic positive flow
ρ_b (mmHg s ² /cm ²)	Blood density
μ	Penalty coefficient of the performance index
Λ (cm ⁶ /s)	Penalty term of the performance index

Chapter 3

AAF (cm ³ /s)	Ascending aortic flow
AL (L)	Area integral of the model-estimated ascending aortic flow waveform
CO (L/min)	Cardiac output
D (min)	Duration of the model-estimated ascending aortic flow waveform in one cardiac cycle
ICU	Intensive care unit
LVOT (cm)	Left ventricular outflow tract
PAP (mmHg)	Peripheral artery pressure
RAP (mmHg)	Radial artery pressure
SS	State-space
TAC (cm ³ /mmHg) ...	Total arterial compliance
C (cm ³ /mmHg/cm) ..	Transmission line model unit line capacitance
C_L (cm ³ /mmHg)	Transmission line model load capacitance
C_{tot} (cm ³ /mmHg)	Transmission line model total line capacitance
L (mmHg s ² /cm ³ /cm) .	Transmission line model unit line inductance
L_{tot} (mmHg s ² /cm ³) ..	Transmission line model total line inductance
R_L (mmHg/cm ³)	Transmission line model load resistance
R_T (mmHg/cm ³)	Transmission line model terminating resistance
Z_{ch} (mmHg/cm ³)	Transmission line model characteristic impedance of the line
l (cm)	Transmission line model line length
C_{wind} (cm ³ /mmHg) ..	Windkessel model capacitance
τ (s)	Windkessel model time constant

$\mathbf{A}(\theta), \mathbf{B}(\theta), \mathbf{C}(\theta) \dots\dots$	Physical state-space model
$\hat{\mathbf{A}}, \hat{\mathbf{B}}, \hat{\mathbf{C}} \dots\dots\dots$	Empirical state-space model
$\mathbf{T} \dots\dots\dots$	Transformation matrix between the physical state-space model and the empirical state-space model
$e \dots\dots\dots$	Error between the physical state-space model and the empirical state-space model
$A_1, A_2 \dots\dots\dots$	Parameters of the state-space transmission line model
$I_j \dots\dots\dots$	Current at the j th node of the finite element transmission line
$K_1, K_2, K_3, K_4 \dots\dots\dots$	Parameters of the state-space transmission line model
$M \dots\dots\dots$	Transfer function from the ascending aortic flow to the radial artery pressure
$V_j \dots\dots\dots$	Voltage at the j th node of the finite element transmission line
$d \dots\dots\dots$	Discrete-time delay from the ascending aortic flow to the radial artery pressure
$n \dots\dots\dots$	Discrete time variable
$p - 1 \dots\dots\dots$	Number of elements of the finite element transmission line
$t \dots\dots\dots$	Continuous time variable
$x \dots\dots\dots$	Continuous spatial variable
$\Phi_c \dots\dots\dots$	Voltage across C_L
$\Delta t \dots\dots\dots$	Time step
$\alpha \dots\dots\dots$	Parameter of the state-space transmission line model
$\beta \dots\dots\dots$	Correction factor between the model-estimated cardiac output and echocardiographic-measured cardiac output
$\varphi \dots\dots\dots$	Vector of unknown physical model parameters
$\mu \dots\dots\dots$	Propagation velocity of the transmission line
$\theta \dots\dots\dots$	Vector of unknown parameters of the state-space transmission line model
$\psi \dots\dots\dots$	Vector of known parameters of the state-space transmission line model

Chapter 4

AI (%)	Augmentation index
PP (mmHg)	Pulse pressure
RMSD (mmHg)	Root-mean-squared difference
TAC (cm ³ /mmHg) ...	Total arterial compliance
DP (mmHg)	Diastolic pressure at the brachial artery
MP (mmHg)	Mean arterial pressure
SP (mmHg)	Systolic pressure at the brachial artery
$A(t)$ (cm ²)	Time function of the cross-sectional area of the ascending aorta
A_0 (cm ²)	Cross-sectional area at the reference pressure
D (cm)	Diameter of the ascending aorta
$P(t)$ (mmHg)	Time function of the ascending aortic pressure
P_0 (mmHg)	Reference pressure
P_a (mmHg)	Pressure calculated from the exponential pressure-area relationship
P_{dw} (mmHg)	Pressure waveform obtained from the distension waveform
P_{exp} (mmHg)	Pressure waveform obtained from the distension waveform using exponential calibration
P_{inf} (mmHg)	Pressure at the inflection point
P_{lin} (mmHg)	Pressure waveform obtained from the distension waveform using linear calibration
P_{max} (mmHg)	Maximum pressure
P_{tono} (mmHg)	Pressure waveform obtained using applanation tonometry
R_P (mmHg/cm ³)	Peripheral resistance
cr	Correlation between the kernel block and the candidate block in block matching
cv	Curvature of the second degree polynomial fit
k	Size of the kernel block in block matching
s	Size of the search region in block matching
vx	x -coordinate of the second degree polynomial fit

vy	y -coordinate of the second degree polynomial fit
β	Threshold of discrepancy in the gradient-based edge refining scheme
φ	Threshold of distance in the weighted total least-squares fitting scheme
γ	Threshold of correlation in the adaptive block matching scheme
θ	Threshold of the number of neighborhood points in the weighted total least-squares fitting scheme

To my mum

Chapter 1

Introduction

1.1 Motivation

According to the World Health Organization (WHO), cardiovascular diseases are the number one cause of death globally, and are projected to remain the single leading cause of death by 2030. Central pressure and arterial stiffness have strong association with the pathogenesis of the cardiovascular diseases [1].

Central arteries are proximal to the heart and include the aorta and the carotid artery while peripheral arteries are distal to the heart and include the arteries at the limbs, such as the radial, brachial and femoral arteries. Although brachial pulse pressure has long been recognized as a powerful predictor of cardiovascular events [103,113], it has recently been shown that central pulse pressure has stronger association with the severity of coronary artery disease than brachial pulse pressure [168], and is a powerful independent predictor of all-cause, including cardiovascular, mortality in end-stage renal diseases [136]. In addition, it has also been suggested that central pressure may have predictive value independent of the corresponding brachial pressure [1]. Therefore, there is an increasing interest in the measurement of central pressure.

However, central hemodynamics are more difficult to assess than the peripheral hemodynamics. Aortic pressure can be measured by advancing a catheter through the brachial artery or the femoral artery to the aorta, but such procedure is highly invasive. In contrast, pressure at the superficial arteries, including carotid, radial and femoral arteries, can be measured non-invasively using applanation tonometry.

It has been suggested that carotid artery pressure obtained using applanation tonometry can be used as a surrogate of aortic pressure [82]. However, the procedure requires substantial expertise. In addition, the aortic pressure and the carotid artery pressure are not identical due to difference in location, and the difference may become significant in case of carotid artery diseases, such as carotid stenosis. In this thesis, a new method is developed to measure the aortic pressure using B-mode imaging. This method estimates the

aortic pressure waveform using B-mode images of the aortic arch, which can be obtained during routine echocardiographic exam, and therefore does not require any special equipment or training. It is applicable to patients with carotid diseases. Since this method is non-invasive, it can be used in early detection of cardiovascular diseases in the general population.

Aortic pulse wave velocity is the most well-accepted index of arterial stiffness. It has been shown that aortic pulse wave velocity is an independent predictor of all-cause and cardiovascular mortality in hypertensive patients [92], cardiovascular mortality in subjects over 70 years of age [109], and cardiovascular events in different populations [19,93,154]. The most common method to estimate the aortic pulse wave velocity is to measure the pressure pulses at the carotid and femoral arteries, and calculate the aortic pulse wave velocity as the distance between the measuring sites divided by the pulse transit time. This method requires high precision of the measurement of the pulse transit time. The distance is measured on the surface of the skin and may be inaccurate in subjects with large busts or abdominal obesity. In this thesis, a non-invasive, model-based method is developed to measure the aortic pulse wave velocity. This new method does not require pulse transit time or distance measurement. Since this method is non-invasive, it can be used in early detection of cardiovascular diseases in the general population.

The modelling approach has been used by previous researchers to estimate the stiffness of the central arteries. The most commonly used model to represent the arterial system is the two-element Windkessel [119]. The two-element Windkessel model is simple and captures the two most important mechanical properties of the arterial system: compliance and resistance. However, the Windkessel model is a lumped model and has two related limitations. First, it implies that pulse wave velocity is infinite. Second, it cannot capture the wave propagation and reflection characteristics in the arterial system. Wave reflection is an important phenomenon in the arterial system and is related to the pathogenesis of the cardiovascular diseases [1]. The transmission line model is distributive and is a more suitable model for the arterial system [94]. It is one of the motivations of this thesis to use the more accurate transmission line model to estimate the stiffness of the central arteries.

Non-invasive methods to measure the central pressure and arterial stiffness are important as they are valuable tools for the diagnosis of cardiovascular diseases at their early stage of development. Invasive measurement methods are associated with significant risk and are not always justifiable. Non-invasive methods are also useful for large-scale, cross-sectional studies.

Cardiac output indicates the performance of the heart as a pulsatile

pump [127]. It has been shown that the cardiac index in postoperative patients is associated with their survival rate [18,40]. The monitoring of cardiac output is therefore essential during perioperative care. Cardiac output can be measured using thermodilution, which is often performed with a pulmonary artery catheter. The placement of a pulmonary artery catheter is associated with increased mortality and increased utilization of resources [34]. A less invasive alternative is much desired.

Cardiac output can be measured using transthoracic Doppler ultrasound, but the procedure requires a well-trained operator, and therefore is not suitable for long-term continuous monitoring. In contrast, the radial artery pressure can be monitored continuously using an indwelling catheter and the procedure is minimally invasive. Therefore, in this thesis, a new technique is developed to monitor the cardiac output using the radial artery pressure waveform. This technique can be applied to post-operative patients during their stay at the intensive care unit.

The estimation of the cardiac output using the radial artery pressure waveform is termed pulse contour analysis. One of the most popularly used pulse contour analyses is Wesseling's algorithm [172], which is based on the a simplified transmission line model. According to Wesseling's transmission line model, the aortic flow and the aortic pressure are directly proportional and are related by the characteristic impedance of the line. However, aortic flow is instead directly proportional to the difference between the forward aortic pressure and the backward aortic pressure. As presented in Section 1.3.3, Wesseling's algorithm uses only the area of the systolic portion of the pressure waveform to estimate the cardiac output. In addition, in Wesseling's algorithm, the radial artery pressure is used as a surrogate of aortic pressure. It is one of the motivations of this thesis to develop a cardiac output estimation technique based on a more precise transmission line model.

1.2 Background

1.2.1 The mechanism of the pressure and flow waves in the arterial system

The cardiovascular system can be divided into two major components, the heart and the vasculature. While the heart is a muscular pump, the vasculature is a network of vessels, which consists of the arteries, the capillaries and the veins. Blood runs from the ventricles of the heart, through the arteries, the capillaries and the veins, and back to the atria of the heart. Since the heart operates as an intermittent pump, the pressure and flow waves

entering the arteries have a oscillating component and a steady component. The oscillating component is gradually eliminated in the arterial system, and only the steady component enters the capillaries.

The arteries form a network of progressively branching, geometrically and elastically tapering viscoelastic tubes. The arterial network has two major functions, cushioning and conduiting. The arteries are compliant and are able to distend to accommodate the sudden increase in blood volume, thereby providing a cushioning function. The arteries then recoil slowly and push the volume of blood forward. There is a progressive loss of the cushioning function along the arterial network. The aorta and its major branches are referred to as the elastic arteries. The media of the elastic arteries are rich in elastic fibers. The elastic arteries gradually merge into the muscular arteries, and the muscular arteries gradually merge into the arterioles. The media of the muscular arteries is dominated by smooth muscle cells and has very few elastic fibers. From the elastic arteries to the resistive arterioles, the compliance of the arteries decreases gradually [119].

Pressure and flow waves propagate down the arterial network at a finite pulse wave velocity. During the propagation, wave reflections occur at various discontinuities and terminations, including the branching points and the resistive arterioles [121]. Theoretically, since the compliance and the cross-sectional area of the arteries are progressively changing, wave reflections occur at every point along the arterial network. However, it is believed that the major wave reflections occur at the resistance arteries, including the muscular arteries and the arterioles [1]. A direct consequence of wave reflections is pressure amplification from the central arteries to the peripheral arteries. The pressure wave recorded at any point along the arterial network is the sum of the incident wave and all the reflected waves. At the peripheral sites, the reflected wave augments the systolic portion of the incident wave. The reflected wave propagates from the peripheral site back to the central site and is gradually attenuated. At the central sites, the attenuated reflected wave augments the diastolic portion of the incident wave. The net result is that the pressure amplitude is higher at the peripheral site than the central site. This phenomenon is referred to as pressure amplification.

During systole, it is the aortic systolic pressure that the left ventricle encounters. Chronic sustained elevation of aortic systolic pressure causes left ventricular hypertrophy [122]. In young and healthy subjects, reflected wave augments the incident wave at the ascending aorta during diastole. In the case of arteriosclerosis, which is the degeneration of the arterial media, the arterial stiffness increases. According to the Moen- Korteweg equation, pulse wave velocity increases as arterial stiffness increases [119]. Because of

the increase in pulse wave velocity, the reflected wave arrives at the ascending aorta during systole and causes the aortic systolic pressure to increase. Arteriosclerosis occurs mainly in aging and hypertensive subjects [122]. Similarly, in the case of arterial or arteriolar constriction, where the reflection site is moved closer to the heart, the reflected wave augments the incident wave at the ascending aorta during systole causing aortic systolic pressure to increase.

In summary, the central pulse pressure, the aortic pulse wave velocity and the central arterial stiffness are interrelated and have strong influences on the pathogenesis of the cardiovascular diseases. Because of pressure amplification, peripheral pressure cannot be used as a surrogate of central pressure.

1.3 Literature review

1.3.1 Current non-invasive methods to measure the central pressure waveform

Carotid artery applanation tonometry

Arterial applanation tonometry is a technique for transcutaneous pressure recording. It is based on the principle that the force required to applanate an artery divided by the applanated area is equivalent to the intraluminal pressure. The principle of applanation tonometry was originally applied in ocular tonometry to measure the intraocular pressure. In 1963, Pressman and Newgard published the earliest work in arterial applanation tonometry [129]. Unlike sphygmomanometry, arterial applanation tonometry can measure the instantaneous blood pressure continuously and thereby provide the pressure waveform. The early development of arterial applanation tonometry was described in the review by Drzewiecki et al. [43]. In 1989, Kelly et al. [80] developed a tonometer consisting of a pencil-type probe incorporating a high-fidelity Millar gauge transducer, and it was shown that the tonometrically and intra-arterially measured radial artery pressure waveforms were similar. It was also shown that the morphology of the tonometrically measured carotid artery pressure waveform and that of the intra-arterially measured ascending aortic pressure waveform were similar [81].

During the early development of arterial applanation tonometry, researchers aimed to measure the absolute pressure. It is then regarded as possible only if stringent requirements of applanation are met [81]. External calibration can be applied to the brachial artery pressure waveform. The brachial systolic and diastolic pressures are measured at the arm using cuff

sphygmomanometer. The systolic pressure is assigned to the peak and the diastolic pressure is assigned to the trough of the waveform. For the radial artery, it is often assumed that the systolic and diastolic pressures at the brachial artery and the radial artery are the same. The same calibration is thus applied. However, because of pressure amplification, the same calibration scheme cannot be applied to the carotid artery.

Kelly et al. [82] proposed an external calibration method for the carotid artery. It is based on the assumption that the mean arterial pressure and the diastolic pressure remain constant through out the arterial tree. The brachial artery pressure waveform is measured using applanation tonometry and calibrated using a cuff sphygmomanometer. The mean arterial pressure is calculated as the area integral over the duration of the calibrated brachial artery pressure waveform. The mean arterial pressure is then assigned to the area integral over the duration of the carotid artery pressure waveform. The diastolic pressure is assigned to the trough of the carotid artery pressure waveform. It was shown that the calibrated, tonometrically measured carotid artery pressure waveform and the inter-arterially measured aortic pressure waveform were similar [82].

Carotid artery applanation tonometry has since become a popular choice to measure the central pressure waveform [7, 65, 101, 138, 167]. In some studies, a simplified calibration process was used [3, 128, 134]. The mean arterial pressure (MP) was calculated from the systolic pressure (SP) and diastolic pressure (DP) at the brachial artery using the traditional formula: $MP = \frac{1}{3}SP + \frac{2}{3}DP$ instead of the brachial artery pressure waveform.

The major limitation of carotid artery applanation tonometry is that the applanation of the carotid artery is difficult and requires substantial amount of expertise. The quality of the measured waveform is affected by the lateral and radial motions of the applanation force. The carotid artery is surrounded by loose tissue and is therefore not an ideal site for optimal applanation.

Radial artery applanation tonometry with a generalized transfer function

Comparing to the carotid artery, the radial artery is well-supported by bony tissue allowing optimal applanation to be achieved.

Because of pressure amplification, the pressure waveforms at the radial artery and the central arteries are very different in both morphology and magnitude. Radial artery pressure waveform can not be used as a surrogate of the central pressure waveform. Karamanoglu et al. [77] pro-

posed to use a generalized transfer function to reconstruct the aortic pressure waveform from the radial artery pressure waveform. The generalized transfer function is calculated as the average of the individual transfer functions from the ascending aortic pressure to the radial artery pressure of a group of subjects. Since then, the idea was explored by a number of studies [32,46,68,69,126]. Most of these studies derived a non-parametric transfer function [32,68,69] while one study also derived an ARX transfer function [46]. In these studies, the radial artery pressure waveform was measured either intra-arterially [126], or tonometrically with invasive calibration, in which the the mean and diastolic pressures of the radial artery and the aorta were matched [32,46,68,69]. This is to eliminate the error introduced by the cuff sphygmomanometer during the calibration of the radial artery pressure waveform. Three of these studies concluded that the generalized transfer function method is viable [32,46,126], while two were skeptical [68,69]. In the study by Hope et al. [68], it was shown that even though the mean error between the invasively-measured and the transfer-function-derived aortic systolic pressures was small, the error variance was large. It was pointed out that a generalized transfer function derived from a population mean would be expected to result in a small mean error in the estimation of the systolic pressure or other parameters, however, this does not demonstrate its validity on an individual basis. The large error variance indicated that the generalized transfer function may not be valid for each individual.

A commercial device, SphygmoCor (SphygmoCor; Atcor Medical, Sydney, Australia), estimates the aortic pressure waveform using the generalized transfer function method. A substantial amount of studies used this device to measure central pulse pressure and other central indices. However, the validity of the generalized transfer function method remains controversial [70]. A number of studies have shown that SphygmoCor cannot measure central pulse pressures with acceptable accuracy [33,37,147,149].

Distension waveform method

The relationship between the pressure waveform and the distension waveform of an artery is determined by the elastic properties of the arterial wall. In 1978, Ghista et al. [52] published the earliest theoretical analysis for the determination of the pressure waveform from the distension waveform. It was suggested that if several elasticity parameters are known, the pressure waveform can be calculated from the distension waveform. It was also indicated that high resolution for the measurement of the arterial diameter is required. The idea was not explored further for about twenty years, and it

was most likely due to the complexity in the determination of the elasticity parameters and the lack of accuracy in the measurement of the distension waveform. In 1998, Watanabe et al. [171] used an echo-tracking device to measure the aortic distension waveform, and a relatively simple exponential relationship between the pressure and the diameter to calculate the aortic pressure waveform. The echo-tracking device can provide a spatial resolution up to $20\text{ }\mu\text{m}$. However, the simple exponential relationship involves a stiffness parameter, and the study did not provide a method to accurately estimate this parameter. In 2001, Van Bortel et al. [161] used the echo-tracking device to measure the carotid distension waveform, and assumed a linear relationship between the pressure and the diameter. With carotid artery applanation tonometry as the reference method, the central pulse pressure obtained from the carotid distension waveform demonstrated good accuracy. In 2004, Meinders and Hoeks [110] used high frame rate B-mode images to measure the carotid distension waveform, and an exponential relationship between the pressure and the cross-section area of the artery to calculate the pressure waveform. The exponential relationship involves a stiffness parameter. An iterative scheme was proposed to find the stiffness parameter. It was assumed that the mean pressures at the brachial artery and the carotid artery were the same. The stiffness parameter was updated iteratively such that the mean pressure of the calibrated distension waveform matched that of the brachial artery. In 2008, Vermeersch et al. [166] used the echo-tracking device to measure the carotid distension waveform, and both linear and exponential calibration schemes to calculate the pressure waveform. It was shown that the exponential calibration scheme was superior to the linear calibration scheme, and good accuracy was achieved in the estimation of the carotid artery pressure waveform and pulse pressure.

Compared to applanation tonometry, the distension waveform method is relatively new and is not yet popularly used in clinical research for the measurement of the central pressure waveform.

1.3.2 Current non-invasive methods to measure aortic pulse wave velocity

Pulse wave velocity is often measured using the two-site method. The pulse wave is measured at two recording sites, and the pulse wave velocity is calculated as the distance between the sites divided by the time delay between the measured pulse waves. The time delay is often referred to as the pulse transit time. Pulse wave velocity can be obtained from the travel of the pressure wave, the flow wave or the distension wave. Aortic pulse wave velocity

is most commonly measured as the carotid-femoral pulse wave velocity.

In 1922, Bramwell and Hill [23] published the earliest clinical study on the measurement of the pulse wave velocity. The pressure waveforms at the carotid artery and the radial artery were measured simultaneously using the hot-wire sphygmograph. The pulse transit time was taken as the time interval elapsed between the commencements of the carotid and radial deflections displayed on the sphygmogram. The distance traveled was taken as the distance from the sterno-clavicular joint to the wrist, less the distance from the same point to the carotid artery. It should be noted that the pressure waveforms obtained using the sphygmograph in this study were quite different from the intra-arterially measured pressure waveforms in the literature. However, large deflections corresponded to the systolic upstrokes can be easily identified, and the pulse transit time was measured from the deflections. It should also be noted that this method measures the pulse wave velocity along the subclavian-radial pathway and does not measure the aortic pulse wave velocity.

In contrast to the carotid-radial pulse wave velocity, the carotid-femoral pulse wave velocity measures the pulse wave velocity along the aorta-iliac pathway and is a direct measurement of the aortic pulse wave velocity. Several studies measured the carotid-femoral pulse wave velocity. Some of these studies used the flow waves obtained using Doppler ultrasound [5,8,9,100,101]. Some of these studies used the pulse waves obtained using a pulse transducer [4,73,124,135]. It was not clarified if the pulse transducer measured the pressure waves or the flow waves. However, it is likely that the pulse wave measured was related to the pressure wave as the studies also mentioned a diastolic curve as part of the pulse wave [4,124,135]. A study used the pressure wave obtained using a pressure probe [90]. The principle of the pressure probe was not explained nor was the quality of the measured pressure wave displayed. A study used the distension wave obtained by echo-tracking [162]. The study used an echo-tracking device evaluated by Kool et al [88], and it was shown that distension waves with close resemblance of the typical pressure waves can be obtained using this device.

Currently, two commercial devices, SphygmoCor and Complior, are popularly used to obtain the carotid-femoral pulse wave velocity in clinical research. Using the SphygmoCor device, the pressure waveforms at the carotid artery and the femoral arteries are acquired consecutively using applanation tonometry [45,83,111]. The pressure waveforms are synchronized using the electrocardiographic signal as the reference. The pulse transit time is calculated as the foot-to-foot interval between the pressure waveforms. The

distance between the sites is taken as the distance from the sternal notch to the applanation site at the femoral artery as measured on the surface of the skin [83,111], or the distance from the sternal notch to the femoral applanation site less the distance from the sternal notch to the carotid applanation site [45]. Using the Complior device, the pressure waveforms at the carotid artery and femoral arteries are acquired simultaneously using a piezo-electric pressure transducer [6,10,17,104]. The pulse transit time is determined by a correlation algorithm. In short, the correlation between the part of the initial rise to just after the peak of the carotid waveform and that of the time-shifted femoral waveform is found, and the pulse transit time is estimated from the time-shift that gives the maximum correlation [6]. The distance is taken as the distance between the two applanation sites [6,10,104]. In the study by Asmar et al [6], the pressure waveforms obtained using the pressure transducer were shown, and they were not similar to the typical pressure waveforms found in literature. However, clear initial upstrokes of the waveforms can be easily identified.

SphygmoCor and Complior use different algorithms to measure the pulse transit time and the distance traveled. It has been shown that the pulse transit time calculated using these two algorithms are significantly different and the measurement of pulse wave velocity is critically dependent on the algorithm used to measure the pulse transit time [112]. It has also been shown that travel distances measured by these two methods are significantly different [130]. In addition, abdominal obesity and large busts in women can also make distance measurement inaccurate.

Pulse wave velocity can also be measured along the aorta using MRI [58,133,141]. Flow velocity is obtained at different levels along the aorta using velocity-encoded MRI images [58]. The pulse transit time is obtained from the velocity curves. Distances between the levels are measured on the long-axis image of the aorta [58].

Pulse wave velocity can also be measured along the aortic arch using Doppler ultrasound [22, 140]. Flow waveforms are measured at the ascending and descending aorta. The pulse transit time is calculated as the foot-to-foot interval between the measured flow waveforms. The distance is measured on the B-mode image of the aortic arch.

Recently, a new device, the arteriograph, has been developed to measure aortic pulse wave velocity [11,75]. This device makes use of an oscillatory method to measure the brachial artery pressure waveform through an inflated cuff. In short, the change in the pressure in the artery beneath the inflated cuff induces oscillations, and these oscillations are detected and used as an indirect measure of the change in the pressure. To measure the pulse

wave velocity, the cuff is over-inflated to 35 mmHg over the systolic pressure. It is claimed that, because of the over-inflation, the signal of the reflected wave is intensified and can be detected more easily [75]. The time interval between the first wave and the second wave of the measured waveform corresponds to the distance from jugulum to the symphysis, and the pulse wave velocity is thus derived [11]. It has been shown that the pulse wave velocity measured by this device is related to the pulse wave velocities measured by SphygmoCor and Complior [11,75] and also invasively [71]. However, it has also been shown that the relation between the pulse wave velocity measured by arteriograph and the carotid-femoral pulse wave velocity measured by applanation tonometry is low [118]. In addition, the underlying principle of arteriograph is questioned. Through a simulation study, it has been shown that arteriograph can only pick up the wave reflection phenomenon confined to the brachial artery and reflect the stiffness of the brachial artery [159].

1.3.3 Current methods to monitor cardiac output

Pulse contour analysis

Pulse contour analysis is a method for the estimation of the cardiac output using the arterial pressure waveform. The idea was put forward as early as 1904 [62]. The central aorta is considered as a elastic chamber, which distends during systole to accommodate the sudden increase in volume. Therefore, the rise in pressure during systole is related to the ventricular ejection. This relationship is dependent on various factors, such as the size and elasticity of the aorta, and therefore varies among individuals. Calibration is thus required to determine the absolute value of the cardiac output from the arterial pressure. Various equations have been put forward to describe the pressure-flow relationship [2,170].

Wesseling et al. [172] proposed to relate the area under the systolic portion of the pressure waveform to the cardiac output through the characteristic impedance of the aorta. The characteristic impedance is determined during calibration, and is updated during the estimation of the cardiac output according to various factors, such as the changes in the heart rate and the mean arterial pressure. Several studies have shown that this method can estimate cardiac output accurately with thermodilution as the reference method [53,74,132,158]. However, it has also been suggested that this method may become unreliable during hemodynamic instability [132,158]. It should also be noted that, theoretically, aortic pressure waveform should be used as the input of Wesseling's algorithm [74], but in practice the radial

or femoral artery pressure waveform is used as a surrogate.

Currently, three commercial devices, PiCCO, PulseCO and FloTrac, estimate cardiac output using pulse contour analysis.

PiCCO is based on Wesseling's algorithm [53,132]. The more recent version also uses the diastolic portion of the pressure waveform to estimate arterial compliance [48]. It has been shown that the enhanced version of PiCCO can estimate cardiac output with acceptable accuracy during hemodynamic instability [49].

PulseCO is based on a cardiac output-radial artery pressure relationship developed in the frequency domain [97]. To use this relationship to derive the cardiac output, three quantities, including the first harmonic of the aortic input impedance, the first harmonic of the transfer function from the aortic pressure to the radial artery pressure, and the ratio of the cardiac output to the first harmonic of aortic flow, have to be approximated. These three quantities are estimated from the radial artery pressure using equations that are derived from the data of the modelling studies by Karamangoglu et al. [78,79] and the in-vitro study by Langewouters et al. [91]. It has been shown that the limits of agreement between PulseCO and lithium dilution during a 4-hour calibration-free period was about 20% to 30%, which is acceptable [29]. Low bias but wide confidence limits of PulseCO has also been report with thermodilution as the reference method [108]. It has also been shown that PulseCO cannot estimate cardiac output reliably during change of systemic vascular resistance [176].

In contrast to the PiCCO system and the PulseCO system, the FloTrac/Vigileo system does not require external calibration. Instead, cardiac output is estimated from the arterial pressure waveform in conjunction with the demographic data of the patients. The relationship of the cardiac output and the arterial pressure waveform is based on the data from an in-vitro study of the elasticity of human aorta [105]. The validation of the accuracy of this device has been disappointing so far. In an article by Biancofiore et al. [16], the validation studies of this device published from 2006 to 2008 were reviewed. Only two out of 13 published studied achieved an agreement error of less than 30 %. Recently, it is claimed that a software upgrade can improve the performance of this device [106, 146]. However, studies have shown that even with the upgraded software, the agreement error of this device is still larger than 30 % [16,146]. Further investigation is required.

Transcutaneous echocardiography

A commercial device, USCOM, estimates cardiac output using transcutaneous echocardiography [157]. The device consists of a Doppler flow probe. The probe is placed on the chest at either the left parasternal position to measure pulmonary blood flow velocity or the suprasternal position to measure aortic blood flow velocity. Stroke volume is calculated as the velocity-time integral of the measured Doppler spectrum times the cross-sectional area of the valve. The cross-sectional area is calculated from the subject's height. Cardiac output is calculated as the product of the stroke volume and the heart rate. Training is required to use this device, but it has been suggested that the learning curve is short [35,157,164]. It has also been suggested that inter-observer variability may be high [125,157,]. Some studies have shown that the device has clinically acceptable agreement with thermodilution [31,35] while some studies have shown poor agreement [20,30,87]. It has also been shown that the device has poor agreement with conventional echocardiography method [125]. It has also been suggested that more accurate measurement of the cross-sectional area may improve the performance of the device [87].

Other methods

Cardiac output can be estimated using transoesophageal echocardiography. The instrument consists of a standard echocardiographic system attached to a conventional flexible endoscope. The distal end of the endoscope is advanced into the esophagus and the ultrasound transducer is positioned behind the heart. Sedation is usually provided to reduce the subject's anxiety and improve the subject's compliance [50]. The procedure is usually considered as semi-invasive.

Cardiac output can be estimated non-invasively using the partial carbon dioxide rebreathing method based on the Fick's principle. In the direct Fick method, the mix venous oxygen or carbon dioxide content is measured from the blood sample taken at the pulmonary artery. In the rebreathing method, the subject breathes into a bag of gas mixture for a couple of times. The mixed venous carbon dioxide oxygen is then estimated from carbon dioxide concentration of the bag. The detailed description of the procedure is given by Franciosa [51]. This method is only accurate during precisely controlled mechanical ventilation and showed poor agreement with thermodilution during spontaneous breathing [156].

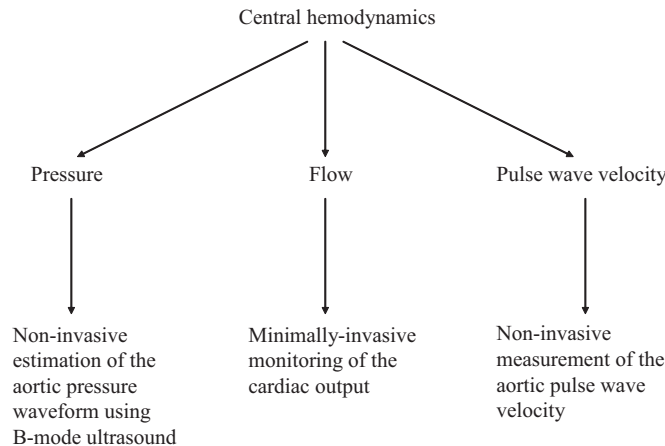


Figure 1.1: The overall objectives

1.4 Thesis objectives

The overall objective of this thesis is to develop and evaluate non-invasive and minimally-invasive methods for measuring and monitoring three aspects of central hemodynamics, including pressure, flow and the propagation velocity of pressure and flow pulses, which is equivalent to PWV (Figure 1.1).

In this thesis, novel methods are developed to

- measure the arterial stiffness using non-invasive data.
- monitor the cardiac output using minimally-invasive data.
- measure the aortic pressure waveform non-invasively.

From a modelling perspective, the underlying algorithms of these methods are interrelated. The arterial system is modeled as a single uniform lossless transmission line terminated by a complex load. Each measuring or monitoring task is a problem of identification, simulation or data acquisition. The specific objectives of this thesis are as follows:

1. Formulating the arterial stiffness estimation problem as an identification problem.
 - (a) Modelling the arterial system as a single lossless uniform transmission line.

- (b) Identifying the model using the carotid artery pressure and the aortic flow as the input and output to the model.
 - (c) Estimating the arterial stiffness using the identified model parameters.
- 2. Formulating the cardiac output monitoring problem as a problem of identification and simulation.
 - (a) Modelling the pulse transmission path from the ascending aorta to the radial artery as a single lossless uniform transmission line.
 - (b) Identifying the model using the aortic flow and the radial artery pressure as the input and output to the model.
 - (c) Deriving a transfer function from the radial artery pressure to the aortic flow using the identified model parameters.
 - (d) Simulating the aortic flow using the derived transfer function and the radial artery pressure.
- 3. Measuring the aortic pressure waveform using the aortic distension waveform obtained using B-mode imaging.
 - (a) Developing a semi-automatic algorithm for the measurement of the aortic distension waveform from a series of B-mode images of the aortic arch.
 - (b) Applying a calibration scheme to estimate the aortic pressure waveform from the aortic distension waveform.

The following contributions were made:

- 1. As presented in Chapter 2, during the development of the arterial stiffness estimation method:
 - (a) A white-box identification algorithm was developed for the transmission line model implemented using a finite-element method.
 - (b) The white-box identification algorithm was applied to the non-invasive data obtained from a group of healthy children and a group of children with Marfan syndrome. Aortic pulse wave velocity and the ratio of the large artery compliance to the small artery compliance were obtained from the identified model parameters. These two indices could differentiate the group of healthy children from the group of children with Marfan syndrome.

2. As presented in Chapter 3, during the development of the cardiac output monitoring method:
 - (a) A state-space representation of the transmission line model based on the finite element method was developed.
 - (b) A grey-box identification algorithm was developed for the proposed state-space representation of the transmission line model.
 - (c) The model identifiability of the proposed state-space representation, and the bias and variances of the proposed grey-box identification algorithm were investigated.
 - (d) A cardiac output monitoring technique was developed using the proposed grey-box identification. The cardiac output monitoring technique was applied to a group of post-operative infants. The technique achieved clinically acceptable accuracy without re-calibration for the first five hours.
3. As presented in Chapter 4, during the development of the method for aortic pressure waveform measurement:
 - (a) A semi-automatic algorithm for the measurement of the aortic distension waveform based on block-matching, edge detection using the gradient of the intensity, and smoothness constraint on the continuity of the wall motion was developed.
 - (b) The algorithm was applied to the B-mode images obtained from a group of healthy children. The aortic pressure waveform was estimated from the aortic distension waveform through linear and exponential calibration schemes, and compared to the carotid artery pressure waveform obtained using applanation tonometry. The morphologies of the waveforms, and the derived central pulse pressure and total arterial compliance were in good agreement.

Chapter 2

Model-based Aortic Pulse Wave Velocity^{1,2,3}

Aortic pulse wave velocity (PWV) is an independent predictor of all-cause and cardiovascular mortality in hypertensive patients [92], cardiovascular mortality in subjects over 70 years of age [109], and cardiovascular events in different populations [19,93,154].

Aortic PWV is often estimated as the carotid-femoral pulse wave velocity, which is measured as the pulse transit time (PTT) from the carotid site to the femoral site divided by the distance between the two sites [112,130]. This method is very sensitive to PTT. Different methods to measure PTT can result in significantly different PWV [112]. In addition, the distance between the sites is measured on the surface of the skin, and may be inaccurate in subjects with large busts or abdominal obesity.

Aortic PWV is also popularly measured using echocardiography [22,140]. PTT is determined from the Doppler flow pulses measured at the ascending and descending aorta, and the distance is measured on the image of the aortic arch. However, in some subjects, a clear image of the aortic arch may be difficult to obtain.

To avoid the difficulties caused by PTT and distance measurements, a model-based method for estimating PWV without PTT and distance measurements is developed in this chapter.

¹ A version of this chapter has been submitted.

² M. Leung, G. A. Dumont, G. G. S. Sandor and J. E. Potts, "Estimating arterial stiffness using transmission line model," 28th IEEE Engineering in Medicine and Biology Conference, New York, 2006

³ M. Leung, G. A. Dumont, J. E. Potts, M. T. Potts and G. G. S. Sandor, "A model-based method to estimate pulse wave velocity," 11th World Congress of Medical Physics and Biomedical Engineering, Munich, Germany, 2009

2.1 Introduction

Arterial stiffness affects the change in the lumen area of the arteries given a change in pressure. It has been suggested that increase in arterial stiffness causes increase in central systolic and pulse pressures, which is a risk factor of cardiovascular events [1,137]. A number of physiological parameters have been proposed as indices of arterial stiffness, e.g. PWV, arterial distensibility and total arterial compliance. Of all these parameters, PWV is probably the most accepted index of arterial stiffness [123]. According to the Moens–Korteweg equation, PWV is related to the Young’s modulus (E) of a thin-walled elastic tube by: $PWV = \sqrt{E \times h / 2r\rho}$, where ρ is the fluid density, h is the wall thickness and r is the tube radius. [119,123]. It is generally accepted that PWV increases as arterial stiffness increases.

By definition, PWV is the distance travelled by a (pressure or flow) pulse divided by the time of travel. Previous researchers have devised several methods to measure PWV by measuring PTT and travel distance. In this thesis, these previous methods are referred to as the direct methods as compared to the model-based method developed in this chapter.

The direct methods use echocardiography [22,140], magnetic resonance imaging (MRI) [58,141] or applanation tonometry [112,130]. Using echocardiography, PTT is measured as the delay between the flow pulses at the ascending and descending aorta while distance is measured on the long-axis image of the aortic arch. Using MRI, PTT is measured as the delay between the flow pulses at different locations along the entire aorta while distance is measured on the long-axis image of the aorta. Using applanation tonometry, PTT is measured as the delay between the pressure pulses at the carotid and femoral arteries while distance is measured on the surface of the skin.

In the measurement of the carotid-femoral PWV using applanation tonometry, PTT is in the range of 30 to 100 ms while the distance is in the range of 40 to 100 cm [112,130]. In these ranges, a difference of 10 ms in PTT can result in a difference of 100 cm/s in PWV. Therefore the precision requirement for PTT is rather high.

A model-based method to measure PWV without PTT and distance measurements is developed in this chapter. A single uniform transmission line terminated by a complex load is used to model the arterial system (Figure 2.1). The applicability of this model has been described elsewhere [14,15]. The analogy between this model and the arterial system is explained in Appendix A. The line is assumed to be lossless since the resistance along the pulse transmission path is very small [15,25]. For a lossless transmission line, the phase velocity can be calculated from the line capacitance and the

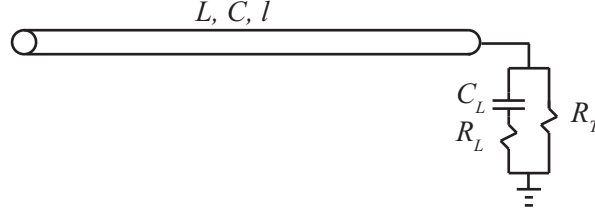


Figure 2.1: A transmission line terminated by a complex load: L is the line inductance; C is the line capacitance; l is the line length; C_L is the load capacitance; R_L is the load resistance; R_T is the terminating resistance.

line inductance. The phase velocity of the line corresponds to the PWV of the arterial system.

To identify the model parameters, ascending aortic pressure (AAP) and ascending aortic flow (AAF) are used as the input and output to the model respectively. PWV is then calculated from the identified line capacitance and line inductance. The carotid artery pressure waveform is acquired non-invasively using applanation tonometry and used as a surrogate to the AAP waveform [81]. The AAF waveform is acquired using echocardiography.

The purpose of this model-based method is to provide a tool to differentiate subjects with abnormal arterial stiffness from the healthy subjects. If this method can indicate abnormal arterial stiffness, it will be useful in predicting cardiovascular events and quantifying cardiovascular risks.

In this thesis, a clinical study was performed to investigate the usefulness of this new method. In this study, the model-based method was applied to 8 healthy children and 8 children with Marfan syndrome (MFS). MFS is a connective tissue disorder. It is generally agreed that MFS causes abnormal elastic fiber content in the arterial wall, especially at the ascending aorta. Its primary cardiovascular manifestation is progressive dilatation of the aortic root eventually leading to aortic dissection or rupture [38]. It has been found in several studies that aortic pulse wave velocity is higher in subjects with MFS [22,58,59,140].

MFS is chosen in this study since its major manifestation is abnormal arterial stiffness. The objective was to investigate if the model-based method can differentiate subjects with MFS from healthy subjects. The model-based method was also compared to the direct method using echocardiography and the correlation between these two methods were found.

2.2 Methods

2.2.1 Outline of the model parameter identification algorithm

The model has six parameters: line inductance (L), line capacitance (C), load capacitance (C_L), load resistance (R_L), terminating resistance (R_T) and line length (l). R_L is dependent on L , C and R_T , therefore there are only five free parameters. L and R_T are estimated using some known relations. The remaining three free parameters, C , C_L and l are found by minimizing a performance index (J).

The carotid artery pressure waveform is used as the input to the model while the AAF waveform is the output. J consists of the difference between the model-predicted and the experimentally-measured AAF waveforms. An iterative optimization algorithm is used to minimize J . The transmission line model is numerically implemented using the finite element method as described in Appendix B. Since J may not be convex, a set of initial values for C , C_L and l are chosen based on some physiological information of the subject. It is assumed that this set of initial values would lead to a local minimum that corresponds to the true values of C , C_L and l .

A version of the Newton conjugate-gradient method is used to minimize J [120]. It is a line search method, in which a direction is chosen from the current iterate and along this direction the next iterate is searched for such that J has a lower value. In this method, the direction is either the pure Newton direction or an approximation to it, found using the conjugate gradient method. Obtaining the Newton direction is a non-trivial task, and it can only be used as a search direction if the Hessian of J is positive definite. In the conjugate gradient method, the Newton direction is solved for iteratively. If the Hessian is found to be non-positive definite during the computation of the next iterate, the current iterate is chosen as an approximation to the Newton direction instead. The conjugate gradient method is very fast and therefore is chosen to compute the search direction. The simplest line search method is the steepest descent method, in which the search direction is the negative gradient of J at the current iterate. Although it is conceptually simple and easy to implement, the steepest descent method is often excruciatingly slow. In contrast, the Newton method typically has superlinear rate of convergence and is therefore chosen as the optimization algorithm in this study.

2.2.2 Estimations of the line inductance and the terminating resistance

The transmission line equations are analogous to the one dimensional Navier-Stokes equations for incompressible, pulsatile flow in an elastic tube. The two set of equations are presented and the analogy is explained in Appendix A.

The line inductance corresponds to the density of the fluid divided by the cross-sectional area of the tube. Accordingly, L is estimated as:

$$L = \frac{\rho_b}{A_{ao}} \quad (2.1)$$

where ρ_b is the blood density and A_{ao} is the lumen area of the ascending aorta as measured by echocardiography. The standard value of blood density, 1.056 g/cm^3 (or $0.00079 \text{ mmHg s}^2/\text{cm}^2$), is used.

The terminating resistance corresponds to the peripheral resistance. Accordingly, R_T is estimated as mean (time-averaged) pressure (\bar{P}) divided by mean (time-averaged) flow (\bar{Q}):

$$R_T = \frac{\bar{P}}{\bar{Q}} \quad (2.2)$$

2.2.3 Initial values of the line capacitance, the load capacitance and the line length

The line length corresponds to the distance from the root of the ascending aorta to the effective reflection site [27], which is also referred to as the effective arterial length. It has been suggested that the effective arterial length is dependent on age [114,119] and the relative distribution of the compliance in the arterial system [114]. Therefore, it is expected that l varies among different age groups and groups with different pathological conditions. l should also be dependent on body size since as height increases, the distances to each actual reflection sites also increase. In a previous invasive study [116], it was shown that the average effective arterial length was 48 cm for a group of normal men with the average body surface area (BSA) of 1.98 m^2 . In this method, a crude initial value is obtained by assuming that l varies linearly with BSA:

$$l_{\text{initial}} = \frac{\text{BSA}}{1.98} \times 48 \quad (2.3)$$

It should be noted that this equation was conceived to provide an initial value of l . In fact, l is dependent on a lot of factors and may not have a linear relationship with BSA.

In the transmission line model, the total capacitance (C_T) is

$$C_T = C \times l + C_L \quad (2.4)$$

In this method, C_T is initially estimated by the total arterial compliance (TAC) calculated using the area method [98], which is given by

$$\text{TAC} = \frac{A_{12}}{R_T(P_1 - P_2)} \quad (2.5)$$

where P_1 is the pressure at the very beginning of the diastolic decay, P_2 is the end-diastolic pressure and A_{12} is the area under the pressure curve between P_1 and P_2 (Figure 2.2). In a previous modelling study using data collected from open-chest dogs [28], it was found that the total line capacitance (line capacitance times line length) was 40-50% of the total capacitance. Accordingly, the initial values of C and C_L are calculated as follows:

$$C_{\text{initial}} = \frac{\text{TAC}}{2l_{\text{initial}}} \quad (2.6)$$

$$C_{L,\text{initial}} = \frac{\text{TAC}}{2} \quad (2.7)$$

2.2.4 Estimation of the load resistance

At high frequencies, as viewed from the ventricles, the arterial system appears to be minimally reflective [160]. It can be assumed that the terminating impedance matches the characteristic impedance of the line at high frequencies [28]. For a lossless line, the characteristic impedance is $\sqrt{L/C}$ and therefore R_L is estimated as:

$$R_L = \frac{1}{\sqrt{\frac{C}{L}} - \frac{1}{R_T}} \quad (2.8)$$

2.2.5 Performance index

The performance index J is defined as follow:

$$J = \frac{\sum_i^n (Q_{ao,m}(i) - Q_{ao,e}(i))^2}{n} + \mu\Lambda \quad (2.9)$$

with

$$\Lambda = (\max(F - mn, 0))^2 \quad (2.10)$$

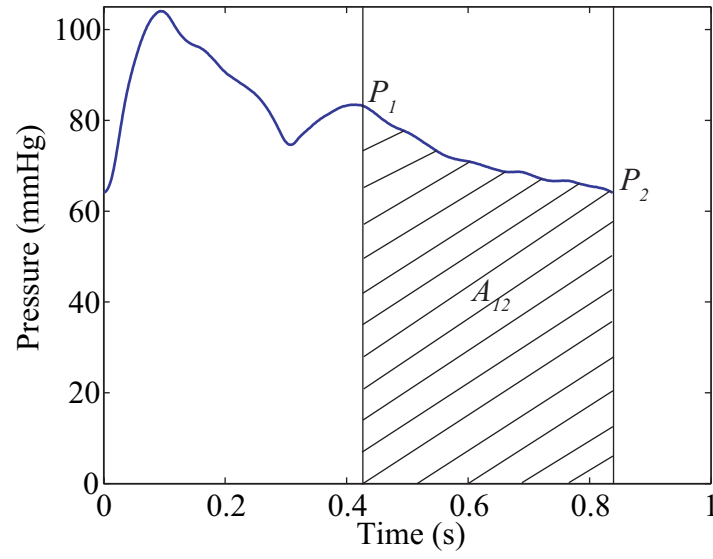


Figure 2.2: The calculation of the total arterial compliance: P_1 is the pressure at the beginning of the diastolic decay; P_2 is the end-diastolic pressure; A_{12} is the area under the pressure curve between P_1 and P_2 .

$$mn = 10 \quad (2.11)$$

where $Q_{ao,m}$ is the model-predicted ascending aortic positive flow, $Q_{ao,e}$ is the experimentally-measured ascending aortic positive flow, n is the number of data points, F is the magnitude of the model-predicted negative flow, mn is the allowed magnitude of the negative flow, and μ is the penalty coefficient. In this study, the sampling rate for the pressure and flow waveforms was 12.0 kHz and n was about 10^4 . The meanings of $Q_{ao,m}$ and F are also displayed in Figure 2.3.

In this method, when obtaining the experimentally-measured AAF from the Doppler spectrum, only the positive flow during the ventricular ejection is considered. The first term of J corresponds to mean-squared error between the experimentally-measured and the model-predicted ascending aortic positive flow (Figure 2.3). A small amount of negative flow often occurs after the ventricular ejection. Therefore, J is defined to allow only a small amount of negative flow. The second term of J penalizes large magnitude of negative flow.

The mean-squared error between the experimentally-measured and the model-predicted ascending aortic positive flows is expected to range from 10^2 to 100^2 cm⁶/s. Accordingly, μ is chosen to be 1. If the magnitude of the negative flow is larger than 20, the penalty term would be of the same order of magnitude as the mean-squared error. Setting μ at 1 effectively restricts the search of the solution in a neighborhood with F smaller than 20 cm³/s.

2.2.6 Calculation of the model-based pulse wave velocity

For a lossless transmission line, PWV is given by

$$\text{PWV}_{\text{model}} = \frac{1}{\sqrt{LC}} \quad (2.12)$$

2.3 Experiments

2.3.1 Data acquisition and processing

This study was approved by the University of British Columbia Children's and Women's Research Ethics Board. 8 healthy children and 8 children with MFS participated in this study.

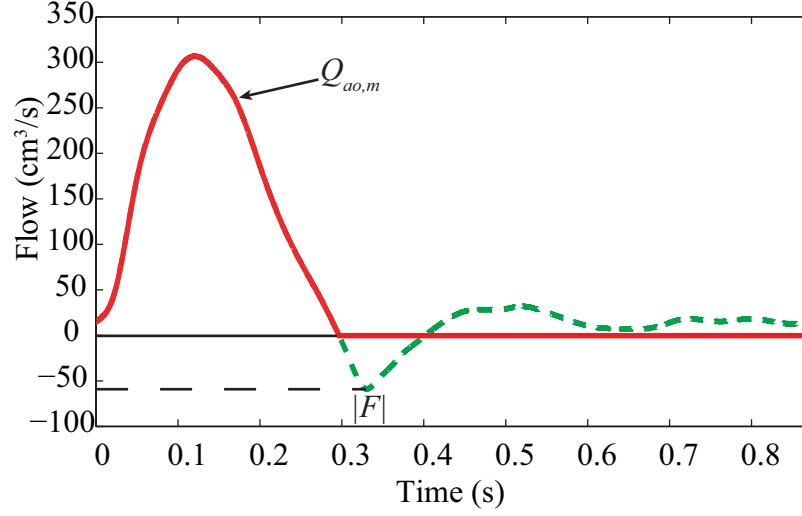


Figure 2.3: The model-predicted ascending aortic flow and its components: $Q_{ao,m}$ is the positive ascending aortic flow; F is magnitude of the negative flow immediately after the ventricular ejection.

Model-based pulse wave velocity

Ascending aortic blood velocity was obtained using Doppler ultrasound with the transducer positioned at the suprasternal notch. The carotid artery pressure waveform was obtained simultaneously using applanation tonometry. Brachial artery systolic and diastolic blood pressures were measured using a cuff sphygmomanometer. The aortic annulus was measured using two-dimensional echocardiography. All the applanation-tonometric and echocardiographic data were acquired using a GE Vivid 7 Pro ultrasound machine (GE Vingmed, Horten, Norway) equipped with an applanation tonometer.

The AAF waveform was obtained by tracing the envelope of the Doppler spectrum of the ascending aortic blood velocity and multiplying it by the lumen area (Figure 2.4, upper left panel). The lumen area was assumed to be circular and was calculated from the aortic annulus. Only the positive flow during the ventricular ejection was considered, and zero flow was assumed after the ventricular ejection (Figure 2.4, upper right panel). The carotid artery pressure waveform was used as a surrogate to the AAP waveform (Figure 2.4, lower left panel). It has been previously shown that aortic pressure waveform measured invasively and carotid artery pressure waveform mea-

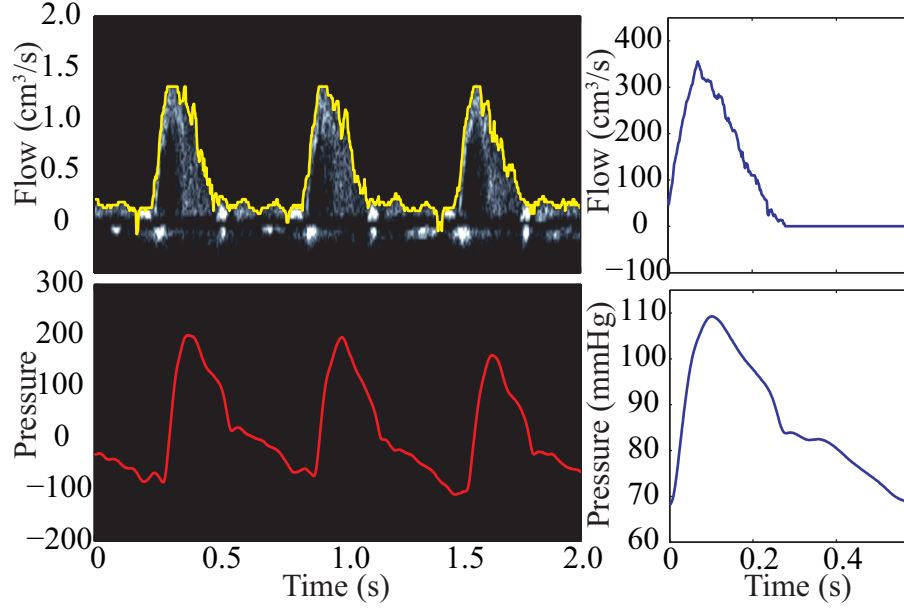


Figure 2.4: Upper left panel: the Doppler spectrum and its envelope. Upper right panel: the averaged flow waveform; zero flow was assumed after the ventricular ejection. Lower left panel: the uncalibrated pressure waveform obtained using applanation tonometry. Lower right panel: the averaged pressure waveform.

sured by applanation tonometry simultaneously have similar morphology [81]. The carotid artery pressure waveform was then calibrated by assuming that mean and diastolic pressures were constant throughout the arterial tree [82]. Mean pressure (MP) was calculated from the brachial artery systolic (SP) and diastolic pressures (DP) using the traditional formula [21]: $MP = (SP + 2DP)/3$. Mean pressure was assigned to the area integral over the duration of the carotid artery pressure waveform, and diastolic pressure was assigned to the minimum of the carotid artery pressure waveform (Figure 2.4, lower right panel).

Two sets of 4 to 6 beats were selected based on quality from each subject and averaged. The first set was used for parameter identification and the second set for model validation.

Direct pulse wave velocity using echocardiography

The data acquisition procedure for the direct measurement of the aortic PWV using echocardiography has been described in details by Sandor et al. [140]. The Doppler spectrum of the ascending aortic blood velocity was acquired with the sample volume placed at the valve leaflets. Then, the Doppler spectrum of the descending aortic blood velocity was acquired with the sample volume placed as distally as possible. PTT was calculated as the time from the QRS to the onset of the descending aortic flow minus the time from the QRS to the onset of the AAF. The distance between the two recording sites was measured on the B-mode image of the aortic arch.

2.4 Results

Data are expressed as mean \pm SD. All the clinical characteristics and the resulting estimates of the two groups were compared by means of an unpaired Student's t -test. A value of $p < 0.01$ was considered statistically significant. The clinical characteristics of the subjects are listed in Table 2.1.

TAC, the fixed model parameters including L and R_T , and the initial model parameters including C_{initial} , $C_{L,\text{initial}}$ and l_{initial} , are listed in Table 2.2. C_{initial} , $C_{L,\text{initial}}$ and l_{initial} were calculated from TAC and BSA as describe in the previous section.

The final model parameters, including C , C_L and l are listed in Table 2.3. C , C_L and l were obtained through the minimization of J . The ratio of C to C_L is also listed in Table 2.3.

The penalty coefficient (μ) is chosen to be 1 as described in the previous section. However, to investigate the effect of μ , the optimization of J was also performed with μ set at 0.1, 10 and 100. The resulting $\text{PWV}_{\mu=0.1}$, $\text{PWV}_{\mu=1}$, $\text{PWV}_{\mu=10}$, $\text{PWV}_{\mu=100}$ are listed in Table 2.4. PWV_{echo} , which is the direct PWV using echocardiography, and $\text{PWV}_{\text{initial}}$, which is calculated using C_{initial} and L are also listed in Table 2.4.

Model validation are evaluated by the root-mean-squared error (RMSE) between the model-predicted and experimentally-measured ascending aortic positive flow waveforms. Two RMSE values were calculated with one using C_{initial} , $C_{L,\text{initial}}$ and l_{initial} , and one using C , C_L and l . The final estimates were found by setting μ at 1. These values are listed in Table 2.6. A sample of the model-predicted AAF waveform and the corresponding experimentally-measured AAF waveform is shown in Figure 2.8.

The box and whisker plots of $\text{PWV}_{\mu=1}$ and PWV_{echo} are shown in Figure 2.5. The correlation between $\text{PWV}_{\mu=1}$ and PWV_{echo} is shown in

	Control (8)	MFS (8)	<i>p</i> -value
Age (yrs)	11 ± 2	15 ± 3	NS
BSA (m ²)	1.1 ± 0.2	1.7 ± 0.2	<i>p</i> < 0.0006
SP _{BA} (mmHg)	107 ± 8	111 ± 7	NS
DP _{BA} (mmHg)	63 ± 5	70 ± 7	NS
AO (cm)	1.62 ± 0.21	2.16 ± 0.25	<i>p</i> < 0.0003
Peak AAF (cm ³ /s)	265 ± 74	328 ± 117	NS

Table 2.1: Clinical characteristics of the subjects: BSA is the body surface area; SP_{BA} is the systolic pressure at the brachial artery; DP_{BA} is the diastolic pressure at the brachial artery; AO is the aortic annulus; Peak AAF is the peak ascending aortic flow.

	Control (8)	MFS (8)	<i>p</i> -value
TAC (cm ³ /mmHg)	1.2 ± 0.4	2.3 ± 1.0	NS
<i>L</i> (mmHg s ² /cm ³ /cm)	0.00041 ± 0.00012	0.00022 ± 0.00007	<i>p</i> < 0.003
<i>R_T</i> (mmHg s/cm ³)	1.3 ± 0.3	1.3 ± 0.6	NS
<i>C</i> _{initial} (cm ³ /mmHg/cm)	0.022 ± 0.007	0.028 ± 0.009	NS
<i>C_L</i> _{initial} (cm ³ /mmHg)	0.61 ± 0.19	1.14 ± 0.50	NS
<i>l</i> _{initial} (cm)	28 ± 6	40 ± 5	<i>p</i> < 0.0006

Table 2.2: Fixed model parameters and initial model parameters: TAC is the total arterial compliance; *L* is the line inductance; *R_T* is the terminating resistance; *C*_{initial} is the initial value of the line capacitance; *C_L*_{initial} is the initial value of the load capacitance; *l*_{initial} is the initial value of the line length.

Figure 2.6. The Bland-Altman plot of PWV_{μ=1} and PWV_{echo} is shown in Figure 2.7.

The model-based PWV with different μ were found to be significantly higher in the MFS group. Both PWV_{initial} and PWV_{echo} are not significantly different between the MFS and the control groups. The correlations between PWV_{echo} and different model-based PWV are shown in Table 2.5

	Control (8)	MFS (8)	p -value
C (cm ³ /mmHg/cm)	0.015 ± 0.007	0.013 ± 0.006	NS
C_L (cm ³ /mmHg)	0.63 ± 0.19	1.35 ± 0.69	NS
l (cm)	25 ± 7	34 ± 5	NS
C/C_L	0.025 ± 0.009	0.011 ± 0.003	$p < 0.003$

Table 2.3: Final model parameters: C is the final estimate of the line capacitance; C_L is the final estimate of the load capacitance; l is the final estimate of the line length.

	Control (8)	MFS (8)	p -value
PWV _{$\mu=1$} (cm/s)	438 ± 97	626 ± 115	$p < 0.004$
PWV _{$\mu=0.1$} (cm/s)	383 ± 112	578 ± 143	$p < 0.01$
PWV _{$\mu=10$} (cm/s)	410 ± 92	600 ± 119	$p < 0.004$
PWV _{$\mu=100$} (cm/s)	398 ± 107	605 ± 132	$p < 0.005$
PWV _{echo} (cm/s)	362 ± 133	444 ± 115	NS
PWV _{initial} (cm/s)	349 ± 69	422 ± 55	NS

Table 2.4: Pulse wave velocity: PWV _{$\mu=1$} is the model-based pulse wave velocity with the penalty coefficient set at 1; PWV _{$\mu=0.1$} is the model-based pulse wave velocity with the penalty coefficient set at 0.1; PWV _{$\mu=10$} is the model-based pulse wave velocity with the penalty coefficient set at 10; PWV _{$\mu=100$} is the model-based pulse wave velocity with the penalty coefficient set at 100; PWV_{echo} is the direct measurement of pulse wave velocity using echocardiography; PWV_{initial} is the pulse wave velocity estimated using the initial value of the line capacitance.

	Correlation
PWV _{echo} vs PWV _{$\mu=1$}	0.51
PWV _{echo} vs PWV _{$\mu=0.1$}	0.26
PWV _{echo} vs PWV _{$\mu=10$}	0.60
PWV _{echo} vs PWV _{$\mu=100$}	0.52
PWV _{echo} vs PWV _{initial}	0.50

Table 2.5: Correlations between the echocardiographic pulse wave velocity and different model-based pulse wave velocities: PWV _{$\mu=1$} is the model-based pulse wave velocity with the penalty coefficient set at 1; PWV _{$\mu=0.1$} is the model-based pulse wave velocity with the penalty coefficient set at 0.1; PWV _{$\mu=10$} is the model-based pulse wave velocity with the penalty coefficient set at 10; PWV _{$\mu=100$} is the model-based pulse wave velocity with the penalty coefficient set at 100; PWV_{echo} is the direct measurement of pulse wave velocity using echocardiography; PWV_{initial} is the pulse wave velocity estimated using the initial value of the line capacitance.

	Control (8)	MFS (8)
RMSE _{initial} (cm ³ /s)	45.2 \pm 18.4	92.4 \pm 40.7
RMSE (cm ³ /s)	27.4 \pm 6.2	31.0 \pm 17.30

Table 2.6: Performance of the model: RMSE is the root-mean-squared error between the model-predicted and experimentally-measured ascending aortic positive flow waveforms; RMSE_{initial} was calculated using the initial values of the line capacitance, load capacitance and line length; RMSE was calculated using the final estimates of the line capacitance, load capacitance and line length. The final estimates were found using optimization with the penalty coefficient set at 1.

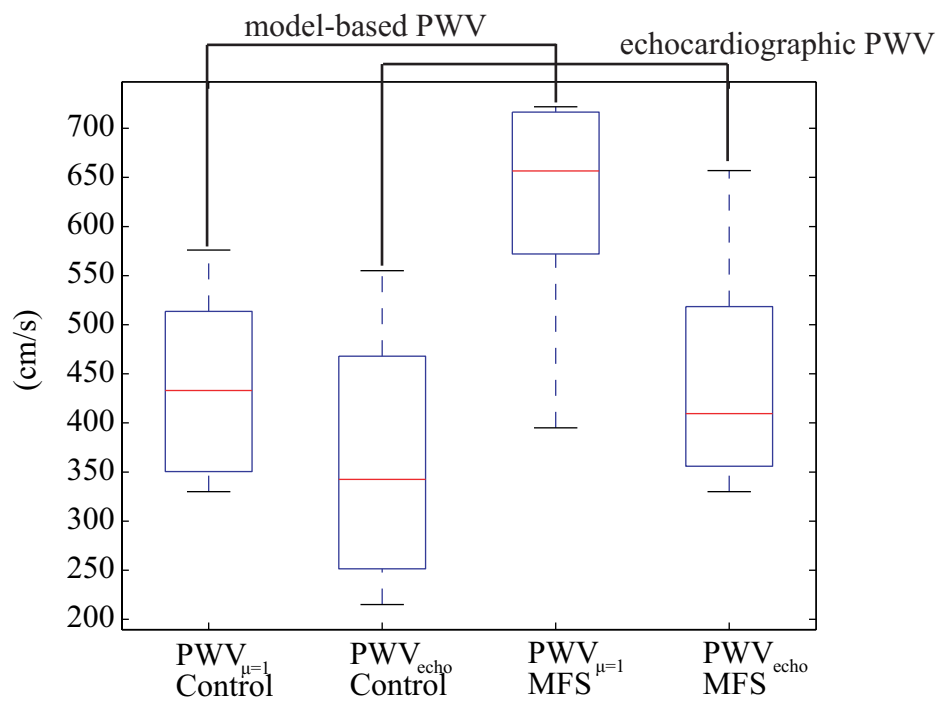


Figure 2.5: Box and whisker plots: medians, upper and lower quantiles and ranges are displayed; $PWV_{\mu=1}$ is the model-based pulse wave velocity; PWV_{echo} is the direct pulse wave velocity obtained using echocardiography.

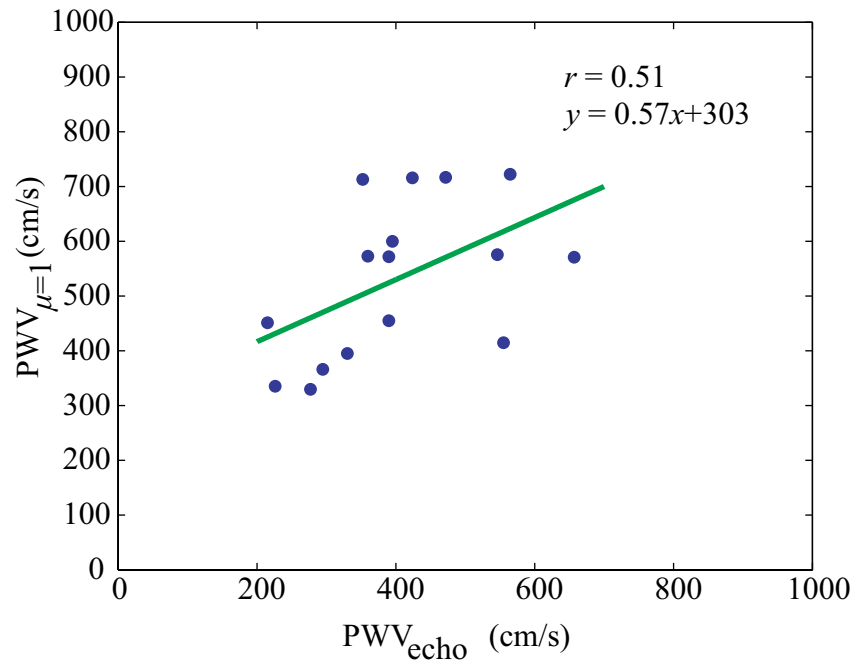


Figure 2.6: Correlation between the model-based pulse wave velocity and the direct pulse wave velocity: $PWV_{\mu=1}$ is the model-based pulse wave velocity; PWV_{echo} is the direct pulse wave velocity obtained using echocardiography.

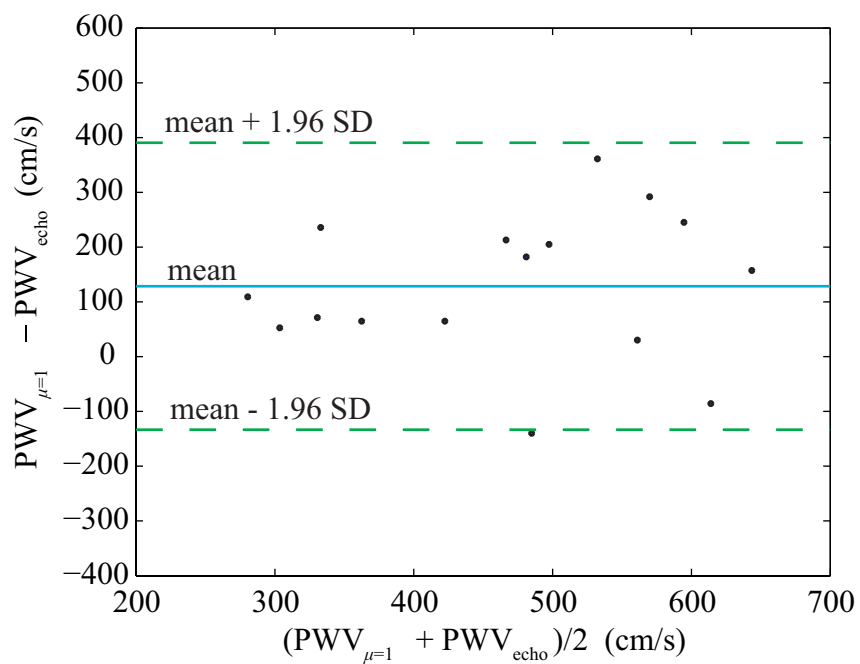


Figure 2.7: Bland-Altman plot of the model-based pulse wave velocity and the direct pulse wave velocity: $PWV_{\mu=1}$ is the model-based pulse wave velocity; PWV_{echo} is the direct pulse wave velocity obtained using echocardiography.

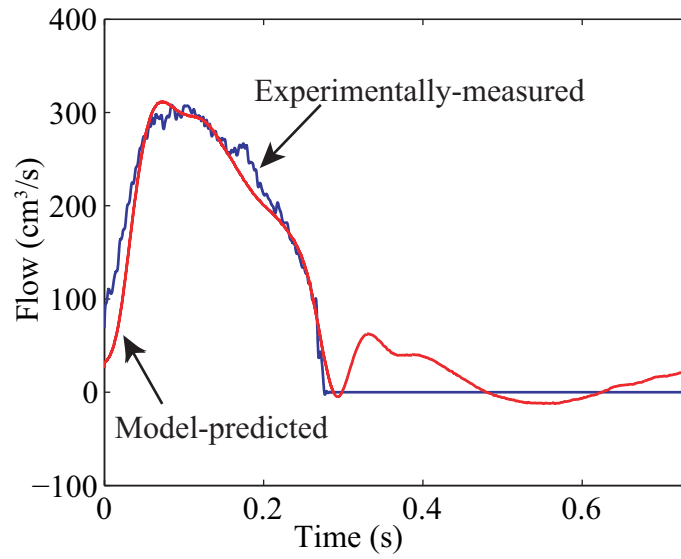


Figure 2.8: A sample of the model-predicted ascending aortic flow waveform and the corresponding experimentally-measured ascending aortic flow waveform: the root-mean-squared error between the model-predicted and experimentally-measured ascending positive flow waveforms is $16.6 \text{ cm}^3/\text{s}$.

2.5 Discussion

2.5.1 Ability to differentiate the subjects with Marfan syndrome from the healthy subjects

$PWV_{\mu=1}$, $PWV_{\mu=0.1}$, $PWV_{\mu=10}$ and $PWV_{\mu=100}$ were higher in the MFS group. It suggests that the proposed model-based pulse wave velocity is able to differentiate the children with MFS from the normal children regardless of the value of the penalty coefficient.

PWV_{initial} was not significantly different between the two groups. It suggests that the optimization step is necessary to obtain a PWV estimate that can differentiate the children with MFS from the normal children.

PWV_{echo} was also not significantly different between the two groups. This is unexpected since pulse wave velocity obtained using echocardiography was found to be higher in subjects with MFS in two other studies [22,140]. A possible reason for this is the small sample size, and therefore the power of the test was small.

In the box and whisker plots (Figure 2.5), it is clear that $PWV_{\mu=1}$ of the control group and $PWV_{\mu=1}$ of the MFS group occupied different ranges. On the other hand, for PWV_{echo} , the range for the control group and the range for the MFS group largely overlapped. It is also clear that, for the MFS group, $PWV_{\mu=1}$ is higher than PWV_{echo} . A possible reason for this is the larger aortic diameter in the MFS group (Table 2.1). By equation (2.1), larger aortic diameter gives smaller L . And by equation (2.12), smaller L gives larger PWV . However, it should not be concluded that the ability of $PWV_{\mu=1}$ to differentiate the two groups was solely due to L . It should be noted that PWV_{initial} has the same dependency on the aortic diameter but it lacks the ability to differentiate the two groups.

To determine if $PWV_{\mu=1}$ can detect abnormal arterial stiffness independent of the size of aorta, a study on two groups with the aortic diameter matched is necessary.

2.5.2 Correlations between the pulse wave velocities obtained by different methods

The correlation coefficient between $PWV_{\mu=1}$ and PWV_{echo} was 0.51 (Figure 2.6). To put this into perspective, a previous study that compared PWV obtained by three devices: Complior, SphygmoCor, and Arteriograph is considered [130]. Both Complior and SphygmoCor measure carotid-femoral PWV , but the algorithms to determine PTT and distance are different. The

main principle behind Arteriograph is to occlude the brachial artery by applying a cuff pressure exceeding systolic pressure by 35–40 mmHg. PTT is then measured as the time interval between the incident and reflected systolic wave. The correlation coefficients between Complior and SphygmoCor, Complior and Arteriograph, SphygmoCor and Arteriograph were 0.57, 0.36, 0.29 respectively. The correlation between the proposed model-based PWV and the echocardiographic PWV is similar to that between Complior and SphygmoCor.

2.5.3 Interchangeability between the pulse wave velocities obtained by different methods

The limits of agreement between $PWV_{\mu=1}$ and PWV_{echo} were -133 cm/s and 391 cm/s. Therefore, $PWV_{\mu=1}$ and PWV_{echo} are not interchangeable. Similar conclusion for Complior and SphygmoCor was found by Millasseau et al. [112]. Both Complior and SphygmoCor are validated techniques to estimate carotid-femoral PWV, and yet they are not interchangeable. It suggests that lack of interchangeability does not affect the validity of either technique. In fact, the PWV estimates are strongly dependent on the underlying algorithms [112,130]. It is recommended that the same PWV estimation method is used when differentiating two different populations.

2.5.4 Performance of the model in predicting ascending aortic flow

The experimentally-measured peak AAF was around 300 cm³/s (Table 2.1). Relative to the peak AAF, the RMSE was reasonable (Table 2.6). As shown in Figure 2.8, the model-predicted AAF waveform is reasonably close to the experimentally-measured AAF waveform.

In addition, using the initial values, the model-predicted ascending aortic positive flow waveform had poor agreement with the experimentally-measured ascending aortic positive flow waveform (Table 2.6). It suggests that the optimization step is necessary.

2.5.5 Large artery compliance to small artery compliance ratio

It is interesting to note that the ratio of C to C_L was lower in the MFS group. In the transmission line model, the line can be considered as representing the aorta and the elastic arteries with the load representing the muscular

arteries and the arterioles. It has been previously shown that increase in arterial stiffness is largely confined to the aorta in the MFS patients [76]. Therefore, it seems reasonable to expect that the ratio of C to C_L would be lower with the MFS patients. Indeed, the ratio of C to C_L found in this study matched this expectation. It suggests that this model and the corresponding identification method can also model the difference in the distribution of compliance.

2.6 Conclusions

In this chapter, a model-based method to estimate PWV is presented. This method was compared to the direct measurement of PWV using echocardiography. A few conclusions were made. First, the model-based PWV had stronger ability than the direct PWV obtained using echocardiography in differentiating the children with MFS from the normal children. Second, the model-based PWV and the direct PWV obtained using echocardiography showed a moderate correlation. Third, the model-based PWV and the direct PWV obtained using echocardiography are not interchangeable.

The number of subjects in this study was small. A follow-up study including a larger number of subjects is necessary to confirm the clinical usefulness of this model-based method.

Chapter 3

Monitoring Cardiac Output using Grey-Box Identification on a State-Space Representation of the Transmission Line Model¹

Cardiac output (CO) is a strong indicator of the adequacy of the cardiovascular circulation. CO normalized to the body surface area is associated with the survival rate of postoperative patients [18,40].

A minimally-invasive technique that allows continuous monitoring of CO is valuable. It has been suggested that CO can be estimated from the peripheral pressure waveform using the pulse contour analysis. In the traditional pulse contour techniques, CO is related to the area of the systolic portion of the pressure waveform.

In this chapter, a novel pulse contour technique that uses the peripheral pressure waveform and a transmission line model to estimate CO is developed. The transmission line model represents the pulse transmission path from the ascending aorta to the radial artery. Calibration is performed through the acquisition of the ascending aortic flow waveform using echocardiography. A patient-specific transmission line model is identified from the ascending aortic flow and the radial artery pressure. With the identified model and the radial artery pressure waveform, the ascending aortic flow is estimated. CO is calculated from the estimated ascending aortic flow.

¹ A version of this chapter has been submitted.

3.1 Introduction

CO measurement during critical care is traditionally performed using thermodilution, the direct Fick method or dye-dilution. All these methods require the placement of a pulmonary artery catheter, which is associated with increased risk and increased utilization of resources [34]. A less invasive alternative is much desired. CO can also be measured non-invasively using transthoracic echocardiography [144], [145], [169]. However, a trained technician is required to perform the measurement. Therefore, continuous CO monitoring in the intensive care unit (ICU) is not commonly performed using transthoracic echocardiography.

In ICU, patients often have an indwelling radial artery catheter inserted to monitor the vital signs. Radial artery pressure (RAP) waveform is therefore readily available. For many years, researchers have tried to derive CO from the peripheral artery pressure (PAP) waveform. Various pressure waveform analysis techniques, which are also referred to as the pulse contour analysis techniques, have been put forward [54], [74], [97], [115], [173]. Many of these techniques involve one or several measurements of CO before the monitoring commences, and a relationship between the CO values and the PAP waveform is thus derived. Such calibration is often performed using transpulmonary lithium-dilution.

In this chapter, a new CO estimation technique is developed. According to this new technique, the pulse transmission path from the ascending aorta to the radial artery is represented by a transmission line model. During calibration, the ascending aortic flow (AAF) waveform is acquired using transthoracic echocardiography. The transmission line model parameters are identified using the AAF and the RAP waveforms. The new CO estimation technique is outlined as follow:

1. Calibration
 - (a) An empirical state-space (SS) model is identified from the AAF and the RAP waveforms using subspace identification.
 - (b) The transmission line model parameters are then derived from the empirical SS model.
2. Estimation
 - (a) The transfer function from the AAF to the RAP is calculated from the identified model parameters.

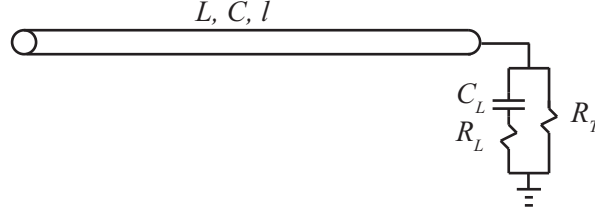


Figure 3.1: A lossless transmission line terminated by a complex load: L is the line inductance; C is the line capacitance; l is the line length; C_L is the load capacitance; R_L is the load resistance; R_T is the terminating resistance.

- (b) The AAF is estimated from the RAP through the inverse of the identified transfer function
- (c) CO is calculated from the area-time integral of the model-estimated AAF waveform.

This new technique has two advantages compared to previous techniques. First, the calibration is performed using transthoracic echocardiography and is completely non-invasive. Second, assuming that the flow waveform contains more information than the CO value, then the identified model should be able to describe the pressure-flow dynamics more precisely.

The transmission line model consists of a single uniform lossless line terminated by a complex load (Fig. 3.1). The applicability of this model has been described elsewhere [14], [15]. The analogy between this model and the pulse transmission path is explained in Appendix A. In this chapter, the electric terms are used instead of the fluid dynamic terms. A SS representation of this model based on the finite-element method [96] is developed. In this representation, the unknown entries of the system matrices are linear functions of (the reciprocals of) the transmission line model parameters.

An empirical SS model can be identified from the input and output data using subspace identification [39], [99], but it is often more useful to identify a SS model with physical meaning. The reason for this is one may be interested in identifying the physical parameters, or one may want to incorporate additional knowledge about the system into the identification process. Recently, Kind et al. [85] used the three- and four-element Windkessel model to describe the arterial system, and proposed a method to derive the Windkessel parameters from the empirical SS model. This method was specifically designed for the three- and four-element Windkessel model. Xie and Ljung [175] proposed a more general framework to identify a physical SS model

from an empirical SS model. In this framework, the transformation matrix between the empirical SS model and the physical SS model is found through iterative bilinear regression. It was suggested that this framework is suitable when the system matrices of the physical SS model have a small number of unknown entries or a special structure [102], [175].

In this chapter, it is proposed that this framework is also suitable when the unknown entries of the system matrices are linear functions of a small number of the physical model parameters. An identification method based on this framework is developed. Since this method involves black-box identification (subspace identification) and a model structure with physical meaning (the transmission line model), it is a grey-box identification method.

In the Methods section, the followings are presented:

1. the derivation of the SS representation of the transmission line model,
2. the derivation of the physiological ranges of the physical model parameters,
3. the local identifiability of the proposed SS model,
4. the grey-box identification method, and
5. the estimated bias and variances of the proposed grey-box identification method,
6. the performance of the proposed grey-box identification method on simulated data,
7. the CO estimation technique.

In the Results section, the followings are presented:

- the limits of agreement between the proposed CO estimation technique and the more well-established CO estimation technique using transthoracic echocardiography. The data were collected from 5 infant patients during their stay in ICU after cardiac surgeries.

3.2 Methods

3.2.1 Derivation of the state-space representation of the transmission line model

Equations of a lossless transmission line terminated by a complex load

The voltage and the current of a transmission line are described by the following equations:

$$-\frac{\partial V(x,t)}{\partial x} = L \frac{\partial I(x,t)}{\partial t} \quad (3.1)$$

$$-\frac{\partial I(x,t)}{\partial x} = C \frac{\partial V(x,t)}{\partial t} \quad (3.2)$$

where V is the voltage, I is the current, L is the line inductance, C is the line capacitance, x is the spatial index and t is the time index. The transmission line equations are analogous to the one-dimensional Navier-Stokes equations with the voltage corresponds to the pressure and the current corresponds to the flow (Appendix A).

The complex load at the end of the line is described by the following equations:

$$C_L \frac{d\Phi_c}{dt} = I(l,t) - \frac{V(l,t)}{R_T} \quad (3.3)$$

$$I(l,t) = \left(\frac{1}{R_T} + \frac{1}{R_L} \right) V(l,t) - \frac{1}{R_L} \Phi_c \quad (3.4)$$

where C_L is the load capacitance, R_L is the load resistance, R_T is the terminating resistance, l is the length of the line and Φ_c is the voltage across C_L .

Finite element representation of the transmission line model

In the finite element method, voltage and current are evaluated at a finite number of nodes. Each voltage node is placed between two current nodes. Voltage is evaluated at half a time step before and after current. The transmission line equations (3.1) and (3.2) can be approximated using the finite element method as described by Lee et al. [96]:

$$V_j^{n+1} = K_3 V_j^n - K_4 (I_{j+1}^{n+\frac{1}{2}} - I_j^{n+\frac{1}{2}}) \quad (3.5)$$

$$I_{j+1}^{n+\frac{1}{2}} = K_1 I_{j+1}^{n-\frac{1}{2}} - K_2 (V_{j+1}^n - V_j^n) \quad (3.6)$$

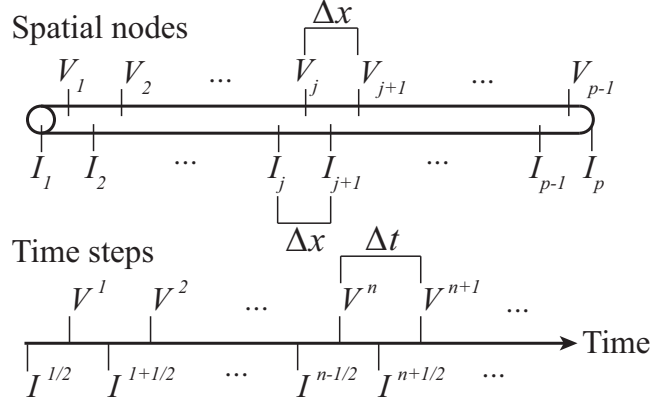


Figure 3.2: The indexing for the current and the voltage in the finite element representation: the superscript indicates the time step and the subscript indicates the spatial node; n is used to indicate the time step; j is used to indicate the spatial node; $p - 1$ indicates the last voltage node and p indicates the last current node; Δx is the distance between two current nodes or two voltage nodes; Δt is the duration of each time step.

where j indicates the node and n indicate the time step (Fig. 3.2). K_1 to K_4 are given by

$$K_1 = 1 \quad (3.7)$$

$$K_2 = \frac{\Delta t}{L\Delta x} \quad (3.8)$$

$$K_3 = 1 \quad (3.9)$$

$$K_4 = \frac{\Delta t}{C\Delta x} \quad (3.10)$$

For numerical stability, this approximation scheme requires [96]:

$$\mu \leq \frac{\Delta x}{\Delta t} \quad (3.11)$$

where μ is the wave propagation speed. For a lossless transmission line, μ is given by:

$$\mu = \frac{1}{LC} \quad (3.12)$$

Equations (3.3) and (3.4) are approximated as follows:

$$\begin{aligned}\Phi_c^{n+1} &= \frac{\Delta t}{C_L} I_p^{n+\frac{1}{2}} \\ &- \frac{\Delta t}{2C_L R_T} (V_{p-1}^{n+1} + V_{p-1}^n) + \Phi_c^n\end{aligned}\quad (3.13)$$

$$I_p^{n+\frac{1}{2}} = \left(\frac{1}{R_T} + \frac{1}{R_L} \right) V_{p-1}^n - \frac{1}{R_L} \Phi_c^n \quad (3.14)$$

where $p-1$ indicates the last voltage node and p indicates the last current node (Fig. 3.2).

State-space representation of the finite element transmission line model

Since the time index for I is arbitrary, $I^{n-\frac{1}{2}}$ and $I^{n+\frac{1}{2}}$ can be re-indexed as I^n and I^{n+1} respectively. Equations (3.5), (3.6), (3.13) and (3.14) are rewritten as follow:

$$V_j^{n+1} = K_3 V_i^n - K_4 (I_{j+1}^{n+1} - I_j^{n+1}) \quad (3.15)$$

$$I_{j+1}^{n+1} = K_1 I_{j+1}^n - K_2 (V_{j+1}^n - V_j^n) \quad (3.16)$$

$$\begin{aligned}\Phi_c^{n+1} &= \frac{\Delta t}{C_L} I_p^{n+1} \\ &- \frac{\Delta t}{2C_L R_T} (V_{p-1}^{n+1} + V_{p-1}^n) + \Phi_c^n\end{aligned}\quad (3.17)$$

$$I_p^{n+1} = \left(\frac{1}{R_T} + \frac{1}{R_L} \right) V_{p-1}^n - \frac{1}{R_L} \Phi_c^n \quad (3.18)$$

It should be noted that I^n represents current that is evaluated at half a time step later than V^n .

By approximating, on the right-hand side, I^{n+1} with I^n , V_{p-1}^{n+1} with V_{p-1}^n , and V_{p-1}^n with V_{p-1}^{n-1} , equations (3.15) and (3.17) can be written as

$$V_j^{n+1} = K_3 V_j^n - K_4 (I_{j+1}^n - I_j^n) \quad (3.19)$$

$$\Phi_c^{n+1} = \frac{\Delta t}{C_L} I_p^n - \frac{\Delta t}{2C_L R_T} (V_{p-1}^n + V_{p-1}^{n-1}) + \Phi_c^n \quad (3.20)$$

Intuitively, this approximation requires Δt to be small. Similar requirement on Δt is also imposed by the inequality in (3.11).

Equations (3.16), (3.18)-(3.20), with the current at the beginning of the line as the input (u) and the voltage at the end of the line as the output

(y), can then be written in the SS form:

$$\mathbf{x}(n+1) = \mathbf{A}\mathbf{x}(n) + \mathbf{B}u(n) \quad (3.21)$$

$$y(n) = \mathbf{C}\mathbf{x}(n) \quad (3.22)$$

with

$$u(n) = I_1(n) = I_1^n \quad (3.23)$$

$$y(n) = V_{p-1}(n) = V_{p-1}^n \quad (3.24)$$

$$\mathbf{x}(n) = \begin{bmatrix} V_1(n) \\ I_2(n) \\ V_2(n) \\ I_3(n) \\ \vdots \\ V_{p-1}(n) \\ I_p(n) \\ \Phi_c(n) \\ V_{p-1}(n-1) \end{bmatrix} = \begin{bmatrix} V_1^n \\ I_2^n \\ V_2^n \\ I_3^n \\ \vdots \\ V_{p-1}^n \\ I_p^n \\ \Phi_c^n \\ V_{p-1}^{n-1} \end{bmatrix} \quad (3.25)$$

$$\mathbf{A} = \begin{bmatrix} K_3 & -K_4 & 0 & & \dots & & & 0 \\ K_2 & K_1 & -K_2 & 0 & & \dots & & 0 \\ 0 & K_4 & K_3 & -K_4 & 0 & & \dots & 0 \\ \vdots & \ddots & \ddots & \ddots & \ddots & \ddots & \dots & \vdots \\ 0 & \dots & 0 & K_2 & K_1 & -K_2 & 0 & 0 \\ 0 & & \dots & 0 & K_4 & K_3 & -K_4 & 0 \\ 0 & & \dots & & 0 & (\alpha + A_1) & 0 & -A_1 \\ 0 & & \dots & & 0 & -\frac{\alpha A_2}{2} & A_2 & 1 \\ 0 & & \dots & & 0 & 1 & 0 & 0 \end{bmatrix} \quad (3.26)$$

$$\mathbf{B} = \begin{bmatrix} K_4 \\ 0 \\ \vdots \\ 0 \end{bmatrix} \quad (3.27)$$

$$\mathbf{C} = \begin{bmatrix} 0 & \dots & 0 & 1 & 0 & 0 & 0 \end{bmatrix} \quad (3.28)$$

where

$$\alpha = \frac{1}{R_T} \quad (3.29)$$

$$A_1 = \frac{1}{R_L} \quad (3.30)$$

$$A_2 = \frac{\Delta t}{C_L} \quad (3.31)$$

The system order is $2p$.

The terminating resistance R_T corresponds to the peripheral resistance. Peripheral resistance is calculated as the mean aortic pressure divided by the cardiac output [119]. It is often assumed that mean pressure stays the same along the arterial tree. Cardiac output is the same as mean aortic flow. Therefore, peripheral resistance can also be approximated as the mean pressure at any location along the arterial tree divided by the mean aortic flow. In analogy, R_T can be approximated as:

$$R_T = \frac{\bar{V}_{p-1}}{\bar{I}_1} \quad (3.32)$$

The remaining unknowns in the system matrices are:

$$\theta = \begin{bmatrix} K_2 & K_4 & A_1 & A_2 \end{bmatrix} \quad (3.33)$$

and the known entries are:

$$\psi = \begin{bmatrix} K_1 & K_3 & 1 \end{bmatrix} \quad (3.34)$$

Since Δx is $l/(p-1)$, the total line inductance (L_{tot}) and the total line capacitance (C_{tot}) can be retrieved from K_2 and K_4 :

$$L_{\text{tot}} = L \times l = \frac{\Delta t(p-1)}{K_2} \quad (3.35)$$

$$C_{\text{tot}} = C \times l = \frac{\Delta t(p-1)}{K_4} \quad (3.36)$$

R_L and C_L can be retrieved from A_1 and A_2 .

3.2.2 Physiological ranges of the physical model parameters

The physiological ranges of C_{tot} , C_L , the characteristic impedance of the line (Z_{ch}) and the ratio Z_{ch}/R_T are given in Table 3.1. These ranges were derived from the values found in literature.

As viewed from the ventricles, the arterial system appears to be minimally reflective at high frequencies [160]. Therefore, it can be assumed that Z_{ch} matches the load impedance at high frequencies. The following relation thus holds:

$$\frac{1}{R_L} = \frac{1}{Z_{ch}} - \frac{1}{R_T} \quad (3.37)$$

Traditionally, Z_{ch} is estimated from the input impedance, as calculated from the aortic pressure and flow, of the arterial system [119]. It has been shown that Z_{ch} for a group of children aged 0.8 to 4 years was in the range of 0.08–0.6 mmHg/cm³, and Z_{ch} decreases with age [26]. It is then deduced that Z_{ch} for infants is in the range of 0.08–2 mmHg/cm³.

The total arterial compliance (TAC) defined by the Windkessel model represents the collective compliance of the arterial system [98]. In the transmission line model, the sum of C_{tot} and C_L also represents the collective compliance of the arterial system. Therefore, it can be assumed that TAC approximates the sum of C_{tot} and C_L . It has been shown TAC for a group of children aged 3 to 12 years was 0.71 cm³/mmHg [139]. It has also been shown that TAC increases with age among children because of the increase in the arterial size [143]. It is then deduced that TAC for infants is in the range of 0.01–0.7 cm³/mmHg. In a previous modelling study on data collected from open-chest dogs [28], it was found that the ratio of C_{tot} to C_L was about 0.7 to 1. Assuming the same ratio is applicable to human infants, C_{tot} and C_L for infants are in the range of 0.01–0.5 cm³/mmHg.

It has also been shown that the ratio of Z_{ch} to R_T for a group of children aged 0.8 to 4 years was in the range of 0.05–0.23, and this ratio decreases with age [26]. It is then deduced that the Z_{ch} to R_T ratio for infants is in the range 0.05–0.5.

The ranges of L_{tot} , R_T and R_L can be calculated from the ranges of C_{tot} , Z_{ch} and Z_{ch}/R_T .

3.2.3 Local identifiability of the proposed state-space model

In the proposed SS model, the unknown physical model parameters are C_{tot} , L_{tot} , C_L and R_L . To investigate the local identifiability of this model with respect to these parameters, a method proposed by Dötsch and Van den Hof [42] was used. If the model described by equations (3.21) to (3.31) is stable, then the rank of

$$\mathbf{C_d P C_d}^T \quad (3.38)$$

C_{tot}	0.01–0.5 cm ³ /mmHg
C_L	0.01–0.5 cm ³ /mmHg
Z_{ch}	0.08–2 mmHgs/cm ³
Z_{ch}/R_T	0.05–0.5 mmHgs/cm ³

Table 3.1: Physiological ranges of the physical model parameters: C_{tot} is the total line capacitance; C_L is the load capacitance; Z_{ch} is the characteristic impedance; R_T is the terminating resistance.

equals the number of parameters if and only if the model is locally identifiable with respect to these parameters. \mathbf{P} is the solution to the Lyapunov equation

$$\mathbf{P} = \mathbf{A}_d \mathbf{P} \mathbf{A}_d^T + \mathbf{B}_d \mathbf{B}_d^T \quad (3.39)$$

where \mathbf{A}_d , \mathbf{B}_d and \mathbf{C}_d are given by

$$\mathbf{A}_d = \begin{bmatrix} \mathbf{A} & 0 & 0 & 0 & 0 \\ \frac{\partial \mathbf{A}}{\partial C_{\text{tot}}} & \mathbf{A} & 0 & 0 & 0 \\ \frac{\partial \mathbf{A}}{\partial L_{\text{tot}}} & 0 & \mathbf{A} & 0 & 0 \\ \frac{\partial \mathbf{A}}{\partial C_L} & 0 & 0 & \mathbf{A} & 0 \\ \frac{\partial \mathbf{A}}{\partial R_L} & 0 & 0 & 0 & \mathbf{A} \end{bmatrix} \quad (3.40)$$

$$\mathbf{B}_d = \begin{bmatrix} \mathbf{B} \\ \frac{\partial \mathbf{B}}{\partial C_{\text{tot}}} \\ \frac{\partial \mathbf{B}}{\partial L_{\text{tot}}} \\ \frac{\partial \mathbf{B}}{\partial C_L} \\ \frac{\partial \mathbf{B}}{\partial R_L} \end{bmatrix} \quad (3.41)$$

$$\mathbf{C}_d = \begin{bmatrix} \frac{\partial \mathbf{C}}{\partial C_{\text{tot}}} & \mathbf{C} & 0 & 0 & 0 \\ \frac{\partial \mathbf{C}}{\partial L_{\text{tot}}} & 0 & \mathbf{C} & 0 & 0 \\ \frac{\partial \mathbf{C}}{\partial C_L} & 0 & 0 & \mathbf{C} & 0 \\ \frac{\partial \mathbf{C}}{\partial R_L} & 0 & 0 & 0 & \mathbf{C} \end{bmatrix} \quad (3.42)$$

$$(3.43)$$

For a 2-element transmission line model,

$$\frac{\partial \mathbf{A}}{\partial C_{\text{tot}}} = \begin{bmatrix} 0 & \frac{2\Delta t}{C_{\text{tot}}^2} & 0 & 0 & 0 & 0 \\ 0 & 0 & 0 & 0 & 0 & 0 \\ 0 & -\frac{2\Delta t}{C_{\text{tot}}^2} & 0 & \frac{2\Delta t}{C_{\text{tot}}^2} & 0 & 0 \\ 0 & 0 & 0 & 0 & 0 & 0 \\ 0 & 0 & 0 & 0 & 0 & 0 \\ 0 & 0 & 0 & 0 & 0 & 0 \end{bmatrix} \quad (3.44)$$

$$\frac{\partial \mathbf{A}}{\partial L_{\text{tot}}} = \begin{bmatrix} 0 & 0 & 0 & 0 & 0 & 0 \\ -\frac{2\Delta t}{L_{\text{tot}}^2} & 0 & \frac{2\Delta t}{L_{\text{tot}}^2} & 0 & 0 & 0 \\ 0 & 0 & 0 & 0 & 0 & 0 \\ 0 & 0 & 0 & 0 & 0 & 0 \\ 0 & 0 & 0 & 0 & 0 & 0 \\ 0 & 0 & 0 & 0 & 0 & 0 \end{bmatrix} \quad (3.45)$$

$$\frac{\partial \mathbf{A}}{\partial C_L} = \begin{bmatrix} 0 & 0 & 0 & 0 & 0 & 0 \\ 0 & 0 & 0 & 0 & 0 & 0 \\ 0 & 0 & 0 & 0 & 0 & 0 \\ 0 & 0 & 0 & 0 & 0 & 0 \\ 0 & 0 & \frac{\Delta t}{2\alpha C_L^2} & -\frac{\Delta t}{C_L^2} & 0 & \frac{\Delta t}{2\alpha C_L^2} \\ 0 & 0 & 0 & 0 & 0 & 0 \end{bmatrix} \quad (3.46)$$

$$\frac{\partial \mathbf{A}}{\partial R_L} = \begin{bmatrix} 0 & 0 & 0 & 0 & 0 & 0 \\ 0 & 0 & 0 & 0 & 0 & 0 \\ 0 & 0 & 0 & 0 & 0 & 0 \\ 0 & 0 & -\frac{1}{R_L^2} & 0 & \frac{1}{R_L^2} & 0 \\ 0 & 0 & 0 & 0 & 0 & 0 \\ 0 & 0 & 0 & 0 & 0 & 0 \end{bmatrix} \quad (3.47)$$

$$\frac{\partial \mathbf{B}}{\partial C_{\text{tot}}} = \begin{bmatrix} -\frac{2\Delta t}{C_{\text{tot}}^2} \\ 0 \\ 0 \\ 0 \\ 0 \\ 0 \end{bmatrix} \quad (3.48)$$

$$\frac{\partial \mathbf{B}}{\partial L_{\text{tot}}} = \frac{\partial \mathbf{B}}{\partial C_L} = \frac{\partial \mathbf{B}}{\partial R_L} = \begin{bmatrix} 0 \\ 0 \\ 0 \\ 0 \\ 0 \\ 0 \end{bmatrix} \quad (3.49)$$

$$\frac{\partial \mathbf{C}}{\partial C_{\text{tot}}} = \frac{\partial \mathbf{C}}{\partial L_{\text{tot}}} = \frac{\partial \mathbf{C}}{\partial C_L} = \frac{\partial \mathbf{C}}{\partial R_L} \quad (3.50)$$

$$= \begin{bmatrix} 0 & 0 & 0 & 0 & 0 & 0 \end{bmatrix} \quad (3.51)$$

\mathbf{A}_d , \mathbf{B}_d and \mathbf{C}_d for model with more elements can be derived easily.

Local identifiability test for the 2-, 3-, 4- and 5-element models were performed. Values of C_{tot} , C_L , Z_{ch} and Z_{ch}/R_T were randomly chosen from the ranges given in Table 3.1. L_{tot} , R_T and R_L were calculated from the chosen values.

The eigenvalues of \mathbf{A} and the rank of $\mathbf{C}_d \mathbf{P} \mathbf{C}_d^T$ were found. The model was stable if all the eigenvalues of \mathbf{A} were inside the unit circle. 5000 different sets of parameter values were tested.

Δt was chosen to be 10^{-4} s, 10^{-5} s and 10^{-6} s. It was found that some of the models were unstable (Table 3.2). The number of unstable models increases as Δt increases, and as number of the elements increases. This may be related to the requirement on Δt and Δx given by the inequality in (3.11).

However, it is reasonable to assume that the pulse transmission path from the AAF to the RAP is a stable system and would be represented by a stable model. In all cases, if the model was stable, the rank of $\mathbf{C}_d \mathbf{P} \mathbf{C}_d^T$ was 4.

3.2.4 Grey-box identification

Framework of the grey-box identification

The physical SS model ($\mathbf{A}(\theta)$, $\mathbf{B}(\theta)$, $\mathbf{C}(\theta)$) that describes a lossless transmission line terminated by a complex load has been described in the previous section and is given by equations (3.21)-(3.31). An empirical SS model ($\hat{\mathbf{A}}$, $\hat{\mathbf{B}}$, $\hat{\mathbf{C}}$) is identified from the input, $I_1(n)$, and the output, $V_{p-1}(n)$, using subspace identification. The transformation matrix \mathbf{T} relates the subspace-identified empirical SS model and the physical SS model as follows:

$$\mathbf{T}^{-1} \mathbf{A}(\theta) \mathbf{T} = \hat{\mathbf{A}} \quad (3.52)$$

	Number of stable model
$\Delta t = 10^{-4}$, 2-element	5000
$\Delta t = 10^{-4}$, 3-element	4942
$\Delta t = 10^{-4}$, 4-element	4606
$\Delta t = 10^{-4}$, 5-element	3798
$\Delta t = 10^{-5}$, 2-element	5000
$\Delta t = 10^{-5}$, 3-element	5000
$\Delta t = 10^{-5}$, 4-element	4990
$\Delta t = 10^{-5}$, 5-element	4954
$\Delta t = 10^{-6}$, 2-element	5000
$\Delta t = 10^{-6}$, 3-element	5000
$\Delta t = 10^{-6}$, 4-element	5000
$\Delta t = 10^{-6}$, 5-element	5000

Table 3.2: The number of stable models for different time steps and numbers of elements: Δt is the time step.

$$\mathbf{T}^{-1}\mathbf{B}(\theta) = \hat{\mathbf{B}} \quad (3.53)$$

$$\mathbf{C}(\theta)\mathbf{T} = \hat{\mathbf{C}} \quad (3.54)$$

In the framework proposed by Xie and Ljung [175], \mathbf{T} and θ are found by minimizing the error of equations (3.52)-(3.54) through iterative bilinear regression. The error criterion is defined as

$$\begin{aligned} e = & \left\| \mathbf{T}\hat{\mathbf{A}} - \mathbf{A}(\theta)\mathbf{T} \right\|_F^2 \\ & + \left\| \mathbf{B}(\theta) - \mathbf{T}\hat{\mathbf{B}} \right\|_F^2 + \left\| \hat{\mathbf{C}} - \mathbf{C}(\theta)\mathbf{T} \right\|_F^2 \end{aligned} \quad (3.55)$$

where $\|\cdot\|$ is the Frobenius norm. \mathbf{T} and θ are updated alternatively by applying linear regression on equations (3.52)-(3.54). The iterative search begins with an initial estimate of θ .

Subspace identification using N4SID

The N4SID algorithm has been described in [165]. In brief, an extended observability matrix is determined from the projection of the future outputs onto the past and future inputs and the past outputs. The system matrices are then determined from a set of linear equations, which is written in terms of the extended observability matrix, inputs and outputs.

The Matlab algorithm **N4SID** was used in this thesis.

Derivation of θ from $\hat{\mathbf{A}}$, $\hat{\mathbf{B}}$, $\hat{\mathbf{C}}$

Equations (3.52)-(3.54) can be written in terms of the vectorized \mathbf{T} as follows:

$$\begin{bmatrix} \hat{\mathbf{A}}^T \otimes I - I \otimes \mathbf{A}(\theta) \\ \hat{\mathbf{B}}^T \otimes I \\ I \otimes \mathbf{C}(\theta) \end{bmatrix} \text{vec}(\mathbf{T}) = \begin{bmatrix} 0 \\ \mathbf{B}(\theta) \\ \text{vec}(\hat{\mathbf{C}}) \end{bmatrix} \quad (3.56)$$

where \otimes denotes the Kronecker product.

Equations (3.52) and (3.53) can also be written in terms of the vectorized $\mathbf{A}(\theta)$ and $\mathbf{B}(\theta)$ respectively

$$[\mathbf{T}^T \otimes I] \text{vec}(\mathbf{A}(\theta)) = \mathbf{T} \hat{\mathbf{A}} \quad (3.57)$$

$$\mathbf{B}(\theta) = \mathbf{T} \hat{\mathbf{B}} \quad (3.58)$$

Since the entries in $\mathbf{A}(\theta)$ are linear functions of θ , two matrices $\mathbf{H}_{\mathbf{A}}$ and $\mathbf{G}_{\mathbf{A}}$ can be defined such that

$$\text{vec}(\mathbf{A}(\theta)) = \mathbf{H}_{\mathbf{A}} \theta^T + \mathbf{G}_{\mathbf{A}} \psi^T \quad (3.59)$$

with

$$\begin{aligned} & \text{vec}(\mathbf{A}(\theta))_{(i)} \\ &= \mathbf{H}_{\mathbf{A}(i,1)} K_2 + \mathbf{H}_{\mathbf{A}(i,2)} K_4 + \mathbf{H}_{\mathbf{A}(i,3)} A_1 + \mathbf{H}_{\mathbf{A}(i,4)} A_2 \\ &+ \mathbf{G}_{\mathbf{A}(i,1)} K_1 + \mathbf{G}_{\mathbf{A}(i,2)} K_3 + \mathbf{G}_{\mathbf{A}(i,3)} \end{aligned} \quad (3.60)$$

where (i) indicates the element at the i th row, and (i, w) indicates the element at the i th row and w th column. Two matrices $\mathbf{H}_{\mathbf{B}}$ and $\mathbf{G}_{\mathbf{B}}$ are defined similarly:

$$\mathbf{B}(\theta) = \mathbf{H}_{\mathbf{B}} \theta^T + \mathbf{G}_{\mathbf{B}} \psi^T \quad (3.61)$$

Equations (3.57) and (3.58) can then be written in terms of θ as follow

$$\begin{aligned} & \begin{bmatrix} \mathbf{T}^T \otimes I & 0 \\ 0 & I \end{bmatrix} \begin{bmatrix} \mathbf{H}_{\mathbf{A}} \\ \mathbf{H}_{\mathbf{B}} \end{bmatrix} \theta^T \\ &= \begin{bmatrix} \text{vec}(\mathbf{T} \hat{\mathbf{A}}) \\ \mathbf{T} \hat{\mathbf{B}} \end{bmatrix} - \begin{bmatrix} \mathbf{T}^T \otimes I & 0 \\ 0 & I \end{bmatrix} \begin{bmatrix} \mathbf{G}_{\mathbf{A}} \\ \mathbf{G}_{\mathbf{B}} \end{bmatrix} \psi^T \end{aligned} \quad (3.62)$$

To minimize e given in equation (3.55), iterative bilinear regressions are performed as follows:

1. A set of initial values for θ are chosen.
2. \mathbf{T} is solved for in equation (3.56) using linear regression.
3. With the updated \mathbf{T} , θ is solved for in equation (3.62) using linear regression.
4. Step 2 and 3 are repeated alternatively with the updated θ and \mathbf{T} until the gradient of e is smaller than some chosen bound.

An additional nonlinear constraint

Z_{ch} of a lossless line is given by

$$Z_{ch} = \sqrt{\frac{L}{C}} \quad (3.63)$$

As viewed from the ventricles, the arterial system appears to be minimally reflective at high frequencies [160]. Therefore, it can be assumed that the characteristic impedance of the line matches the load impedance at high frequencies. The following relation thus holds:

$$\frac{1}{R_L} = \frac{1}{Z_{ch}} - \frac{1}{R_T} \quad (3.64)$$

$$A_1 = \sqrt{\frac{K_2}{K_4}} - \alpha \quad (3.65)$$

To implement this nonlinear constraint, \mathbf{H}_A , \mathbf{H}_B , \mathbf{G}_A and \mathbf{G}_B are modified. Let K_2^- and K_4^- be the values of K_2 and K_4 found in the previous iteration. Then A_1 is approximated as

$$A_1 = \sqrt{\frac{K_2^-}{K_4^-}} - \alpha \quad (3.66)$$

A new θ is defined as

$$\theta = \begin{bmatrix} K_2 & K_4 & A_2 \end{bmatrix} \quad (3.67)$$

and a new ψ is defined as

$$\psi = \begin{bmatrix} K_1 & K_3 & 1 & A_1 \end{bmatrix} \quad (3.68)$$

\mathbf{H}_A , \mathbf{H}_B , \mathbf{G}_A and \mathbf{G}_B are re-defined accordingly. To find T and θ , iterative bilinear regression is applied on equation(3.56) and equation (3.62) with the re-defined \mathbf{H}_A , \mathbf{H}_B , \mathbf{G}_A and \mathbf{G}_B .

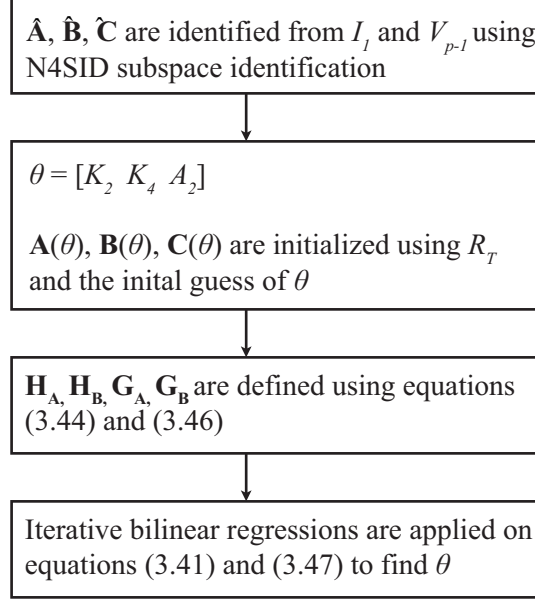


Figure 3.3: The grey-box identification algorithm: $\hat{\mathbf{A}}, \hat{\mathbf{B}}, \hat{\mathbf{C}}$ represent the empirical model; I_1 is the current at the beginning of the line or analogously the ascending aortic flow; V_{p-1} is the voltage at the end of the line or analogously the radial artery pressure; K_2, K_4 and A_2 are the unknowns of the physical model; $\mathbf{A}(\theta), \mathbf{B}(\theta), \mathbf{C}(\theta)$ represent the physical model; R_T is the terminating resistance.

Summary of the grey-box identification algorithm

The steps of the identification algorithm are shown in Figure 3.3.

3.2.5 Estimation of the bias and variance using a Monte-Carlo study

A Monte-Carlo study was performed to estimate the bias and the variance of the proposed grey-box identification method. Several sets of parameter values were used as shown in Table 3.3. Δt was 10^{-4} . R_T was 10 mmHg/cm³. Number of elements was 3.

The input was the realization of a Gaussian random variable with zero mean and unit variance. The length of the realization was 10^5 and 100 realizations were used.

The estimates of the bias ($\hat{\text{Bias}}$) and the variance ($\hat{\text{Var}}$) were calculated as follows:

$$\varphi = \begin{bmatrix} C_{\text{tot}} & L_{\text{tot}} & C_L \end{bmatrix} \quad (3.69)$$

$$\hat{\text{Bias}} = \frac{1}{M} \left| \sum_{i=1}^M (\varphi_0 - \hat{\varphi}_i) \right| \quad (3.70)$$

$$\hat{\text{Var}} = \frac{1}{M-k} \sum_{i=1}^M (\hat{\varphi}_i - \bar{\varphi})^2 \quad (3.71)$$

where M is the number of realization, k is the number of the parameters, φ_0 is the set of parameter values used to generate the output, $\hat{\varphi}$ is the set of parameter values estimated from each realization, and the bar denotes the mean value. The estimated bias and variance are presented in Table 3.3.

The estimated bias was small and the variance was negligible for the small parameter values. The proposed grey-box identification method thus provides an ideal estimator for the small parameter values. For the large parameter values, the estimated bias and variance became more significant. As C_{tot} , L_{tot} and C_L increase, K_2 , K_4 and A_2 decrease (see equations (3.31),(3.35),(3.36)). Since some of the entries in $\mathbf{A}(\theta)$ are fixed at 1 (see equation (3.26)), decrease in K_2 , K_4 and A_2 makes $\mathbf{A}(\theta)$ less numerically favorable. This may explain the significant bias and variance for the large parameter values. To avoid this problem, the input and output data can be downsampled before the grey-box identification method is applied. This is illustrated in the next section.

3.2.6 Performance of the proposed grey-box identification method using simulated data

To further evaluate the performance of the proposed grey-box identification method, a simulated flow waveform (Fig.3.4) was applied as the input to the model described by equations (3.21) to (3.31). Several sets of parameter values were used as shown in Table 3.4.

The input and the model output were downsampled 5 and 10 times. The grey-box identification method was applied to the original and the downsampled input and model output. For the downsampled data, Δt was increased, and K_2 , K_4 and A_2 increased accordingly (see equations (3.31),(3.35),(3.36)). The goal of this simulation study was to decide whether

	φ_0	$\hat{\text{Bias}}$	$\hat{\text{Var}}$
C_{tot}	0.01	0.0005	2.3×10^{-10}
L_{tot}	0.01	0.0005	2.8×10^{-10}
C_L	0.02	0.0012	1.4×10^{-9}
C_{tot}	0.05	0.0015	2.2×10^{-5}
L_{tot}	0.05	0.0020	2.2×10^{-5}
C_L	0.02	0.0007	5.6×10^{-6}
C_{tot}	0.10	0.0138	0.0026
L_{tot}	0.10	0.0730	0.0161
C_L	0.02	0.0017	0.0003
C_{tot}	0.10	0.0092	0.0039
L_{tot}	0.05	0.0230	0.0012
C_L	0.05	0.0014	0.0020
C_{tot}	0.05	0.0022	0.0003
L_{tot}	0.10	0.0166	0.0042
C_L	0.05	0.0107	0.0219

Table 3.3: The estimated bias and variances: φ_0 is the set of true parameter values; $\hat{\text{Bias}}$ is the estimated bias; $\hat{\text{Var}}$ is the estimated variance; C_{tot} is the total line capacitance; L_{tot} is the total line inductance; C_L is the load capacitance.

reasonable estimates of K_2 , K_4 and A_2 , and thereby C_{tot} , L_{tot} and C_L , can be obtained using the downsampled data.

The results are presented in Table 3.4 and 3.5. For the original data, good estimates of K_2 , K_4 and A_2 , and thereby C_{tot} , L_{tot} and C_L , were obtained in all cases.

For the downsampled data, good estimates of C_{tot} , L_{tot} and C_L were obtained in all cases. Because of the downsampling, Δt increased 5 or 10 times, and K_2 , K_4 and A_2 increased 5 or 10 times accordingly. It is interesting to note that, in some cases, the estimated K_2 , K_4 and A_2 actually produced an unstable model (Table (3.5)). This was likely caused by the requirement of Δt imposed by the inequality in (3.11). However, the corresponding estimates of C_{tot} , L_{tot} and C_L were still reasonably accurate. Samples of the RAP waveforms estimated using the sets of parameter values identified from the original and the downsampled data are shown in Figure 3.5.

For the original data, the error, as evaluated by the differences between the estimated and the true parameter values, increased as the parameter values increased (Table 3.4). Similar observation was obtained in the monte-carlo study as described in the previous section. However, for the downsampled data, the error did not seem to be dependent on the parameter values (Table 3.4). This is likely due to the increase in K_2 , K_4 and A_2 , which caused $\mathbf{A}(\theta)$ to be numerically favorable.

On the other hand, as the sampling rate decreased, the error increased (Table 3.4). However, even for the 10-times downsampled data, the error was still acceptable. In this thesis, the sampling rate of the experimental data was similar to the sampling rate of the 10-times downsampled data.

3.2.7 Estimation of the cardiac output from the radial artery pressure waveform

Re-estimation of the terminating resistance

R_T corresponds to the peripheral resistance, and is altered through vasodilation and vasoconstriction, which can happen in a very short course of time. Therefore, it is necessary to re-estimate R_T when CO is estimated from the identified model during monitoring.

To re-estimate R_T , the RAP is considered to be entering a Windkessel load (Fig. 3.6). The time constant (τ) of the Windkessel load is given by

$$\tau = R_T C_{\text{wind}} \quad (3.72)$$

		Original sampling rate $\Delta t = 0.00023$		Downsampled 5 times $\Delta t = 0.0011$		Downsampled 10 times $\Delta t = 0.0023$	
	φ_0	$\hat{\varphi}$	$\hat{\varphi} - \varphi_0$	$\hat{\varphi}$	$\hat{\varphi} - \varphi_0$	$\hat{\varphi}$	$\hat{\varphi} - \varphi_0$
C_{tot}	0.05	0.050	0.0000	0.046	-0.0036	0.043	-0.0072
L_{tot}	0.05	0.050	0.0000	0.053	0.0034	0.058	0.0078
C_L	0.02	0.020	0.0000	0.023	0.0034	0.026	0.0064
C_{tot}	0.05	0.050	-0.0001	0.048	-0.0020	0.0456	-0.0044
L_{tot}	0.10	0.100	0.0001	0.1039	0.0039	0.1098	0.0098
C_L	0.02	0.020	0.0000	0.0219	0.0019	0.0238	0.0038
C_{tot}	0.10	0.1005	0.0005	0.0967	-0.0033	0.0938	-0.0062
L_{tot}	0.05	0.0497	-0.0003	0.0506	0.0006	0.0511	0.0011
C_L	0.02	0.0201	0.0001	0.0243	0.0043	0.0302	0.0102
C_{tot}	0.10	0.1025	0.0025	0.0968	-0.0032	0.0928	-0.0072
L_{tot}	0.10	0.0975	-0.0025	0.1031	0.0031	0.1075	0.0075
C_L	0.05	0.0517	0.0017	0.0531	0.0031	0.0566	0.0066

Table 3.4: Physical model parameters estimated from the simulated data: φ_0 is the set of true parameter values; $\hat{\varphi}$ is the set of estimated parameter values; C_{tot} is the total line capacitance; L_{tot} is the total line inductance; C_L is the load capacitance; Δt is the time step.

		Original sampling rate $\Delta t = 0.00023$		Downsampled 5 times $\Delta t = 0.0011$		Downsampled 10 times $\Delta t = 0.0023$	
	θ_0	$\hat{\theta}$	Stablility	$\hat{\theta}$	Stablility	$\hat{\theta}$	Stablility
K_4	0.0136	0.0136	stable	0.0732	unstable	0.1587	unstable
K_2	0.0136	0.0136		0.0636		0.1175	
A_2	0.0113	0.0113		0.0484		0.0858	
K_4	0.0136	0.0136	stable	0.0708	unstable	0.149	unstable
K_2	0.0068	0.0068		0.0327		0.0619	
A_2	0.0113	0.0113		0.0516		0.0952	
K_4	0.0068	0.0068	stable	0.0351	unstable	0.0724	unstable
K_2	0.0136	0.0137		0.0671		0.1330	
A_2	0.0113	0.0112		0.0466		0.0749	
K_4	0.0068	0.0066	stable	0.0351	unstable	0.0732	unstable
K_2	0.0068	0.0070		0.0330		0.0632	
A_2	0.0045	0.0044		0.0213		0.0400	

Table 3.5: Stability of the models identified from the simulated data: K_2 , K_4 and A_2 are the unknowns of the physical model; θ_0 is the set of the true values of the unknowns at the original sampling rate; $\hat{\theta}$ is the set of the estimated values of the unknowns; Δt is the time step.

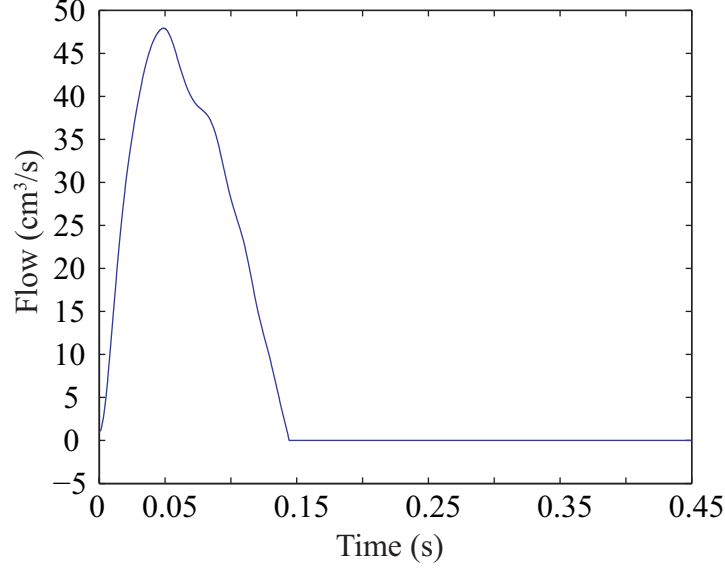


Figure 3.4: The simulated flow waveform

where C_{wind} is the Windkessel compliance. τ can be estimated from the pressure waveform using the area method as described by Liu et al. [98]:

$$\tau = \frac{A_{12}}{P_1 - P_2} \quad (3.73)$$

where P_1 is the pressure at the beginning of the diastolic decay, P_2 is the end-diastolic pressure, A_{12} is the area under the pressure waveform between P_1 and P_2 (Fig. 3.7).

During calibration, τ is measured from the RAP waveform, then C_{wind} is calculated using equation (3.72).

When monitoring CO, it is assumed that C_{wind} is constant. The updated τ is measured from the RAP waveform, then R_T is re-estimated using equation (3.72).

Transfer function from the ascending aortic flow to the radial artery pressure

The transfer function (M) from the AAF to the RAP is given by [14]:

$$M(z) = \frac{Z_{ch}(1 + \Gamma)z^d}{z^{2d} - \Gamma} \quad (3.74)$$

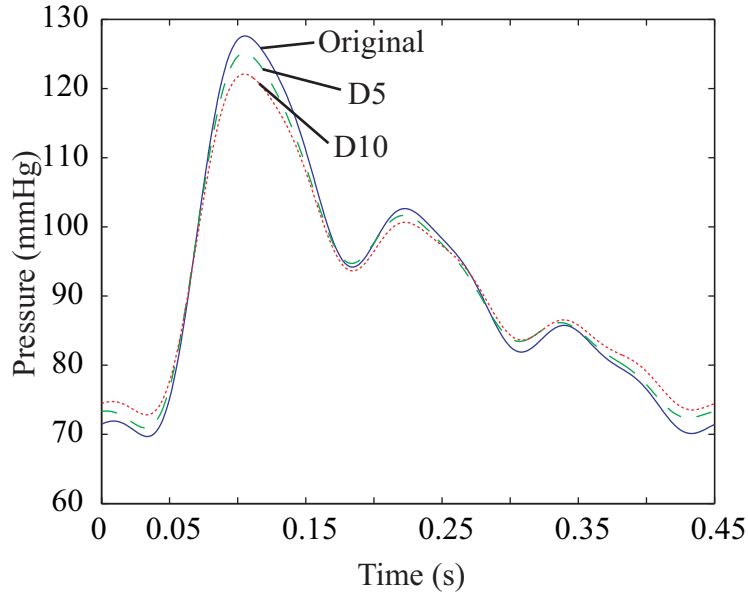


Figure 3.5: The estimated radial artery pressure waveforms: original indicates the waveform identified from the original data; D5 indicates the waveform identified from the 5-times downsampled data; D10 indicates the waveform identified from the 10-times downsampled data.

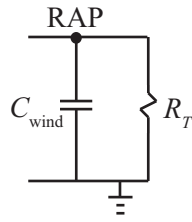


Figure 3.6: The re-estimation of R_T by considering the radial artery pressure waveform as entering a Windkessel load: RAP is the radial artery pressure; C_{wind} is the Windkessel compliance; R_T is the terminating resistance.

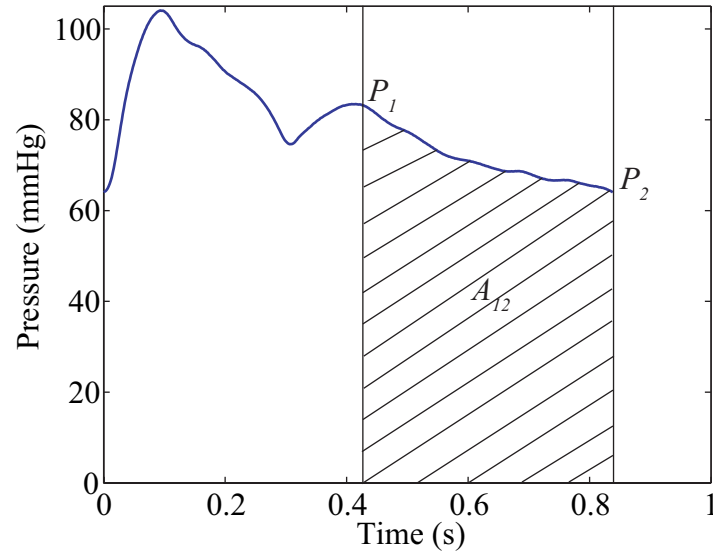


Figure 3.7: The determination of the time constant of the Windkessel load using the area method: P_1 is the pressure at the beginning of the diastolic decay; P_2 is the end-diastolic pressure; A_{12} is the area under the pressure waveform between P_1 and P_2 .

where z is the z -variable, Γ is the reflection coefficient at the line-load interface and d is the discrete time delay between the AAF and the RAP. Since the wave propagation speed for a lossless line is $1/\sqrt{LC}$, d is calculated as:

$$d = \frac{l}{1/\sqrt{LC}} \times \frac{1}{\Delta t} = \frac{\sqrt{(L \times l)(C \times l)}}{\Delta t} = \frac{p-1}{\sqrt{K_2 K_4}} \quad (3.75)$$

$M(z)$ is given in terms of C_L , R_L , Z_{ch} and R_T and d by:

$$M(z) = \frac{b_1 z^{-d} + b_2 z^{-d-1}}{1 + a_1 z^{-1} + a_2^{-2d} + a_3^{-2d-1}} \quad (3.76)$$

where

$$b_1 = \frac{2Z_{ch}(1 + 2F_s C_L R_L)}{\frac{Z_{ch}}{R_T} + 1 + 2F_s C_L (R_L + Z_{ch} + \frac{R_L Z_{ch}}{R_T})} \quad (3.77)$$

$$b_2 = \frac{2Z_{ch}(1 - 2F_s C_L R_L)}{\frac{Z_{ch}}{R_T} + 1 + 2F_s C_L (R_L + Z_{ch} + \frac{R_L Z_{ch}}{R_T})} \quad (3.78)$$

$$a_1 = \frac{\frac{Z_{ch}}{R_T} + 1 - 2F_s C_L (R_L + Z_{ch} + \frac{R_L Z_{ch}}{R_T})}{\frac{Z_{ch}}{R_T} + 1 + 2F_s C_L (R_L + Z_{ch} + \frac{R_L Z_{ch}}{R_T})} \quad (3.79)$$

$$a_2 = \frac{\frac{Z_{ch}}{R_T} - 1 - 2F_s C_L (R_L - Z_{ch} - \frac{R_L Z_{ch}}{R_T})}{\frac{Z_{ch}}{R_T} + 1 + 2F_s C_L (R_L + Z_{ch} + \frac{R_L Z_{ch}}{R_T})} \quad (3.80)$$

$$a_3 = \frac{\frac{Z_{ch}}{R_T} - 1 + 2F_s C_L (R_L - Z_{ch} - \frac{R_L Z_{ch}}{R_T})}{\frac{Z_{ch}}{R_T} + 1 + 2F_s C_L (R_L + Z_{ch} + \frac{R_L Z_{ch}}{R_T})} \quad (3.81)$$

where F_s is $1/\Delta t$. The derivation of equation (3.76) is given in Appendix C. AAF is estimated from RAP using the inverse of $M(z)$.

Calculation of cardiac output from the model-estimated ascending aortic flow waveform

CO can be calculated as the area integral (AL) of the model-estimated AAF waveform divided by its duration (D).

During calibration, CO is also estimated using echocardiography. A correction factor (β) is derived from AL and D of the model-estimated AAF waveform and CO estimated using echocardiography (CO_{echo}):

$$\beta = \frac{\text{CO}_{\text{echo}}}{\text{AL}/\text{D}} \quad (3.82)$$

During monitoring, CO estimated from the RAP (CO_{RAP}) is calculated as:

$$\text{CO}_{\text{RAP}} = \beta \frac{AL}{D} \quad (3.83)$$

Summary of the CO estimation technique

The steps of the CO estimation technique are shown in Figure 3.8.

3.3 Experiments

3.3.1 Data acquisition

This study was approved by the University of British Columbia Children's and Women's Research Ethics Board. Five children who underwent cardiac surgeries participated. Left ventricular outflow tract (LVOT) diameter was obtained using two-dimensional echocardiography. Flow velocity at the LVOT was obtained using pulsed-Doppler ultrasound (Fig. 3.9). Pressure was obtained at the radial artery from an indwelling catheter (Fig. 3.10). Velocity and pressure data were obtained simultaneously. The echocardiographic data were obtained using a GE Vivid 7 Pro ultrasound machine (GE Vingmed, Horten, Norway). The pressure data were obtained using a Philips IntelliVue MP70 Patient Monitor (Philips Healthcare, Andover, MA, the United States). Data were collected once the patients were deemed stable after the surgeries (0 h). In 4 patients, data were also collected 3 to 5 hours after (5 h). In the remaining patient, data were collected at the beginning (0 h) and 24 hours after (24 h).

3.3.2 Data processing

The envelope of the Doppler spectrum of the LVOT flow velocity was traced automatically (Fig. 3.9). The LVOT cross-sectional area was calculated from the LVOT diameter. The LVOT flow waveform was obtained by multiplying the LVOT flow velocity with the LVOT cross-sectional area. The LVOT flow waveform was used as a surrogate of the AAF waveform.

The pressure waveform showed a cyclic fluctuation with a period of about 2 to 3 second (Fig. 3.10). It was assumed that this fluctuation was due to respiration.

For the calibration and each subsequent CO measurement, five to ten consecutive beats were averaged. The number of beats averaged was chosen to include one complete respiratory cycle (Fig. 3.10).

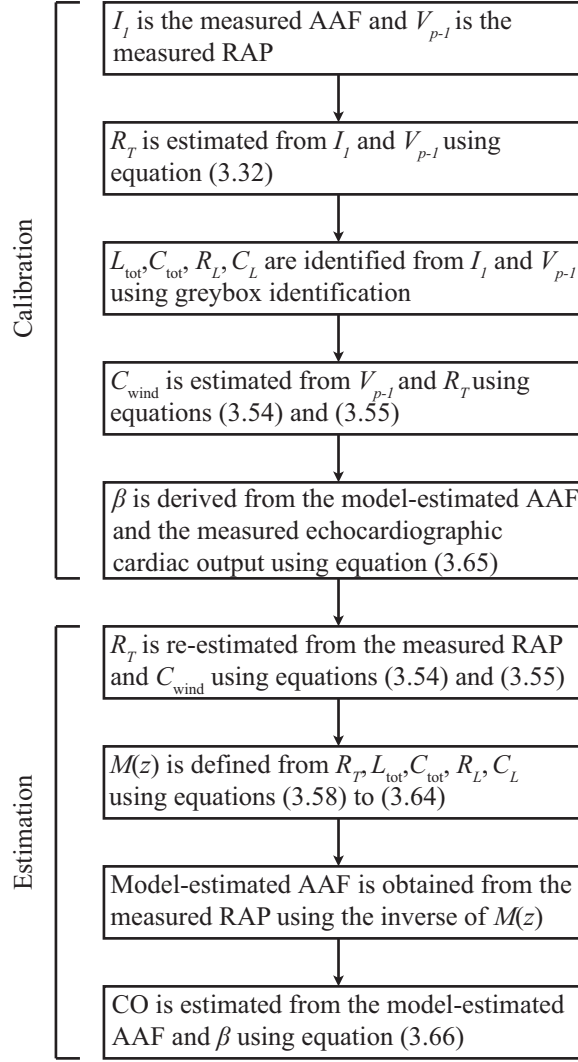


Figure 3.8: The cardiac output estimation technique: I_1 is the current at the beginning of the line; AAF is the ascending aortic flow; V_{p-1} is the voltage at the end of the line; RAP is the radial artery pressure; R_T is the terminating resistance; L_{tot} is the total line inductance; C_{tot} is the total line capacitance; R_L is the load resistance; C_L is the load capacitance; C_{wind} is the Windkessel compliance as seen by the radial artery pressure; β is a correction factor relating the cardiac output estimated by echocardiography and that estimated from the radial artery pressure; $M(z)$ is the transfer function from the ascending aortic flow to the radial artery pressure; CO is the cardiac output.

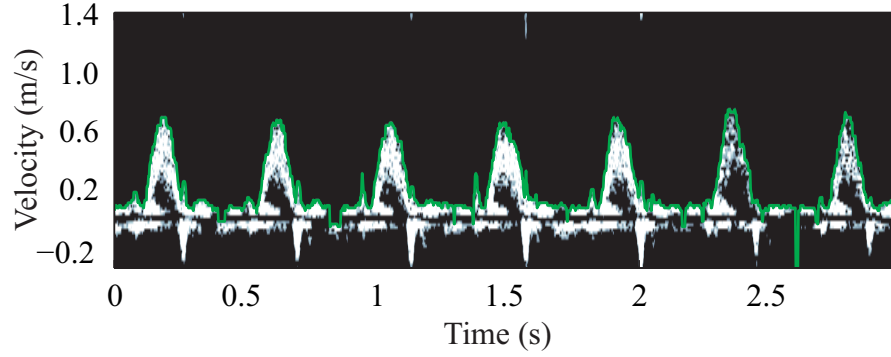


Figure 3.9: The Doppler spectrum of the LVOT flow velocity: the envelope of the spectrum was traced automatically.

For the pressure waveform, the beginning and end of each beat were marked by the end-diastolic pressures. The beginning and end of the chosen pressure beat were equalized by removing the linear component defined by these two points. For the flow waveform, only the positive flow during the ventricular ejection was considered. Zero flow was assumed after the ventricular ejection (Fig. 3.11).

The sampling rate of the flow waveform was in the range of 455 – 500 Hz (Δt was 0.0020 – 0.0022s). The sampling rate of the pressure waveform was 125 Hz (Δt was 0.0080s). The pressure waveform was upsampled to have the same sampling rate as the flow waveform.

3.3.3 Cardiac output determination

CO was estimated from the RAP waveform using the proposed technique. To evaluate the accuracy of the proposed technique, CO was also estimated using echocardiography.

Using echocardiography, each measurement of CO was calculated as the velocity-time-integral of the LVOT flow velocity waveform times the LVOT area divided by the duration of the waveform.

Each determination of CO was the average of one to three measurements of CO.

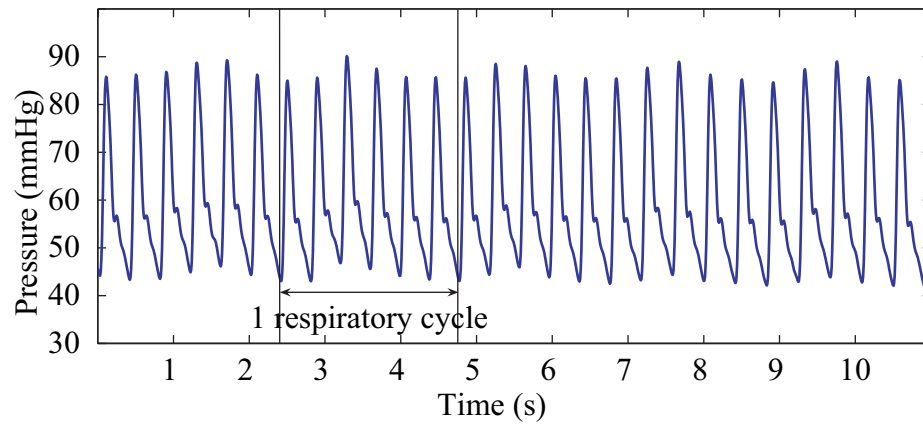


Figure 3.10: The radial artery pressure waveform: one respiratory cycle is indicated.

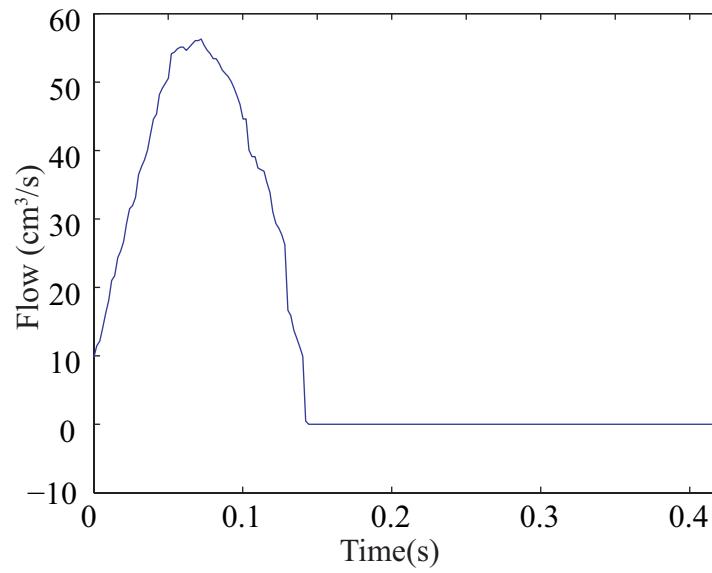


Figure 3.11: The averaged ascending aortic flow waveform: zero flow was assumed after the ventricular ejection.

Patient	Age (mo)	BSA (m ²)
1	1	0.24
2	2	0.27
3	5	0.33
4	6	0.34
5	9	0.30

Table 3.6: Demographics of patients: BSA is the body surface area.

3.4 Results

The demographics of the patients are listed in (Table 3.6).

The system order was determined during subspace identification. Singular value decomposition was performed on a matrix that has the same column space as the extended observability matrix. The number of dominant singular values corresponds to the system order. In a previous modelling study on simulated data by Kind et al. [85], it was found that for noise-free simulated data, the gap between the dominant and non-dominant singular values was easily distinguishable. However, as noise was added, this gap narrowed. For the experimental data in this thesis, the singular value decreased rather smoothly, and the gap between the dominant and non-dominant singular values was not obvious (Fig 3.12). To determine the system order, it was assumed that the physical model should have at least two elements, which corresponds to a system order of 6. A relatively significant drop of the log of the singular value could be identified between the system order of 6 to 12. It was observed that the drop usually occurred from 1 to 0. Therefore, the system order was chosen as the maximum system order with the corresponding log of singular value greater than 0.1.

The identified physical parameters are listed in Table 3.7. In all five cases, the error criterion and the model parameters converged rapidly during the iterations of bilinear regression. Samples of the convergence graphs are shown in Figure 3.13.

The CO determinations and the corresponding time of measurements are listed in Table 3.8. To evaluate the accuracy of our proposed technique, echocardiography was used as a reference method. CO_{RAP} is the CO estimated from the RAP waveform using equation (3.83). CO_{echo} is the CO estimated using echocardiography. The bias and limits of agreement are presented in terms of % error (Table 3.9), CO (Table 3.10), and cardiac index (CI) (Table 3.11) for the data collected during different time intervals. CI is

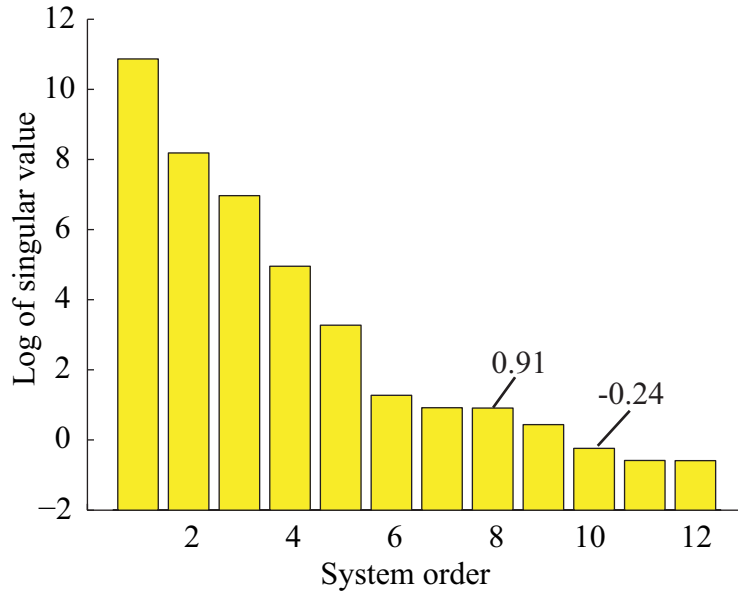


Figure 3.12: Log of singular value versus system order

Patients	C_{tot} (cm^3/mmHg)	L_{tot} ($\text{mmHg}\cdot\text{s}^2/\text{cm}^3$)	C_L (cm^3/mmHg)	R_L ($\text{mmHg}\cdot\text{s}/\text{cm}^3$)
1	0.0887	0.0559	0.0185	0.9904
2	0.0350	0.0765	0.0083	1.6793
3	0.0606	0.0597	0.0450	1.2892
4	0.0854	0.0530	0.0212	0.9490
5	0.0325	0.1356	0.0219	3.0741

Table 3.7: Identified physical model parameters: C_{tot} is the total line capacitance; L_{tot} is the total line inductance; C_L is the load capacitance; R_L is the load resistance.

Patient	Time of measurements	CO _{echo} (L/min)	CO _{RAP} (L/min)	% Difference
1	0h	0.924	0.877	5.3
	5h	0.983	0.937	4.8
2	0h	0.253	0.247	2.4
	3h	0.347	0.299	14.7
3	0h	0.776	0.754	2.8
	4h	0.994	0.979	1.5
4	0h	0.828	0.744	10.7
	5h	0.826	0.885	-6.9
5	0h	0.638	0.633	0.8
	24h	0.791	0.559	34.4

Table 3.8: Cardiac output determinations: CO_{echo} is the cardiac output determination obtained using echocardiography; CO_{RAP} is the cardiac output determination obtained from the radial artery pressure waveform.

Time of measurements	Bias (%)	Limits of agreement (%)
0 hrs	4.4	-3.2 – 12.0
0, 5 hrs	4.0	-8.0 – 16.1
0, 5, 24 hrs	7.1	-14.9 – 29.0

Table 3.9: Bias and limits of agreement in terms of % error

CO normalized to the body surface area (BSA), and it is also often measured during critical care.

The Bland-Altman plot is shown in Figure 3.14. A sample of the model-estimated AAF waveform and the corresponding measured AAF waveform are shown in Figure 3.15.

3.5 Discussion

In this study, the reference method was echocardiography. Calibration was performed only at the beginning of the data collection. For a 5-hour calibration-free period, the limits of agreement was within $\pm 17\%$. To put this into perspective, studies of other pulse contour techniques were considered. There are two relatively well-established techniques based on the pulse contour analysis [67]: PiCCO [47], [54], [64] and PulseCO [63], [84]. Many

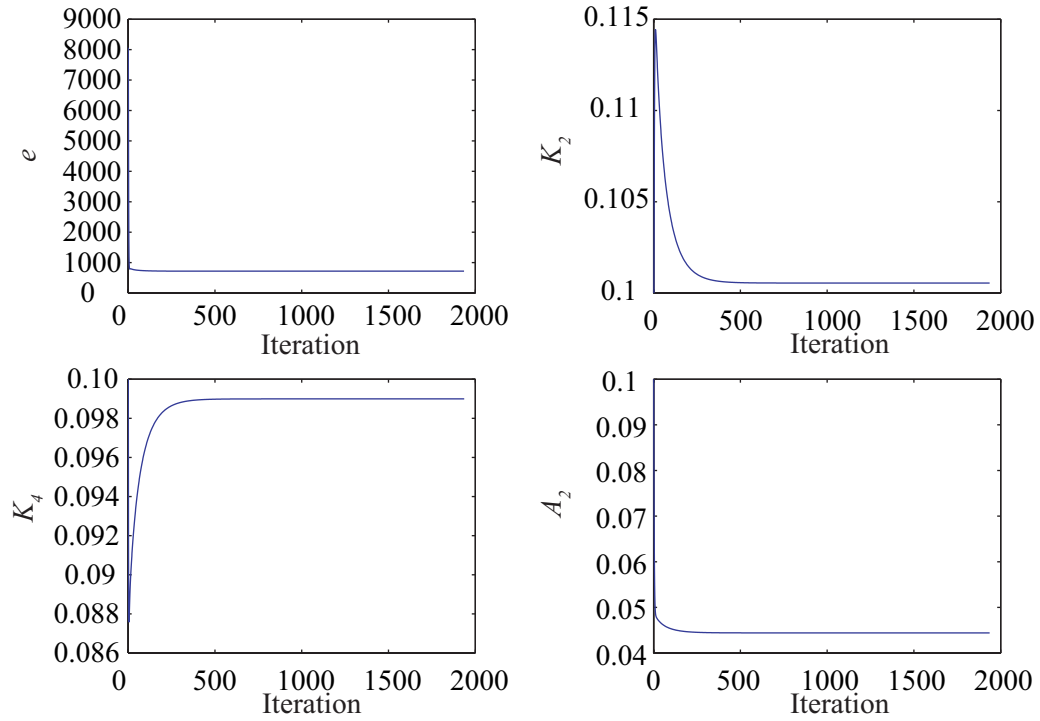


Figure 3.13: Samples of convergence graphs: e is the error criterion; K_2 , K_4 and A_2 are the unknowns of the physical model.

Time of measurements	Bias (L/min)	Limits of agreement (L/min)
0 hrs	0.033	-0.033 – 0.099
0, 5 hrs	0.024	-0.055 – 0.103
0, 5, 24 hrs	0.045	-0.104 – 0.194

Table 3.10: Bias and limits of agreement in terms of cardiac output

Time measurements	Bias (L/min/m ²)	Limits of agreement (L/min/m ²)
0 hrs	0.110	-0.098 – 0.319
0, 5 hrs	0.088	-0.169 – 0.344
0, 5, 24 hrs	0.156	-0.333 – 0.646

Table 3.11: Bias and limits of agreement in terms of cardiac index

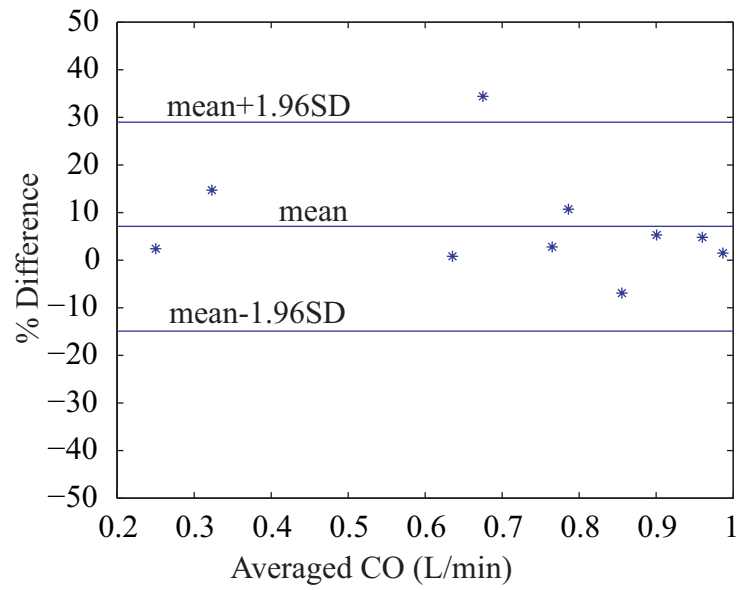


Figure 3.14: Bland-Altman plot of the cardiac output determinations obtained using the echocardiography technique and from the radial artery pressure waveform; CO is the cardiac output.

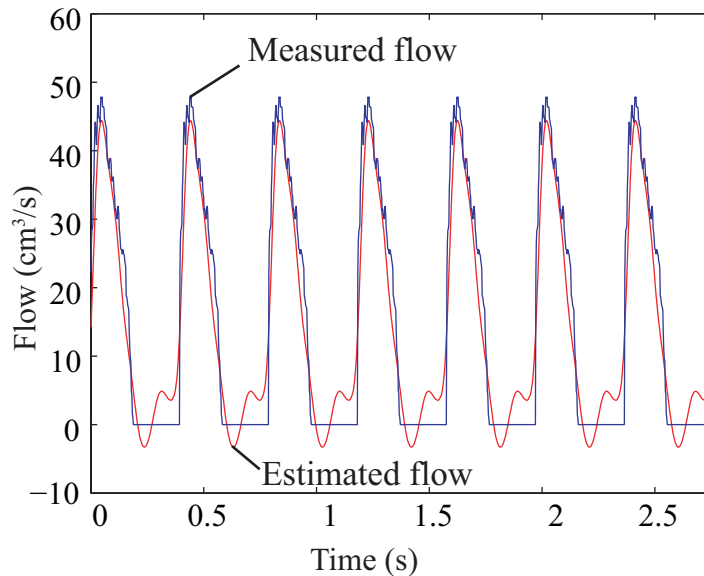


Figure 3.15: Measured and estimated ascending aortic flow waveforms

studies have been conducted to evaluate the accuracy of these techniques on different patient populations under different conditions. To make a reasonable comparison, studies conducted on similar patients and/or under similar conditions were considered. In a study of PiCCO [47], CO determinations were obtained from patients who had underwent pediatric cardiac surgeries. Calibration was performed every 4 hours. The limits of agreement of CI were found to be approximately ± 0.75 L/min/m². In a study of PulseCO [84], CO determinations were obtained from children undergoing hemodynamic evaluation in the cardiac catheterization laboratory. Data were collected in a 4-hour calibration-free period. The limits of agreement of CI were found to be approximately -0.09–0.47 L/min/m². The accuracy of our technique, in terms of limits of agreement, is comparable to the accuracies of PiCCO and PulseCO.

It has been suggested that the measurement of physiological variables often lacks precision and has an error of ± 10 –20% [36]. For example, it has been shown that thermodilution has an inherent error (variability) of 13% (average of three measurements) and 22% (single measurements) [152]. Therefore, to evaluate a new CO estimation technique with thermodilution as the reference technique, the limits of agreement are expected to exceed

$\pm 20\%$. Critchley and Critchley [36] then proposed that limits of agreement within $\pm 30\%$ are acceptable, by assuming both of the test and reference techniques have an error of 20%.

In this study, the limits of agreement including all CO determination (0h, 5h, 24h) were indeed within $\pm 30\%$. However, it was noted that, the % difference was much larger for the CO determination obtained at 24 h (Fig. 3.14). The limits of agreement excluding the last measurement (0h, 5h) were only $\pm 17\%$, and can be considered as quite ideal. It suggests that a re-calibration after 5 hours may improve the performance of the technique.

A major limitation of this study is that only two CO determinations were obtained from each patient. Therefore, the performance of the proposed technique over time cannot be evaluated. It would be necessary to determine how long the technique would stay accurate without re-calibration.

Both PiCCO and PulseCO require calibration using transpulmonary lithium-dilution or thermodilution. Transpulmonary lithium-dilution requires the placement of both central venous and arterial catheters. A major advantage of our technique is that the calibration is completely non-invasive. Since the ultrasound machine has become more compact and portable, echocardiographic examinations can be conducted in ICU with relative ease. The proposed algorithm can be implemented as a module with data transfer interfaces to the ultrasound machine and the bedside monitor.

Recently, it has been suggested that central hemodynamics can be estimated from multiple peripheral pressures [60], [107], [155]. Cardiac output estimation is thus possible using multiple peripheral pressures that can be obtained minimally-invasively or non-invasively. However, validations of these techniques have yet to be performed on human data.

Chapter 4

Measuring Aortic Pressure Waveform using Ultrasound B-Mode Imaging^{1,2}

Aortic pressure is closely related to the pathogenesis of cardiovascular diseases. A non-invasive method for the measurement of the aortic pressure waveform would be a very valuable tool for the diagnosis of cardiovascular diseases at their early stage of development. In this chapter, a method for estimating the aortic pressure waveform using B-mode imaging is proposed. A semi-automatic algorithm is developed to measure the aortic distension waveform from the B-mode images of the aortic arch acquired at a suprasternal view. A linear calibration scheme and an exponential calibration scheme are used to estimate the aortic pressure waveform from the aortic distension waveform.

4.1 Introduction

The aortic pressure waveform is different in both amplitude and morphology from the peripheral artery pressure waveform [119]. To assess the aortic pressure waveform non-invasively, the carotid artery pressure waveform obtained using applanation tonometry can be used as a surrogate to the aortic pressure waveform [82]. However, the use of applanation tonometry on the carotid artery requires substantial expertise. Recently, there has been increasing interest in estimating the pressure waveform from the distension waveform, which is the change in the arterial diameter over time. Various methods have been proposed to obtain the distension waveform

¹ A version of this chapter is under preparation for submission.

² M. Leung, G. A. Dumont, G. G. S. Sandor, M. T. Potts and J. E. Potts, "A novel method to estimate the aortic pressure waveform using B-mode ultrasound images acquired from a suprasternal view," 30th IEEE Engineering in Medicine and Biology Conference, Vancouver, 2008

using M-mode imaging [151], B-mode imaging [55,56,151], echo-tracking [86,151,153,161,166], and more recently, tissue Doppler imaging [41,61].

In medical ultrasound imaging, pulses of sound are sent into the body. The sound wave propagates through the tissue and is scattered by small changes in density. The backscattered signal is received by the transducer. Its strength is determined by the deviations within the tissue and the composition of the tissue, and its transit time is determined by the depth of the tissue. Therefore, the backscattered signal received along a scan line provides the information of the tissue layers along that line. In B-mode imaging, “B” stands for brightness. The scan line sweeps through a plane. The amplitude of the backscattered signal is displayed as a grey value. The backscattered signals received along the scan line as it sweeps through the plane are displayed side-by-side, and a two-dimensional image is thus constructed. In M-mode imaging, “M” stands for motion. Sound waves are emitted successively along a scan line. The amplitude of the backscattered signal is also displayed as a grey value. The backscattered signals received at successive times are displayed side-by-side, and thereby generates an image of tissue motion at the direction of the scan line. The principle of echo-tracking is quite different from that of B-mode and M-mode imaging. In echo-tracking, pulses of sound are emitted successively, and the returned signal from a particular echo structure, e.g. arterial wall, is identified by its amplitude or phase. The transit time of this returned signal provides information on the depth of the structure, and the movement of the structure can be obtained from the change in the transit time. Tissue Doppler imaging is based on the same principle as the conventional Doppler echocardiography, which relies on the detection of the shift in frequency of the returned signal from moving objects. In tissue Doppler imaging, the Doppler principle is used to quantify tissue motion.

Of all these methods, echo-tracking has the advantage of a high spatial resolution of about $1\text{ }\mu\text{m}$ [66]. In contrast, B-mode imaging can only achieve a moderate spatial resolution of about 0.3 mm [151]. However, B-mode imaging also provides additional spatial information along the artery. It has been suggested that, with the use of proper mathematical modelling, this additional spatial information can be used to obtain the distension waveform [150]. It has been shown that distension waveform at the carotid artery obtained using B-mode imaging with modelling has similar reproducibility as that obtained using echo-tracking [151].

In this chapter, an algorithm for obtaining the aortic distension waveform at the ascending aorta from the B-mode longitudinal images of the aortic arch is developed. In addition to the modelling of the spatial structure

of the aorta, this new algorithm also makes use of the continuity of the aortic wall motion to obtain a more accurate distension waveform. This new algorithm consists of three steps. First, an adaptive block matching scheme is used to identify the approximate locations of the edges of the aortic arch. Second, the approximate edges are refined according to the gradient of the intensity of the image. Second-degree polynomials are then fitted to the refined edges. Third, the refined edges are further fine-tuned by imposing smoothness constraints on the curvatures and vertexes over time. The distension waveform is the distance between the edges over a cardiac cycle.

To estimate the pressure waveform from the distension waveform, a relationship between the pressure and the diameter has to be assumed. Even though the arterial wall is viscoelastic and exhibits nonlinear elasticity, it has been shown that the pressure waveform and the distension waveform at the ascending aorta of human have gross similarity [57]. Therefore, a linear relationship may be assumed between the pressure and the diameter. The distension waveform may also be estimated from the pressure waveform through an exponential calibration scheme. The relationship between the pressure and the cross-sectional area of the artery can be described by an exponential function [110]. The cross-sectional area of the artery can be found from its diameter. The exponential function involves a wall rigidity coefficient, which can be found through an iterative scheme [110].

In this chapter, an aortic pressure waveform measurement method is developed. In this method, the aortic distension waveform is obtained from B-mode images of the aortic arch using the semi-automatic edge detection algorithm developed in this chapter, then the aortic pressure waveform is derived from the aortic distension waveform using an exponential calibration scheme proposed by previous researchers [110].

To investigate the clinical usefulness of the aortic pressure waveform measurement method developed in this chapter, a clinical study was performed in which this new method was applied to 9 healthy children. Aortic pressure waveforms were estimated from the aortic distension waveform through both linear and exponential calibration schemes. Carotid artery applanation tonometry was used as a reference method. Carotid artery pressure waveform was obtained using applanation tonometry and used as a surrogate of the aortic pressure waveform. The tonometric and B-mode waveforms were compared in the time domain through the root-mean-squared differences, and in the frequency domain through the moduli and phases of the harmonics. The aortic pulse pressure (PP) and two arterial stiffness indices, augmentation index (AI) and total arterial compliance (TAC), were calculated from the

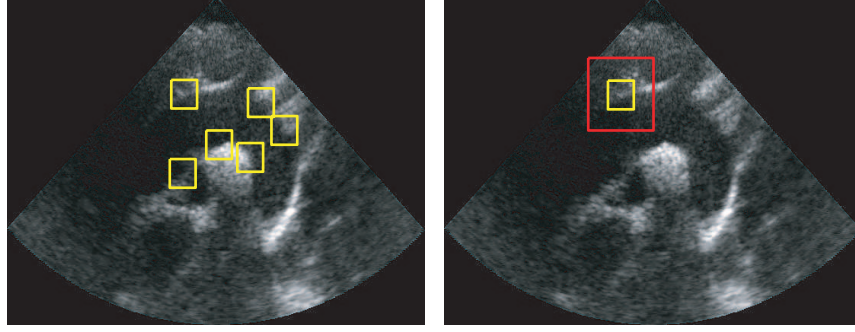


Figure 4.1: Left: several kernel blocks are selected along the edges on the first image. Right: a best-matching block is found inside the search region on the next image.

waveforms.

4.2 Methods

4.2.1 Adaptive block matching

In this semi-automatic edge detection algorithm, the aortic distension waveform is measured from a series of B-mode images of the aortic arch collected over one cardiac cycle.

On the first image, several points along the edges are selected manually (Fig. 4.1). These selected points give the approximate locations of the edges. Using block matching, these approximate locations are tracked on the subsequent images.

Kernel blocks of size $k \times k$ are defined with the selected points as the centers of the blocks. For each kernel block, a search region of size $s \times s$ is defined with the kernel block at the center (Fig. 4.1). On the subsequent images, the best-matching block to the kernel block is found within the search region. The best-matching block has the maximum correlation with the kernel block. The correlation (cr) between the kernel block and a candidate block is given by

$$cr = \frac{\sum_{x=1}^k \sum_{y=1}^k K(x, y) \times C(x, y)}{\sqrt{\sum_{x=1}^k \sum_{y=1}^k [K(x, y)]^2 \times \sum_{x=1}^k \sum_{y=1}^k [C(x, y)]^2}} \quad (4.1)$$

where K is the intensity of the kernel block and C is the intensity of the candidate block, and x and y are the spatial indices.

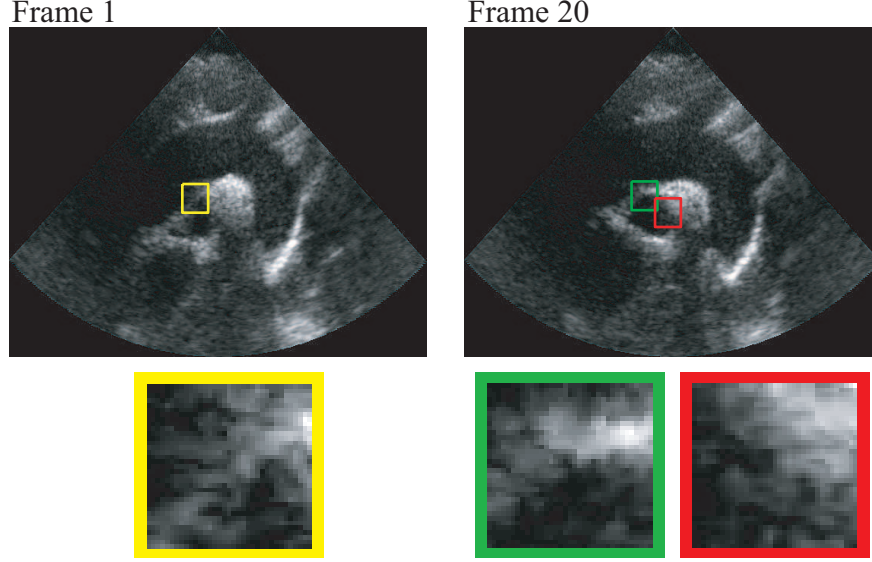


Figure 4.2: Substantial change of the curvature of the aortic wall: the part of the edge inside the original kernel block on the first image (yellow) becomes very different on the twentieth image (green); the best-matching block (red) to the original kernel block does not contain the same part of edge.

As the curvature of the aortic wall changes substantially through out the cardiac cycle, the edge contained by the kernel block becomes much different. The candidate block that has the maximum correlation with the kernel block does not necessarily contain the same edge (Fig. 4.2). To track the edge during pulsation, an adaptive scheme is used.

When the maximum correlation does not reach a certain threshold, the best-matching block of the previous image is used as the kernel block instead. Since the aortic wall motion is gradual, using the previous best-matching block as the kernel block can track the changes in the wall curvature (Fig. 4.3). However, if the previous best-matching block is used as the kernel block on all images, the information in the original kernel block may be completely lost and the best-matching block may eventually become too deviated from the original kernel block. Therefore, the previous best-matching block is used only when the maximum correlation does not reach a certain threshold γ , chosen to be 0.95.

In the experiments described in section 4.3, the image size was approximately 400 by 600 pixels. The actual size of the image was approximately

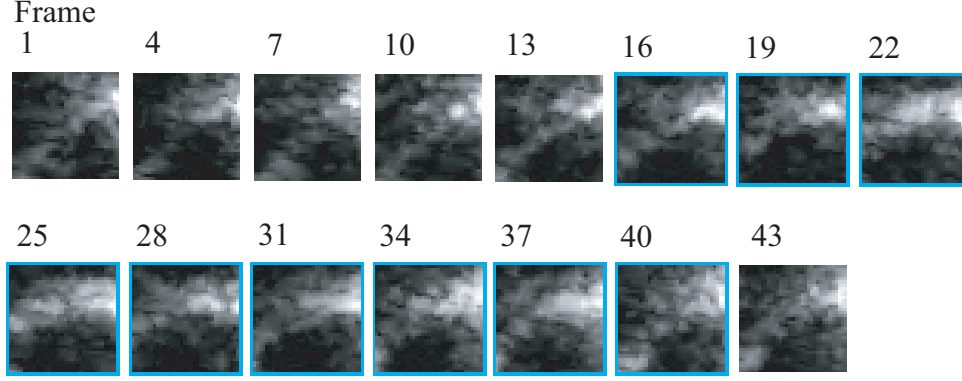


Figure 4.3: The adaptive block matching scheme: the set of best-matching blocks to the original kernel block (shown in figure 4.2) are found by the adaptive block matching scheme; the cyan highlighted blocks are found by comparing with the best-matching block on the previous image; the non-highlighted blocks are found by comparing with the original kernel block.

10 by 15 cm. k was chosen to be 4 mm (approximately 17 pixels) so that the edge contained by the kernel block had trackable movement. s was chosen to be 10 mm (approximately 43 pixels) so that the edge contained by the kernel block was always within the search region.

4.2.2 Gradient-based edge refining

A preliminary edge is defined by joining the centers of the best-matching blocks using a cubic interpolating spline [131]. The more accurate locations of the edge points are then searched for along the normal direction of the preliminary edge (Fig.4.4). The intensity function along each normal is smoothed using a cubic smoothing spline [131]. The location of the maximum gradient of the smoothed intensity function is the refined location of the edge point (Fig.4.4).

The edge refining scheme gives a set of refined edge points. For the outer edge, some of these edge points are located at the “disconnections”. These “disconnections” are due to the presence of the innominate artery, innominate vein, the left common carotid and the left subclavian arteries. These edge points do not represent the actual edge and are excluded by comparing with the preliminary edge. The discrepancy is defined as the norm between each preliminary edge point and the corresponding refined edge point. If the discrepancy is more than β , the edge point is excluded.

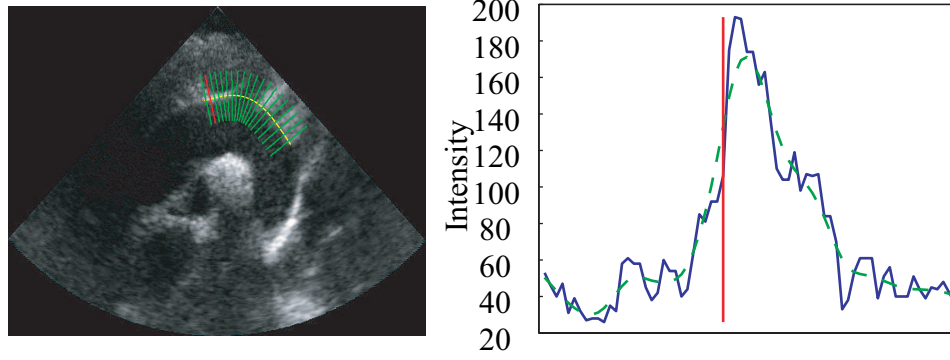


Figure 4.4: Left: the more accurate locations of the edge points are searched for along the normals of the preliminary edge. Right: a smoothing spline (green dash line) is fitted to the intensity function (blue solid line) of the normal highlighted in red on the image on the left; the vertical red line indicates the refined location of the edge.

In the experiments described in section 4.3, β was chosen to be 12 pixels for the outer edge and 8 pixels for the inner edge. Similar to the choice of k and s , β was chosen based on the resolution of the image and the normal anatomical size of the aorta and the adjacent vessels.

4.2.3 Weighted total least-squares fitting

A second degree polynomial given by:

$$y = ax^2 + bx + c \quad (4.2)$$

is fitted to the refined edge points. Since the refined edge points are found by searching along the normal direction of the preliminary edge, the error of the fit is quantified by the perpendicular distances between the points and the fit. Total least-squares fitting is used to minimize this error [163].

During total least-squares fitting, weights are assigned to the refined edge points. Two weight assigning schemes are used.

The first scheme is based on the assumption that a refined edge point is located either on the actual edge or some unrelated bright speckles. If a refined edge point is indeed located on the actual edge, it should be adjacent to a few other edge points. For each refined edge point, the weight assigned is directly proportional to the number of other refined edge points inside its surrounding region. If the number of points is less than or equal to θ , zero

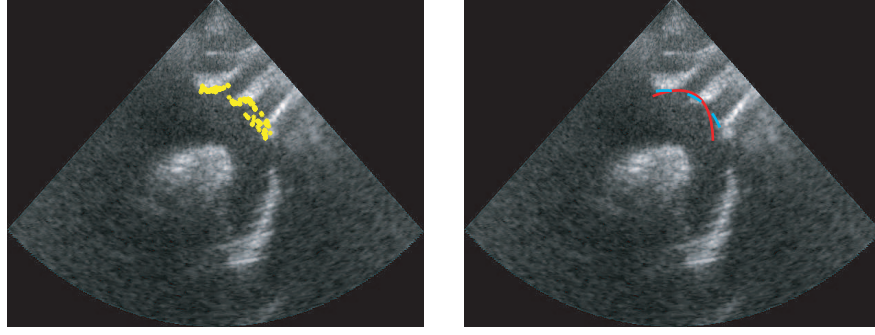


Figure 4.5: Left: some of the refined edge points are located at the edges of the left common carotid and the left subclavian arteries. Right: the total least-squares fit obtained without the second weight assigning scheme (red solid line) has a higher curvature than the total least-squares fit obtained with the second weight assigning scheme (cyan dash line).

weight is assigned. If the number of points is more than θ , the assigned weight is the number of points times 10. This weight-assigning scheme is applied to both outer and inner edges.

In the experiments described in section 4.3, θ was chosen to be 5 for the outer edge and 3 for the inner edge in this thesis. θ was chosen based on the resolution of the image and the normal anatomical size of the aorta and the adjacent vessels.

In some images, some of the refined edge points are located at the edges of the left common carotid or left subclavian arteries (Fig.4.5). These refined edge points cause the total least-squares fit to have a higher curvature. The influence of these refined edge points are reduced by assigning to them a smaller weight. The refined edge points are ordered clockwise. For each refined edge point, its distances with the next three refined edge points are calculated. Its weight is inversely proportional to the sum of these distances. When the sum of distances is over φ , a very small weight that is practically zero is assigned. This weight assigning scheme is applied only to the outer edge.

In the experiments described in section 4.3, φ was chosen to be 50. φ was chosen based on the resolution of the image and the normal anatomical size of the aorta and the adjacent vessels.

4.2.4 Continuity of the aortic wall motion

During systole, the aorta expands in order to accommodate the sudden increase in blood volume, and then slowly returns to its previous state throughout diastole. The aortic wall motion is gradual. It is therefore assumed that the changes in the curvature and the vertex of the total least-squares fit over time are smooth. The curvature (cv), the x-coordinate of the vertex (v_x) and the y-coordinate of the vertex (v_y) of a second degree polynomial are given by:

$$cv = a \quad (4.3)$$

$$v_x = \frac{-b}{2a} \quad (4.4)$$

$$v_y = \frac{-(b^2 - 4ac)}{4a} \quad (4.5)$$

The functions of cv , v_x and v_y over time are smoothed by a cubic smoothing spline [131]. The finalized edges are then obtained.

4.2.5 Choosing a cross-section along the arch

The cross-section is chosen at the ascending aorta proximal to the innominate artery, and as perpendicular to both the outer and inner edges as possible. Three cross-sections are chosen. The distension waveforms obtained along each cross-section are averaged to give the final distension waveform.

4.2.6 Estimating the pressure waveform from the distension waveform

Mean arterial pressure and diastolic pressure remain relatively constant through out the arterial tree [89]. It is thus assumed that the mean and diastolic pressures obtained at the brachial artery are the same as the mean and diastolic pressures at the aorta.

Systolic pressure (SP) and diastolic pressure (DP) are measured at the upper arm using a cuff sphygmomanometer. Mean pressure (MP) is calculated from the traditional formula [21]:

$$MP = \frac{1}{3}SP + \frac{2}{3}DP \quad (4.6)$$

Linear calibration

It is assumed that the pressure and diameter are linearly related. DP is assigned to the minimum of the distension waveform, and MP is assigned to the area integral divided by the duration of the distension waveform.

Exponential calibration

It is assumed that the pressure and the cross-sectional area of the artery are related by an exponential function [110]:

$$P(t) = P_0 \exp^{\alpha(\frac{A(t)}{A_0}-1)} \quad (4.7)$$

where $P(t)$ is the pressure function, P_0 is the reference pressure, $A(t)$ is the cross-sectional area function, A_0 is the cross-sectional area at P_0 , and α is the wall rigidity coefficient. The cross-section area is related to the diameter (D) by $A = (D/2)^2\pi$.

DP is assigned to P_0 , then the minimum of the distension waveform corresponds to A_0 .

α is found through an iterative search. With an initial guess of α , the mean aortic pressure (\bar{P}_a) can be calculated from (4.7). If the estimated \bar{P}_a is different from MP, α is recalculated as:

$$\alpha_{\text{new}} = \frac{\text{MP}}{\bar{P}_a} \alpha \quad (4.8)$$

and then \bar{P}_a is re-estimated. The iterative search stops when \bar{P}_a and MP differ by less than 0.1 mmHg.

4.3 Experiments

4.3.1 Data acquisition and processing

9 healthy children participated in this study.

B-mode images of the aortic arch were obtained from a suprasternal view using a 2.2-5.0 MHz phased-array transducer. The transmittal frequency was 2.4 MHz. The frame rate ranged from 49 to 63 frames per second.

The carotid artery pressure waveform was obtained using applanation tonometry. The ascending aortic blood velocity was obtained simultaneously using Doppler ultrasound with the transducer positioned at the suprasternal notch.

The aortic annulus was measured using two-dimensional echocardiography. Brachial artery systolic and diastolic blood pressures were measured using a cuff sphygmomanometer.

All the applanation-tonometric and echocardiographic data were acquired using a GE Vivid 7 Pro ultrasound machine (GE Vingmed, Horten, Norway) equipped with an applanation tonometer.

Aortic flow was calculated as the envelope of the Doppler spectrum of the aortic blood velocity times the lumen area. The lumen area was assumed to be circular and was calculated from the aortic annulus. The mean aortic flow was used to calculate the peripheral resistance.

4.3.2 Calibration of the carotid artery pressure waveform obtained using applanation tonometry

To calibrate the carotid artery pressure waveform obtained using applanation tonometry, DP is assigned to the minimum of the waveform and MP is assigned to the area integral divided by the duration of the waveform.

4.3.3 Comparison of waveforms

The waveforms were compared in the time domain using the root-mean-squared difference (RMSD). RMSD is given by

$$\sqrt{\frac{\sum_i (P_{\text{tono}}(i) - P_{\text{dw}}(i))^2}{n}} \quad (4.9)$$

where P_{tono} is the pressure waveform obtained using applanation tonometry, P_{dw} is the pressure waveform estimated from the distension waveform using the linear or the exponential calibration scheme, and n is the number of data points. P_{dw} was first upsampled to have the same data points as P_{tono} using a cubic interpolating spline [131].

The waveforms were also compared in the frequency domain using the moduli and the phases of the first three harmonics of the waveforms.

4.3.4 Calculations of pulse pressure, augmentation index and total arterial compliance

PP was calculated as the peak of the pressure waveform (P_{max}) minus DP.

To calculate AI and TAC, P_{dw} was first upsampled to have the same data points as P_{tono} using a cubic interpolating spline [131].

Age (yrs)	11 ± 2
Gender (M:F)	3 : 6
BSA (m^2)	1.2 ± 0.2
SP (mmHg)	108 ± 7
DP (mmHg)	64 ± 7
AO (cm)	1.65 ± 0.14

Table 4.1: Subjects' demographics: BSA is the body surface area; SP is the systolic pressure at the upper arm; DP is the diastolic pressure at the upper arm; AO is the aortic annulus.

AI was calculated as the ratio of the difference between P_{\max} and the pressure at the inflection point (P_{\inf}) to PP:

$$\text{AI} = \frac{P_{\max} - P_{\inf}}{\text{PP}} \quad (4.10)$$

If P_{\inf} occurs after P_{\max} , AI is negative [116]. In a study by Segers et al. [142], the inflection point was identified as the middle of the two zero-crossings of the second derivative of the pressure waveform. The zero-crossing of the second derivative corresponds to the local extremum of the first derivative. In this thesis, the inflection point was identified as the middle of a local minimum and a local maximum of the first derivative. This method is equivalent to the method used by Segers et al.

TAC was calculated using the area method [98]:

$$\text{TAC} = \frac{A_{12}}{R_P(P_1 - P_2)} \quad (4.11)$$

where P_1 is the pressure at the very beginning of the diastolic decay, P_2 is the end-diastolic pressure, A_{12} is the area under the pressure curve between P_1 and P_2 , and R_P is the total peripheral resistance. R_P was estimated as the mean pressure divided by the mean flow.

4.4 Results

Data are expressed as mean \pm SD. A value of $p < 0.01$ was considered as statistically significant. The demographics of the subjects are listed in Table 4.1.

P_{lin} is the aortic pressure waveform obtained from the aortic distension waveform through the linear calibration scheme. P_{exp} is the aortic pres-

sure waveform obtained from the aortic distension waveform through the exponential calibration scheme. The wall rigidity coefficient was 1.2 ± 0.5

4.4.1 Waveform comparisons

In all 9 subjects, P_{lin} and P_{exp} were compared with P_{tono} , which was used as the reference.

RMSD between P_{tono} and P_{lin} was 3.9 ± 1.5 mmHg. RMSD between P_{tono} and P_{exp} was 4.1 ± 1.5 mmHg. The difference in RMSDs obtained by the two calibration schemes was statistically insignificant. Therefore, in terms of RMSD, the two calibration schemes performed equally.

The moduli and phases of the first three harmonics of P_{tono} , P_{lin} and P_{exp} are listed in Table 4.2. For the first and second harmonics, the moduli of P_{tono} were only moderately correlated with that of P_{lin} and P_{exp} . However, in terms of the absolute pressure, the differences were quite small. The differences were also statistically insignificant. For the third harmonic, the modulus of P_{tono} was highly correlated with that of P_{lin} and P_{exp} . Again, in terms of the absolute pressure, the differences were very small. For the modulus of the third harmonic, the difference between P_{tono} and P_{exp} was statistically insignificant, but the difference between P_{tono} and P_{lin} was statistically significant. The differences in phase were statistically insignificant, except for the first harmonic between P_{tono} and P_{lin} . Overall, in terms of the differences in the frequency components, the exponential calibration scheme performed better than the linear calibration scheme.

4.4.2 Comparisons of pulse pressures, augmentation indices and total arterial compliances

PP, AI and TAC calculated from P_{tono} , P_{lin} and P_{exp} in all 9 subjects are listed in Table 4.3.

PP estimated from P_{tono} was highly correlated with that estimated from P_{lin} and P_{exp} . The differences were small and statistically insignificant.

AI estimated from P_{tono} was moderately correlated with that estimated from P_{lin} and P_{exp} . AI estimated from P_{lin} was significantly different from that estimated from P_{tono} . In contrast, the difference in AIs estimated from P_{tono} and P_{exp} was small and statistically insignificant.

TAC estimated from P_{tono} was highly correlated with that estimated from P_{lin} and P_{exp} . The differences were small and statistically insignificant. However, the difference obtained from the exponential calibration

Harmonics	P _{tono}	P _{lin}	P _{exp}	$\Delta_{\text{tono-lin}}$	$\Delta_{\text{tono-exp}}$
Modulus (mmHg)					
1st	5.6 ± 1.3	6.2 ± 1.4 $r = 0.49$	6.8 ± 1.5 $r = 0.52$	-0.6 ± 1.3 $p = \text{NS}$	-1.2 ± 1.4 $p = \text{NS}$
2nd	3.0 ± 0.7	2.5 ± 0.6 $r = 0.60$	2.8 ± 0.7 $r = 0.58$	0.5 ± 0.6 $p = \text{NS}$	0.2 ± 0.6 $p = \text{NS}$
3rd	1.7 ± 0.8	1.3 ± 0.9 $r = 0.91$	1.4 ± 1.1 $r = 0.92$	0.4 ± 0.4 $p < 0.009$	0.3 ± 0.5 $p = \text{NS}$
Phase					
1st	-1.8 ± 0.2	-2.0 ± 0.1 $r = 0.73$	-1.9 ± 0.1 $r = 0.76$	0.1 ± 0.1 $p < 0.005$	0.1 ± 0.1 $p = \text{NS}$
2nd	-2.2 ± 0.3	-2.4 ± 0.4 $r = 0.48$	-2.5 ± 0.5 $r = 0.53$	0.1 ± 0.4 $p = \text{NS}$	0.2 ± 0.4 $p = \text{NS}$
3rd	-1.6 ± 2.5	-2.1 ± 1.9 $r = 0.73$	-0.3 ± 3.0 $r = 0.56$	0.6 ± 1.7 $p = \text{NS}$	-1.3 ± 2.6 $p = \text{NS}$

Table 4.2: Comparisons of the waveforms obtained in 9 healthy children using applanation tonometry and B-mode imaging in the frequency domain: P_{tono} is the carotid artery pressure waveform obtained using applanation tonometry; P_{lin} is the aortic pressure waveform obtained using B-mode imaging with linear calibration; P_{exp} is the aortic pressure waveform obtained using B-mode imaging with exponential calibration; Δ indicates the difference; r is the correlation between P_{tono} and P_{lin}, or P_{tono} and P_{exp}.

scheme was much smaller than that obtained from the linear calibration scheme.

4.5 Discussion

The pressure-diameter relationship of the arterial wall is complicated by two aspects: nonlinear elasticity, which is often studied as static elasticity, and viscoelasticity, which is often studied as dynamic elasticity.

The nonlinear elasticity of the arterial wall is due to its complex composition. The predominant elastic materials of the arterial wall are elastin and collagen [119]. As the distending pressure inside an artery increases, the circumferential stress transfers progressively from the elastin on to the relatively inextensible collagen, and results in a nonlinear stress-strain, or increasing elastic modulus-pressure, relationship [12]. In the *in vitro* study of static elasticity of human arteries by [95], the circumferential Young's modulus of the upper thoracic aorta increased slightly and slowly up to 100 mmHg, and then it began to increase more rapidly. It implies that the pressure-diameter relationship is relatively linear up to 100 mmHg.

The elastic behavior caused by step pressure is rather different from that caused by the rapid pressure change during each heartbeat [13]. This is because of the viscoelasticity of the arterial wall. When a viscoelastic material is extended rapidly, it is stiffer than when it is extended slowly [119]. It is said to have a retarded elastic response to an applied stress as it will slowly extend to its final length. When the stress is removed, the reverse phenomenon occurs. The pressure-diameter relationship in human has been studied *in vivo* [72]. The diameter was found to have a phase lag of -6.7° to the pressure at the fundamental frequency of 1.2 Hz. This corresponds to a time delay of 0.016s. For a normal heart rate of 70 bpm, a delay of 0.016s is about 2 % of the cardiac cycle.

Combining the effects of nonlinear elasticity and viscoelasticity, the distension waveform should have similar morphology as the pressure waveform during normal pulsation. In this study, it was found that the pressure waveform and the distension waveform indeed had similar morphology as indicated by the low RMSD between P_{tono} and P_{lin} .

The morphologies of P_{lin} and P_{exp} were very similar, but the difference in amplitudes was noticeable (Fig. 4.6 and Fig. 4.7). In eight out of nine subjects, both P_{lin} and P_{exp} showed a delay during the initial rise to the systolic peak when compared to the corresponding P_{tono} (Fig. 4.6). This can be explained by the phase lag caused by the viscoelasticity of the

	P _{tono}	P _{lin}	P _{exp}
PP (mmHg)	32.6 ± 7.9	30.6 ± 6.0 $r = 0.90$	33.9 ± 7.4 $r = 0.90$
AI	-0.28 ± 0.09	-0.16 ± 0.06 $r = 0.71$	-0.21 ± 0.07 $r = 0.69$
TAC (cm ³ /mmHg)	1.29 ± 0.48	1.18 ± 0.55 $r = 0.92$	1.21 ± 0.56 $r = 0.91$
	$\Delta_{\text{tono-lin}}$	$\Delta_{\text{tono-exp}}$	
PP (mmHg)	1.9 ± 3.6 $p = \text{NS}$	-1.3 ± 3.5 $p = \text{NS}$	
AI	-0.11 ± 0.06 $p < 0.0006$	-0.07 ± 0.06 $p = \text{NS}$	
TAC (cm ³ /mmHg)	0.11 ± 0.21 $p = \text{NS}$	-0.01 ± 0.12 $p = \text{NS}$	

Table 4.3: Comparisons of pulse pressures, augmentation indices and total arterial compliances obtained in 9 healthy children using applanation tonometry and B-mode imaging: P_{tono} is the carotid artery pressure waveform obtained using applanation tonometry; P_{lin} is the aortic pressure waveform obtained using B-mode imaging with linear calibration; P_{exp} is the aortic pressure waveform obtained using B-mode imaging with exponential calibration; PP is the pulse pressure; AI is the augmentation index; TAC is the total arterial compliance; Δ indicates the difference; r is the correlation between P_{tono} and P_{lin}, or P_{tono} and P_{exp}.

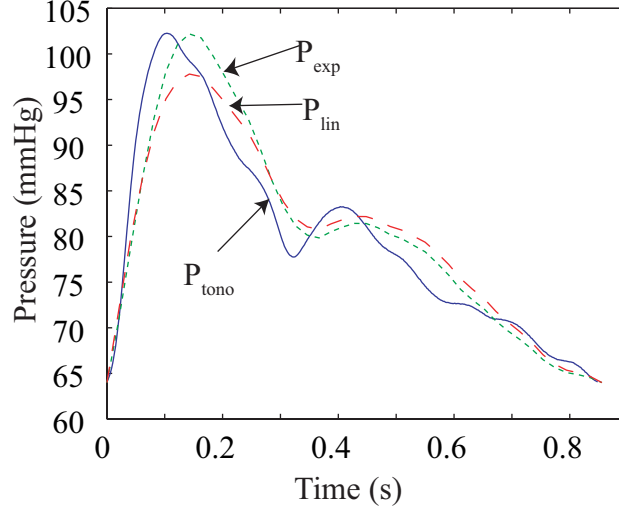


Figure 4.6: The pressure waveforms: P_{tono} is the carotid artery pressure waveform obtained using applanation tonometry; P_{lin} is the aortic pressure waveform obtained using B-mode imaging with linear calibration; P_{exp} is the aortic pressure waveform obtained using B-mode imaging with exponential calibration.

arterial wall. Both P_{lin} and P_{exp} also appeared to be “flatter” than the corresponding P_{tono} . This is particularly obvious in some subjects (Fig. 4.7). Similar observation was obtained in a study comparing the carotid artery distension waveform obtained using echo-tracking and the carotid artery pressure waveform obtained using applanation tonometry [86]. This can again be explained by the phase lag caused by the viscoelasticity and also the nonlinear elasticity. Because of the nonlinear elasticity, the diameter increases by a lesser amount at higher pressure and causes the distension waveform to be “flatter”.

The frequency components of P_{lin} and P_{exp} were only moderately correlated with that of P_{tono} . This can be explained by the delay in peak and the “flatter” shape of the distension waveform. AI estimated from P_{lin} and P_{exp} were also only moderately correlated with that estimated from P_{tono} . This is likely due to the “flatter” shape of the distension waveform. However, the difference between the AI estimated from P_{exp} and that estimated from P_{tono} was only 0.07 ± 0.06 and was statistically insignificant. It should also be noted that the inflection point is more difficult to identify for the younger subjects. This is because the reflected wave arrives at the

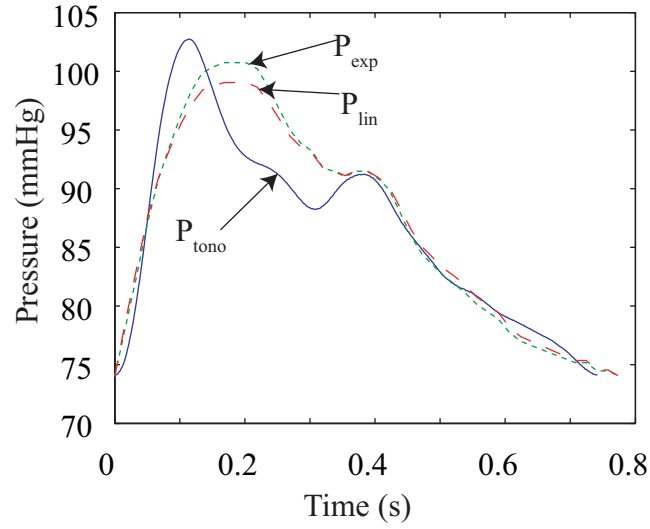


Figure 4.7: The pressure waveforms: P_{tono} is the carotid artery pressure waveform obtained using applanation tonometry; P_{lin} is the aortic pressure waveform obtained using B-mode imaging with linear calibration; P_{exp} is the aortic pressure waveform obtained using B-mode imaging with exponential calibration; the waveforms estimated from the distension waveforms are “flatter” than that obtained using applanation tonometry.

ascending aorta during late systole or early diastole, and is “buried” by the incident wave.

TAC estimated from P_{lin} and P_{exp} were highly correlated with that estimated from P_{tono} . This is because the calculation of TAC involves only the diastolic decay of the pressure waveform, and is not affected by the delay in peak and the “flatter” shape of the distension waveform.

The parameters of the semi-automatic edge detection algorithm including β , θ and φ are chosen according to the usual anatomical size of the aortic arch of the children of the particular age group in this study. For adults, a different set of parameters may be needed. The parameter γ of the adaptive block matching scheme is chosen according to the overall image quality of the B-mode images collected in this study. A future study of a large number of subjects and images is necessary to validate the choice of γ .

According to the Association for the Advancement of Medical Instrumentation (AAMI), the criterion for device performance evaluated against the commonly used cuff/stethoscope auscultation method or intra-arterial pressure allows a difference of 5 ± 8 mmHg [174]. PP estimated from P_{lin} and P_{exp} are well within this acceptability limit if PP estimated from P_{tono} is used as the reference. Therefore, PP estimated from P_{lin} and P_{exp} are potential surrogates to PP estimated from P_{tono} . However, it should be noted that the AAMI criterion is for device performance evaluated against either the commonly used cuff/stethoscope auscultation method or intra-arterial pressure, but not applanation tonometry.

Kelly and Fitchett [82] proposed a calibration scheme for the carotid artery pressure waveform obtained using applanation tonometry, and the calibrated carotid artery pressure waveform was shown to be an accurate estimate of the aortic pressure waveform. Since then, this calibration scheme has been popularly used. This calibration scheme is the same as the calibration scheme used for P_{tono} and P_{lin} in this study, except that MP is calculated as the area integral divided by the duration of the brachial artery pressure waveform. In this study, MP was calculated from the traditional formula (4.6).

As the same calibration scheme was used for P_{tono} and P_{lin} , the error in the measurement of MP (ϵ_m) does not affect the comparison between P_{tono} and P_{lin} . However, it is still of considerable interest how ϵ_m affects the estimation of PP.

Since it is assumed that the true aortic pressure waveform is linearly related to the uncalibrated tonometric waveform and the uncalibrated dis-

tension waveform, then:

$$\frac{SP_{AO} - DP}{MP - DP} = \frac{s - d}{m - d} \quad (4.12)$$

where SP_{AO} is the aortic systolic pressure, m is the area integral over the duration of the uncalibrated waveform, s and d are the maximum and minimum of the uncalibrated waveform respectively. SP_{AO} can then be calculated from MP, DP and the uncalibrated waveform using the following formula:

$$SP_{AO} = \frac{MD - DP}{m - d}(s - d) + DP \quad (4.13)$$

ϵ_m propagates towards the estimation of SP_{AO} as follow:

$$\begin{aligned} SP_{AO} + \epsilon_s &= \frac{(MP + \epsilon_m) - DP}{m - d}(s - d) + DP \\ &= SP_{AO} + \frac{\epsilon_m}{m - d}(s - d) \end{aligned} \quad (4.14)$$

$$\epsilon_s = \frac{\epsilon_m}{m - d}(s - d) \quad (4.15)$$

where ϵ_s is the error in the aortic systolic pressure. Assuming that MP is roughly the sum of one third of SP and two thirds of DP, then the term $(s-d)/(m-d)$ is about 3. MP calculated using the traditional formula and that obtained invasively at the brachial artery were compared by Bos et al. [21] and the difference was 5.0 ± 2.3 mmHg. Suppose ϵ_m is 5 mmHg then ϵ_s is approximately 15 mmHg. Such error is out of the acceptability limit. However, the calibration scheme proposed by Kelly and Fitchett [82] does not use the invasive MP as the study by Bos et al. [21]. The difference in MP calculated from the traditional formula and that from the area integral of the brachial artery pressure waveform may be smaller than 5 mmHg, if the same sphygmomanometric measurements are used in both calculations. Another non-invasive alternative is to use an automatic oscillometric device that provides direct readout of MP. MP at the brachial artery obtained using such device has been compared to the invasive MP at the aorta [148] and the difference was 0.79 mmHg. Using the oscillometric method to obtain MP may improve the accuracy of the calibration scheme.

4.6 Conclusion and future work

A method to estimate the aortic pressure waveform using B-mode imaging is developed. The carotid artery pressure waveform obtained using applanation tonometry was used as the reference method. The aortic distension

waveform showed a delay during the initial rise to the systolic peak and had a “flatter” shape when compared to the carotid artery pressure waveform. The exponential calibration scheme may be better than the linear calibration scheme since the differences in AI and TAC measured from P_{tono} and P_{exp} were smaller and insignificant (Table 4.3). The exponentially-calibrated aortic pressure waveform was similar to the tonometric carotid artery pressure waveform. PP and the TAC estimated from the exponentially-calibrated aortic pressure waveform could be used as the surrogate to that estimated from the tonometric carotid artery pressure waveform. AI estimated from the exponentially-calibrated aortic pressure waveform showed moderate accuracy.

The size of this study was small, and a large-scale study is needed to confirm the validity of the proposed method. The repeatability and reproducibility of the proposed method has to be confirmed. The subjects in this study were young, while the augmentation index is often measured in older and hypertensive subjects. It is necessary to investigate the possibility of measuring the augmentation index using the proposed method in older and hypertensive subjects.

Chapter 5

Conclusions and Future Work

5.1 Contributions

5.1.1 Model-based estimation of the aortic pulse wave velocity

In Chapter 2, a technique was developed to estimate the aortic pulse wave velocity using non-invasive data. The technique is based on a transmission line model and only requires measurements at one site. The model parameters are identified using the white-box identification and the prediction-error method.

There have been many studies of the arterial system, of human and other mammals, based on the transmission line model with variations in the types of lines, terminations and configurations [15, 24, 25, 28, 44, 78, 117]. However, few studies investigated the subjects of parameter identification. Several studies [24, 25, 28] used the prediction-error method to identify the model parameters. Although the technique presented in Chapter 2 is also based on the prediction-error method, there are several fundamental differences when compared to the techniques proposed in the previous studies.

In Chapter 2, the model is formulated in the time domain and its representation is based on the finite element method. Three parameters, unit line capacitance, load capacitance and line length, are identified using the prediction-error method. As the error function may not be convex, initial values of the parameters are calculated based on the pressure and flow data, and physiological information of the subjects. These initial values are specific to the subject and therefore should be in closer proximity of the true solution, as compared to the initial values chosen from some fixed ranges. The ratio of the line compliance to the load compliance and the pulse wave velocity are calculated from the identified parameters. This technique was tested using non-invasive data obtained from healthy children and children with Marfan syndrome. It was found that the ratio of the line compliance to

the load compliance was lower in the children with Marfan syndrome than healthy children; and the pulse wave velocity was higher in the children with Marfan syndrome than healthy children. Both observations matched the theoretical expectation.

The uniform lossless transmission model used in [25] is the same as that used in Chapter 2, but the pressure and flow waveforms are measured at the descending aorta instead. In [25], the model is formulated in the frequency domain and represented by its input impedance. Three parameters, the pulse transit time, the characteristic impedance of the line and the time constant of the load impedance are identified using the prediction-error method. It is suggested that the identification problem has infinite solution, and the smallest solution should be chosen as it is the most physiologically relevant. This technique was only tested using invasive data obtained from anesthetized dog, and has yet been applied on human.

In [24, 28], a T-tube model is used to represent the arterial system. To identify the parameters, the descending aortic flow has to be estimated.

Because of the different identifiable model parameters, the technique presented in Chapter 2 is more clinically useful.

Traditionally, pulse wave velocity is estimated using measurements obtained at two sites. As presented in Chapter 2, the two-site technique requires high accuracy of the measurement of the pulse transit time. In addition, distance measurement can be difficult in some subjects. Recently, a new technique known as Arteriograph has been proposed to measure aortic pulse wave velocity [11]. It only requires pressure measurement at the brachial artery. However, the distance measurement from the jugulum to the symphysis is still required. In addition, the theoretical basis of this technique has been challenged [159].

The aortic pulse wave velocity estimation technique presented in Chapter 2 is a one-site technique, and has been shown to be able to differentiate a group of children with Marfan syndrome from a group of healthy children. It is based on the transmission line model, which has been regarded as a suitable model for the arterial system [94]. It is also a non-invasive technique, making it potentially useful in routine clinical practice.

5.1.2 Minimally-invasive monitoring of the cardiac output

In chapter 3, a technique for continuous cardiac output monitoring using radial artery pressure was developed. The technique uses a state-space representation of a transmission line model to represent the arterial system. The model parameters are identified using a novel grey-box identifica-

tion method. The identifiability of the proposed state-space representation was investigated. The performance of the proposed grey-box identification method was tested using a Gaussian input and a simulated aortic waveform input.

The proposed state-space representation is based on the finite element method [96]. Compared to the transfer function of the transmission line model, the state-space representation has more flexibility. In the state-space representation, the model parameters, including total line compliance, total line inductance, load compliance and load resistance, are separate entries of the system matrix. In contrast, the transfer function is a lumped representation of these parameters. This feature of the state-space representation is especially useful during monitoring of the cardiac output. For example, if additional information of the compliance is available during monitoring, the model can be adjusted accordingly because the initial values of the parameters are known.

In the proposed grey-box identification, subspace identification is applied to identify an empirical model, then the physical model parameters are identified from the empirical model through iterative bilinear regressions. The proposed method is based on the framework by Xie and Ljung [175]. In Chapter 3, it was showed how this framework can be applied when the system matrices have unknown entries that are linear functions of a small number of physical parameters. The proposed method is more computational efficient than the white-box method presented in Chapter 2. In the presented white-box method, an optimization algorithm, such as the gradient-descent method and the Newton conjugate-gradient method, has to be used to identify the model parameters. In most cases, these optimization algorithms are more computationally expensive than a series of bilinear regressions.

The proposed technique was applied to 5 infants during their post-operative stay in the Intensive care unit. The accuracy of this technique was shown to be clinically acceptable during a 5 hours re-calibration-free period.

As presented in Section 1.3.3, PulseCO and PiCCO are the current methods that monitor the cardiac output using the radial artery pressure waveform. Both of these techniques require invasive calibration using thermodilution or transpulmonary thermodilution. In contrast, for the proposed technique, calibration is performed non-invasively using transthoracic Doppler ultrasound.

Recently, techniques based on multichannel blind system identification have been proposed to monitor cardiac output using multiple peripheral

pressure waveforms [107,155]. Compared to PulseCO and PiCCO, these techniques are based on more sophisticated identification method. However, calibration is still required by these techniques, and an additional peripheral pressure measurement is also needed. Up until now, these techniques are yet to be proved to be superior to PulseCO and PiCCO for cardiac output monitoring in human.

5.1.3 Estimation of the aortic pressure waveform using B-mode imaging

In Chapter 4, a method to measure aortic pressure waveform using B-mode imaging was presented. Recently, the idea of estimating the carotid artery pressure waveform from the carotid artery distension waveform has been explored by several studies [86,161,166]. In these studies, echo-tracking was used to measure the carotid artery distension waveform. Given the high spatial resolution that can be achieved by echo-tracking, the carotid artery distension waveform can be measured reliably. In contrast, the reproducibility and repeatability of the edge detection algorithm presented in chapter 4 has yet to be investigated.

The method presented in chapter 4 may have an advantage over the echo-tracking method as it measures the aortic pressure waveform using the distension waveform obtained at the aorta. The carotid artery pressure waveform may not be a suitable surrogate as the aortic pressure waveform in the case of carotid stenosis. The echo-tracking method has yet to be used to measure the aortic pressure waveform.

5.1.4 Suggestions for future work

It has been shown that the model-based pulse wave velocity estimation method proposed in this thesis can differentiate a group of children with Marfan syndrome from a group of normal children. However, since the true aortic stiffness is not known, the accuracy of this method is yet to be confirmed. The true aortic stiffness can be obtained by measuring the change in the aortic diameter and the corresponding change in the pressure at the same location invasively. A follow-up animal study in which the true aortic stiffness is altered and the correlation between the true aortic stiffness and the model-based pulse wave velocity is found may confirm the accuracy of the proposed method.

For the cardiac output monitoring study, a major limitation is that the number of patients participated is small. Studies with a much larger sam-

ple size are required to further validate this technique. In addition, it is useful to determine for how long this technique can maintain an acceptable accuracy without re-calibration. Further studies to acquire multiple CO determinations at different time points in a longer time intervals from each patient would be valuable. This technique should also be validated on different patient populations and under different conditions (e.g. hemodynamic instability).

Using the proposed grey-box identification method, the patient-specific transmission line model is identified and the aortic flow can be estimated from the radial artery pressure. Aortic pressure may also be estimated from the identified model and the radial artery pressure. A non-invasive method to measure the aortic pressure waveform is desirable, and the generalized transfer function method has been used to estimate the aortic pressure from the radial pressure. The possibility of using the patient-specific transmission line model instead of the generalized transfer function should be investigated.

The method for aortic pressure waveform measurement presented in this thesis is strongly dependent on the accuracy of the method for the aortic distension waveform measurement. The reproducibility, the repeatability, the inter- and intra- observer errors of the method for the aortic distension waveform measurement should be further investigated.

References

1. E. Agabiti-Rosei, G. Mancia, M. F. O'Rourke, M. J. Roman, M. E. Safar, H. Smulyan, J.-G. Wang, I. B. Wilkinson, B. Williams and C. Vlachopoulos, "Central blood pressure measurements and antihypertensive therapy: a consensus document," *Hypertension*, vol. 50, pp.154-160, 2007.
2. E. L. Alderman, A. Branzi, W. Sanders and B. W. Brown, "Evaluation of the pulse-contour method of determining stroke volume in man," *Circulation*, vol. 46, pp. 546-558, 1972.
3. R. Armentano, J. L. Megnien, A. Simon, F. Bellenfant, J. Barra and J. Levenson, "Effects of hypertension on viscoelasticity of carotid and femoral arteries in humans," *Hypertension*, vol. 26, pp. 48-54, 1995.
4. R. G. Asmar, P. C. Brunel, B. M. Pannier, P. J. Lacolley and M. E. Safar, "Arterial distensibility and ambulatory blood pressure monitoring in essential hypertension," *Am J Cardiol*, vol. 61, pp. 1066-1070, 1988.
5. R. Asmar, A. Benetos, G. London, C. Hugue, Y. Weiss, J. Topouchian, B. Laloux and M. Safar, "Aortic distensibility in normotensive, untreated and treated hypertensive patients," *Blood Press*, vol. 4, pp. 48-54, 1995.
6. R. Asmar, A. Benetos, J. Topouchian, P. Laurent, B. Pannier, A.-M. Brisac, R. Target and B. I. Levy, "Assessment of arterial distensibility by automatic pulse wave velocity measurement: validation and clinical application studies," *Hypertension*, vol. 26, pp. 485-490, 1995.
7. R. G. Asmar, G. M. London, M. E. O'Rourke and M. E. Safar, "Improvement in blood pressure, arterial stiffness and wave reflections with a very-low-dose Perindopril/Indapamide combination in hypertensive patient," *Hypertension*, vol. 38, pp. 922-926, 2001.

8. A. P. Avolio, S.-G. Chen, R.-P. Wang, C.-L. Zhang, M.-F. Li and M. F. O'Rourke, "Effects of aging on changing arterial compliance and left ventricular load in a northern Chinese urban community," *Circulation*, vol. 68, pp. 50-58, 1983.
9. A. P. Avolio, F.-Q. Deng, W.-Q. Li, Y.-F. Luo, Z.-D. Huang, L.-F. Xing and M. F. O'Rourke, "Effects of aging on arterial distensibility in populations with high and low prevalence of hypertension: comparison between urban and rural communities in China," *Circulation*, vol. 71, pp. 202-210, 1985.
10. J.-P. Baguet, S. Douchin, H. Pierre, A.-M. Rossignol, M. Bost and J.-M. Mallion, "Structural and functional abnormalities of large arteries in the Turner syndrome," *Heart*, vol. 91, pp. 1442-1446, 2005.
11. J. Baulmann, U. Schillings, S. Rickert, S. Uen, R. Düsing, M. Illyes, A. Cziraki, G. Nickenig and T. Mengden, "A new oscillometric method for assessment of arterial stiffness: comparison with tonometric and piezo-electronic methods," *J Hypertens*, vol. 26, pp. 523-528, 2008.
12. D. H. Bergel, "The static elastic properties of the arterial wall," *J Physiol*, vol. 156, pp. 445-457, 1961.
13. D. H. Bergel, "The dynamic elastic properties of the arterial wall," *J Physiol*, vol. 156, pp. 458-469, 1961.
14. D. S. Berger, J. K. Li, W. K. Laskey and A. Noordergraaf, "Repeated reflection of waves in the systemic arterial system," *Am J Physiol*, vol. 264, pp. 269-291, 1993.
15. D. S. Berger, J. K. Li and A. Noordergraaf, "Differential effects of wave reflections and peripheral resistance on aortic blood pressure: a model-based study," *Am J Physiol*, vol. 266, pp. 1626-1642, 1994.
16. G. Biancofiore, L. A. H. Critchley, A. Lee, L. Bindi, M. Bisà, M. Esposito, L. Meacci, R. Mozzo, P. DeSimone, L. Urbani and F. Filipponi, "Evaluation of an uncalibrated arterial pulse contour cardiac output monitoring system in cirrhotic patients undergoing liver surgery," *Br J Anaesth*, vol. 102, pp. 47-54, 2009.
17. J. Blacher, R. Asmar, S. Djane, G. M. London and M. E. Safar, "Aortic pulse wave velocity as a marker of cardiovascular risk in hypertensive patients," *Hypertension*, vol. 33, pp. 1111-1117, 1999.

18. R. D. Bland, W. C. Shoemaker, E. Abraham, J. C. Cobo, "Hemodynamic and oxygen transport patterns in surviving and nonsurviving postoperative patients," *Crit Care Med*, vol.13, pp. 85-90, 1985.
19. P. Boutouyrie, A. I. Tropeano, R. Asmar, I. Gautier, A. Benetos, P. Lacolley, S. Laurent, "Aortic stiffness is an independent predictor of primary coronary events in hypertensive patients: a longitudinal study," *Hypertension*, vol. 39, pp. 10-15, 2002.
20. M. Boyle, L. Steel, G. M. Flynn, M. Murgo, L. Nicholson, M. O'Brien and D. Bihari, "Assessment of the clinical utility of an ultrasonic monitor of cardiac output (the USCOM) and agreement with thermodilution measurement," *Crit Care Resusc*, vol. 11, pp. 198-203, 2009.
21. W. Bos, E. Verrij, H. Vincent, B. Westerhof, G. Parati and G. van Montfrans G, "How to assess mean blood pressure properly at the brachial artery level," *J Hypertens*, vol. 25, pp. 751-755, 2007.
22. T. J. Bradley, J. E. Potts, M. T. Potts, A. M. DeSouza and G. G. S. Sandor, "Echocardiographic Doppler assessment of the biophysical properties of the aorta in pediatric patients with the Marfan syndrome," *Am J Cardiol*, vol. 96, pp. 1317-1321, 2005.
23. J. C. Bramwell and A. V. Hill, "Velocity of transmission of the pulse-wave," *Lancet*, vol. 199, pp. 891-892, 1922.
24. Burattini, R., and K. B. Campbell. Modified asymmetric T-tube model to infer arterial wave reflection at the aortic root. *IEEE Trans Biomed Engg*, vol. 36, pp. 805-814, 1989.
25. R. Burattini K. B. Campbell, "Physiological relevance of uniform elastic tube-models to infer descending aortic wave reflection: a problem of identifiability," *Ann Biomed Eng*, vol. 28, pp. 512-523, 2000.
26. R. Burattini and P. O. Di Salvia, "Development of systemic arterial mechanical properties from infancy to adulthood interpreted by four-element windkessel models," *J Appl Physiol*, vol. 103, pp.66-79, 2007.
27. K. B. Campbell, L. C. Lee, H. F. Frasch and A. Noordergraaf, "Pulse reflection sites and effective length of the arterial system," *Am J Physiol*, vol. 256, pp. 1684-1689, 1989.

28. K. B. Campbell, R. Burattini, D. L. Bell, R. D. Kirkpatrick and G. G. Knowlen, "Time-domain formulation of asymmetric T-tube model of arterial system," *Am J Physiol*, vol. 258, pp. 1761-1774, 1990.
29. M. Cecconi, J. Fawcett, R. M. Grounds and A. Rhodes, "A prospective study to evaluate the accuracy of pulse power analysis to monitor cardiac output in critically ill patients," *BMC Anesth*, vol. 8, 2008.
30. J. S Chan, D. Segara and Priya Nair, "Measurement of cardiac output with a non-invasive continuous wave Doppler device versus the pulmonary artery catheter: a comparative study," *Crit Care Resusc*, vol. 8, pp. 309-314, 2006.
31. R. Chand, Y. Mehta and N. Trehan, "Cardiac output estimation with a new Doppler device after off-pump coronary artery bypass surgery," *J Cardiothorac Vasc Anesth*, vol. 20, pp. 315-319, 2006.
32. C.-H. Chen, E. Nevo, B. Fetis, P. H. Pak, F. C. P. Yin, L. Maughan and D. A. Kass, "Estimation of central aortic pressure waveform by mathematical transformation of radial tonometry pressure," *Circulation*, vol. 95, pp. 1827-1836, 1997.
33. G. C. Cloud, C. Rajkumar, J. Kooner, J. Cooke and C. J. Bulpitt, "Estimation of central aortic pressure by SphygmoCor requires intra-arterial peripheral pressures," *Clin Sci*, vol. 105, pp. 219-225, 2003.
34. A. F. Connors Jr, T. Speroff, N. V. Dawson, C. Thomas, F. E. Harrell Jr, D. Wagner, N. Desbiens, L. Goldman, A. W. Wu, R. M. Califf, W. J. Fulkerson Jr, H. Vidaillet, S. Broste, P. Bellamy, J. Lynn and W. A. Knaus, "The effectiveness of right heart catheterization in the initial care of critically ill patients," *JAMA*, vol. 276, pp. 889-897, 1996.
35. A. Corley, A. G. Barnett, D. Mullany and J. F. Fraser, "Nurse-determined assessment of cardiac output. Comparing a non-invasive cardiac output device and pulmonary artery catheter: a prospective observational study," *Int J Nurs Stud*, vol. 46, pp. 1291-1297, 2009.
36. L. A. H. Critchley and J. A. J. H. Critchley, "A meta-analysis of studies using bias and precision statistics to compare cardiac output estimation techniques," *J Clin Monit*, vol. 15, pp. 85-91, 1999.

37. J. I. Davies, M. M. Band, S. Pringle, S. Ogston and A. D. Struthers, "Peripheral blood pressure measurement is as good as applanation tonometry at predicting ascending aortic blood pressure," *J Hypertens*, vol. 21, pp. 571-576, 2003.
38. J. De Backer, B. Loeys and A. De Paepe, "Marfan and Marfan-like syndromes," *Artery Res*, vol. 3, pp. 9-16, 2009.
39. K. De Cock and B. De Moor, "Subspace identification methods," *Control systems, robotics and automation, EOLSS, UNESCO encyclopedia of life support systems*, vol. 1, pp. 933-979, 2003.
40. R. H. Dietzman, R. A. Ersek, C. W. Lillehei, A. R. Castaneda and R. C. Lillehei, "Low output syndrome: recognition and treatment," *J Thorac Cardiovasc Surg*, vol. 57, pp. 138-150, 1969.
41. J. A. Dineley, N. McDicken and P. R. Hoskins, "Factors affecting the arterial distension waveform derived from tissue doppler imaging (TDI): an in vitro study on precision," *Ultrasound Med Biol*, vol.33, pp. 1123-1131, 2007.
42. H. G. M. Dötsch and P. M. J. Van den Hof, "Test for local structure identifiability of high-order non-linearly parameterized state space models," *Automatica*, vol. 32, pp. 873-883, 1996.
43. G. M. Drzewiecki, J. Melbin and A. Noordergraaf, "Arterial tonometry: review and analysis," *J Biomechanics*, vol. 16, pp. 141-152, 1983.
44. Einav, S., S. Aharoni, and M. Manoach. Exponentially tapered transmission line model of the arterial system. *IEEE Trans. Biomed. Eng.* 35:333-339, 1988.
45. D. J. Eveson, T. G. Robinson, N. S. Shan, R. B. Panerai, S. K. Paul and J. F. Potter, "Abnormalities in cardiac baroreceptor sensitivity in acute ischaemic stroke patients are related to aortic stiffness," *Clin Sci*, vol. 108, pp. 441-447, 2005.
46. B. Fetics, E. Nevo, C.-H. Chen and D. A. Kass, "Parameteric model derivation of transfer function for noninvasive estimation of aortic pressure by radial tonometry," *IEEE Trans Biomed Eng*, vol. 46, pp. 698-706, 1999.

47. U. Fakler, Ch. Pauli, G. Balling, H. P. Lorenz, A. Eicken, M. Hennig, and J. Hess, "Cardiac index monitoring by pulse contour analysis and thermodilution after pediatric cardiac surgery," *J Thorac Cardiovasc Surg*, vol.133, pp. 224–228, 2007.
48. T. W. Felbinger, D. A. Reuter, H. K. Eltzschig, K. Moerstedt, O. Goedje and A. E. Goetz, "Comparison of pulmonary arterial thermodilution and arterial pulse Contour analysis: evaluation of a new algorithm," *J Clin Anesth*, vol. 14, pp. 296-301, 2002.
49. T. W. Felbinger, D. A. Reuter, H. K. Eltzschig, J. Bayerlein and A. E. Goetz, "Cardiac index measurements during rapid preload changes: a comparison of pulmonary artery thermodilution with arterial pulse contour analysis," *J Clin Anesth*, vol. 17, pp. 241-248, 2005.
50. E. A. Fisher, J. A. Stahl, J. H. Budd, M. E. Goldman, "Transesophageal echocardiography: procedures and clinical application," *JACC*, vol. 18, pp. 1333-1348, 1991.
51. J. A. Franciosa, "Evaluation of the CO₂ rebreathing cardiac output method in seriously ill patients," *Circulation*, vol. 55, pp. 449-455, 1977.
52. D. N. Ghista, G. Jayaraman and H. Sandler, "Analysis for the non-invasive determination of arterial properties and for the transcutaneous continuous monitoring of arterial blood pressure," *Med Biol Eng Comput*, vol. 16, pp. 715-726, 1979.
53. O. Gödje, C. Thiel, P. Lamm, H. Reichenspurner, C. Schmitz, A. Schütz and B. Reichart, "Less invasive, continuous hemodynamic monitoring during minimally invasive coronary surgery," *Ann Thorac Surg*, vol. 68, pp. 1532-1536, 1999.
54. O. Gödje, K. Höke, A. E. Goetz, T. W. Felbinger, D. A. Reuter, B. Reichart, R. Friedl, A. Hannekum, and U. J. Pfeiffer, "Reliability of a new algorithm for continuous cardiac output determination by pulse-contour analysis during hemodynamic instability," *Crit Care Med*, vol. 30, pp. 52–59, 2002.
55. S. Golemati, A. Sassano, M. J. Lever, A. A. Bharath, S. Dhanjiu and A. N. Nicolaides, "Carotid artery wall motion estimated from B-mode ultrasound using region tracking and block matching," *Ultrasound Med Biol*, vol. 29, pp. 387-399, 2003.

56. S. Graf, J. Gariépy, M. Massonneau, R. L. Armentano, S. Mansour, J. G. Barra, A. Simon and J. Levenson, "Experimental and clinical validation of arterial diameter waveform and intimal media thickness obtained from B-mode ultrasound image processing," *Ultrasound Med Biol*, vol. 25, pp. 1353-1363, 1999.
57. J. C. Greenfield and D. J. Patel, "Relation between pressure and diameter in the ascending aorta of man," *Circ Res*, vol. 10, pp. 778-781, 1962.
58. M. Groenink, A. de Roos, B. J. M. Mulder, J. A. E. Spaan and E. E. van der Wall, "Changes in aortic distensibility and pulse wave velocity assessed with magnetic resonance imaging following beta-blocker therapy in the Marfan syndrome," *Am J Cardiol*, vol. 82, pp. 203-208, 1998.
59. M. Groenink, A. De Roos, B. J. M. Mulder, B. Verbeeten Jr., J. Timmermans, A. H. Zwinderman, J. A. E. Spaan and E. E. van der Wall, "Biophysical properties of the normal-sized aorta in patients with Marfan Syndrome: evaluation with MR flow mapping," *Radiology*, vol. 219, pp. 535-540, 2001.
60. J.-O. Hahn, A. T. Reisner, and H. H. Asada, "Blind identification of two-channel IIR systems with application to central cardiovascular monitoring," *J-DSMC*, vol. 131, 2009.
61. B. A. Haluska, L. Jeffriess, P. M. Mottram, S. G. Carlier and T. H. Marwick, "A new technique for assessing arterial pressure wave forms and central pressure with tissue Doppler," *Cardiovasc Ultrasound*, vol. 5, pp. 6, 2007.
62. W. F. Hamilton and J. W. Remington, "The measurement of the stroke volume from the pressure pulse," *Am J Physiol*, vol. 148, pp. 14-24, 1947.
63. T. T. Hamilton, L. M. Huber, and M. E. Jessen, "PulseCO: A less-invasive method to monitor cardiac output from arterial pressure after cardiac surgery," *Ann Thorac Surg*, vol. 74, pp. 1408-1412, 2002.
64. O. Hamzaoui, X. Monnet, C. Richard, D. Osman, D. Chemla, and J.-L. Teboul, "Effects of changes in vascular tone on the agreement between

- pulse contour and transpulmonary thermodilution cardiac output measurements within an up to 6-hour calibration-free period,” *Crit Care Med*, vol. 36, pp. 434–440, 2008.
65. C. S. Hayward, D. C. Knight, B. G. Wren and R. P. Kelly, “Effect of hormone replacement therapy on non-invasive cardiovascular haemodynamics,” *J Hypertens*, vol. 15, pp. 987–993, 1997.
66. A. P. G. Hoeks, P. J. Brands, F. A. M. Smeets and R. S. Reneman, “Assessment of the distensibility of superficial arteries,” *Ultrasound Med Biol* vol. 16, pp. 121–128, 1990.
67. C. K. Hofer, M. Cecconi, G. Marx, and G. della Rocca, “Minimally invasive haemodynamic monitoring,” *Eur. J. Anaesthesiol*, vol. 26, pp. 996–1002, 2009.
68. S.A. Hope, D. B. Tay, I. T. Meredith and J. D. Cameron, “Use of arterial transfer functions for the derivation of aortic waveform characteristics,” *J Hypertens*, vol. 21, pp. 1299–1305, 2003.
69. S. A. Hope, I. T. Meredith, D. Tay and J. D. Cameron, “ ‘Generalizability’ of a radial-aortic transfer function for the derivation of central aortic waveform parameters,” *J Hypertens*, vol. 25, pp. 1812–1820, 2007.
70. S. A. Hope, I. T. Meredith and J. D. Cameron, “Arterial transfer functions and the reconstruction of central aortic waveforms: myths, controversies and misconceptions,” *J Hypertens*, vol. 26, pp. 4–7, 2008.
71. I. G. Horváth, A. Németh, Z. Lenkey, N. Alessandri, F. Tufano, P. Kis, B. Gaszner and A. Cziráki, “Invasive validation of a new oscillometric device (Arteriograph) for measuring augmentation index, central blood pressure and aortic pulse wave velocity,” *J Hypertens*, vol. 28, 2010.
72. T. Imura, K. Yamamoto, T. Satoh, K. Kanamori, T. Mikami and H. Yasuda, “In vivo viscoelastic behavior in the human aorta,” *Circ Res*, vol. 66, pp. 1413–1419, 1990.
73. R. N. Isnard, B. M. Pannier, S. Laurent, G. M. London, B. Diebold and M. E. Safar, “Pulsatile diameter and elastic modulus of the aortic arch in essential hypertension: a noninvasive study,” *JACC*, vol. 13, pp. 399–405, 1989.

74. J. R. C. Jansen, K. H. Wesseling, J. J. Settels and J. J. Schreuder, "Continuous cardiac output monitoring by pulse contour during cardiac surgery," *Eur Heart J*, vol. 11(Suppl. 1), pp. 26-32, 1990.
75. N. A. Jatoi, A. Mahmud, K. Bennett and J. Feely, "Assessment of arterial stiffness in hypertension: comparison of oscillometric (Arteriograph), piezoelectronic (Complior) and tonometric (SphygmoCor) techniques," *J Hypertens*, vol. 27, pp. 2186-2191, 2009.
76. G. Jondeau, P. Boutouyrie, P. Lacolley, B. Laloux, O. Dubourg, J. Bourdarias and S. Laurent, "Central pulse pressure is a major determinant of ascending aorta dilation in Marfan syndrome," *Circulation*, vol. 99, pp. 2677-2681, 1999.
77. M. Karamanoglu, M. F. O'Rourke, A. P. Avolio and R. P. Kelly, "An analysis of the relationship between aortic and peripheral upper limb pressure waves in man," *Eur Heart J*, vol. 14, pp. 160-167, 1993.
78. M. Karamanoglu, D. E. Gallagher, A. P. Avolio and M. F. O'Rourke, "Functional origin of reflected pressure waves in a multibranched model of the human arterial system," *Am J Physiol*, vol. 267, pp. 1681-1688, 1994.
79. M. Karamanoglu, D. E. Gallagher, A. P. Avolio and M. F. O'Rourke, "Pressure wave propagation in a multibranched model of the human of the human upper limb," *Am J Physiol*, vol. 269, pp. 1363-1369, 1995.
80. R. Kelly, C. Hayward, J. Ganis, J. Daley, A. Avolio and M. O'Rourke, "Noninvasive registration of the arterial pressure pulse waveform using high-fidelity applanation tonometry," *J Vasc Med Biol*, vol. 1, pp. 142-149, 1989.
81. R. Kelly, M. Karamanoglu, A. Avolio and M. O'Rourke, "Noninvasive carotid pressure wave registration as an indicator of ascending aortic pressure," *J Vasc Med Biol*, vol. 1, pp. 241-241, 1989.
82. R. Kelly and D. Fitchett, "Noninvasive determination of aortic input impedance and external left ventricular power output: a validation and repeatability study of a new technique," *J Am Coll Cardiol*, vol. 20, pp. 952-963, 1992.

83. R. P. Kelly, S. C. Millasseau, J. M. Ritter and P. J. Chowienczyk, "Vasoactive drugs influence aortic augmentation index independently of pulse-wave velocity in healthy men," *Hypertension*, vol. 37, pp. 1429-1433, 2001.
84. J. J. Kim, W. J. Dreyer, A. C. Chang, J. P. Breinholt III, and R. G. Grifka, "Arterial pulse wave analysis: An accurate means of determining cardiac output in children," *Pediatr Crit Care Med*, vol. 7, pp. 532-535, 2006.
85. T. Kind, T. J. C. Faes, J.-W. Lankhaar, A. Vonk-Noordegraaf, and M. Verhaegen, "Estimation of three- and four- element Windkessel parameters using subspace model identification," *IEEE Trans Biomed Eng*, vol. 57, pp. 1531-1538, 2010
86. J. Kips, F. Vanmolkot, D. Mahieu, S. Vermeersch, I. Fabry, J. de Hoon, L. Van Bortel and P. Segers, "The use of diameter distension waveforms as an alternative for tonometric pressure to assess carotid blood pressure," *Physiol Meas*, vol. 31, pp 543-553, 2010.
87. W. Knirsch, O. Kretschmar, M. Tomaske, K. Stutz, N. Nagdyman, C. Balmer, A. Schmitz, D. Béttex, F. Berger, U. Bauersfeld and M. Weiss, "Cardiac output measurement in children: comparison of the ultrasound cardiac output monitor with thermodilution cardiac output measurement," *Intensive Care Med*, vol. 34, pp. 1060-1064, 2008.
88. M. J. F. Kool, T. van Merode, R. s. Reneman, A. P. G. Hoeks, H. A. J. Struyker Boudier and L. M. A. B. Van Bortel, "Evaluation of reproducibility of a vessel wall movement detector system for assessment of large artery properties," *Cardiovasc Res*, vol. 28, pp. 610-614, 1994.
89. E. J. Kroeker and E. H. Wood, "Comparison of simultaneously recorded central and peripheral arterial pressure pulses during rest, exercise and tilted position in man," *Circ Res*, vol. 3, pp. 623-632, 1955.
90. P. Lacolley, S. Gautier, O. Poirier, B. Pannier, F. Cambien and A. Benetos, "Nitric oxide synthase gene polymorphisms, blood pressure and aortic stiffness in normotensive and hypertensive subjects," *J Hypertens*, vol. 16, pp. 31-35, 1998.
91. G. J. Langewouters, K. H. Wesseling and W. J. Goedhard, "The static elastic properties of 45 human thoracic and 20 abdominal aortas in

- vitro and the parameters of a new model,” *J Biomech*, vol. 17, pp. 423-435, 1984.
92. S. Laurent, P. Boutouyrie, R. Asmar, I. Gautier, B. Laloux, L. Guize, P. Ducimetiere and A. Benetos, “Aortic stiffness is an independent predictor of all-cause and cardiovascular mortality in hypertensive patients,” *Hypertension*, vol. 37, pp. 1236-1241, 2001.
93. S. Laurent, S. Katsahian, C. Fassot, A.-I. Tropeano, I. Gautier, B. Laloux and P. Boutouyrie, “Aortic stiffness is an independent predictor of fatal stroke in essential hypertension,” *Stroke*, vol. 34, pp. 1203-1206, 2003.
94. S. Laurent, J. Cockcroft, L. Van Bortel, P. Boutouyrie, C. Giannattasio, D. Hayoz, B. Pannier, C. Vlachopoulos, I. Wilkinson and H. Struijker-Boudier, “Expert consensus document on arterial stiffness: methodological issues and clinical applications,” *Eur Heart J*, vol. 27, pp. 2588-2605, 2007.
95. B. M. Learoyd and M. G. Taylor, “Alterations with age in the viscoelastic properties of human arterial walls,” *Circ Res*, vol. 18, pp. 278-292, 1966.
96. S. Y. Lee, A. Konrad, and R. Saldanha, “Lossy transmission line transient analysis by the finite element method,” *IEEE Trans Magn*, vol. 29, pp. 1730-1732, 1993.
97. N. W. F. Linton and R. A. F. Linton, “Estimation of changes in cardiac output from the arterial blood pressure waveform in the upper limb,” *Br J Anaesth*, vol. 86, pp. 486-496, 2001.
98. Z. Liu, K. P. Brin and F. C. P. Yin, “Estimation of total arterial compliance: an improved method and evaluation of current methods,” *Am J Physiol*, vol. 251, pp. 588-600, 1986.
99. L. Ljung, *System Identification: Theory for the User*. Upper Saddle River, NJ: Prentice-Hall, 1999.
100. G. M. London, S. J. Marchais, M. E. Safar, A. F. Genest, A. P. Guerin, F. Metivier, K. Chedid and A. M. London, “Aortic and large artery compliance in end-stage renal failure,” *Kidney Int*, vol. 37, pp. 137-142, 1990.

-
101. G. M. London, A. P. Guerin, S. J. Marchais, B. Pannier, M. E. Safar, M. Day and F. Metivier, "Cardiac and arterial interactions in end-stage renal disease," *Kidney Int*, vol. 50, pp. 600-608, 1996.
 102. C. Lyzell, M. Enqvist and L. Ljung, "Handling certain structure information in subspace identification," in *15th IFAC Symposium on System Identification*, Saint-Malo, France, 2009, pp. 90-95.
 103. S. Madhavan, W. L. Ooi, H. Cohen and M. H. Alderman, "Relation of pulse pressure and blood pressure reduction to the incidence of myocardial infarction," *Hypertension*, vol. 23, pp. 395-401, 1994.
 104. A. Mahmud and J. Feely, "Acute effect of caffeine on arterial stiffness and aortic pressure waveform," *Hypertension*, vol. 38, pp. 227-231, 2001.
 105. G. R. Manecke and W. R. Auger, "Cardiac output determination from the arterial pressure wave: clinical testing of a novel algorithm that does not require calibration," *J Cardiothorac Vasc Anesth*, vol. 21, pp. 3-7, 2007.
 106. J. Mayer, J. Boldt, M. W. Wolf, J. Lang and S. Suttner, "Cardiac output derived from arterial pressure waveform analysis in patients undergoing cardiac surgery: validity of a second generation device," *Anesth Analg*, vol. 106, pp. 867-872, 2008.
 107. D. B. McCombie, A. T. Reisner, and H. H. Asada, "Laguerre-model blind system identification: cardiovascular dynamics estimated from multiple peripheral circulatory signals," *IEEE Trans Biomed Eng*, vol. 52, pp. 1889-1901, 2005.
 108. J. V. McCoy, S. M. Hollenberg, R. P. Dellinger, R. C. Arnold, L. Russo, V. Lotano, P. Peters, J. E. Parrillo and S. Trzeciak, "Continuous cardiac index monitoring: a prospective observational study of agreement between a pulmonary artery catheter and a calibrated minimally invasive technique," *Resuscitation*, vol. 80, pp. 893-897, 2009.
 109. S. Meaume, A. Benetos, O. F. Henry, A. Rudnichi and M. E. Safar, "Aortic pulse wave velocity predicts cardiovascular mortality in subjects >70 years of age," *Arterioscler Thromb Vasc Biol*, vol. 21, pp. 2046-2050, 2001.

110. J. M. Meinders and A. P. G. Hoeks, "Simultaneous assessment of diameter and pressure waveforms in the carotid artery," *Ultrasound Med Biol*, vol. 30, pp. 147-154, 2004.
111. S. C. Millasseau, R. P. Kelly, J. M. Ritter and P. J. Chowienczyk, "Determination of age-related increases in large artery stiffness by digital pulse contour analysis," *Clin Sci*, vol. 103, pp. 371-377, 2002.
112. S. C. Millasseau, A. D. Stewart, S. J. Patel, S. R. Redwood and P. J. Chowienczyk, "Evaluation of carotid-femoral pulse wave velocity; influence of timing algorithm and heart rate," *Hypertension*, vol. 45, pp. 222-226, 2005.
113. G. F. Mitchell, L. A. Moye, E. Braunwald, J.-L. Rouleau, V. Bernstein, E. M. Geltman, G. C. Flaker and M. A. Pfeffer, "Sphygmomanometrically determined pulse pressure is a powerful independent predictor of recurrent events after myocardial infarction in patients with impaired left ventricular function," *Circulation*, vol. 9, pp. 4254-4260, 1997.
114. G. F. Mitchell, H. Parise, E. J. Benjamin, M. G. Larson, M. J. Keyes, J. A. Vita, R. S. Vasan and D. Levy, "Changes in arterial stiffness and wave reflection with advancing age in healthy men and women: the framingham heart study," *Hypertension*, vol. 43, pp. 1239-1245, 2004.
115. R. Mukkamala, A. T. Reisner, H. M. Hojman, R. G. Mark, and R. J. Cohen, "Continuous cardiac output monitoring by peripheral blood pressure waveform analysis," *IEEE Trans Biomed Eng*, vol. 53, pp. 59-67, 2006.
116. J. P. Murgo, N. Westerhof, J. P. Giolma and S. A. Altobelli, "Aortic input impedance in normal man: relationship to pressure wave forms," *Circulation*, vol. 62, pp. 105-116, 1980.
117. Myers, L. J., and W. L. Capper. Exponential taper in arteries: an exact solution of its effect on blood flow velocity waveforms and impedance. *Med. Eng. Phys.* 26:147-155, 2004.
118. J. Nemcsik, J. Egresits, T. E. H. Othmane, B. C. Fekete, E. Fodor, T. Szabó, Z. Járαι, C. Jekkel, I. Kiss and A. Tislér, "Validation of Arteriograph - a new oscillometric device to measure arterial stiffness in patients on maintenance hemodialysis," *Kidney Blood Press Res*, vol. 32, pp. 223-229, 2009.

119. W. W. Nichols and M. F. O'Rourke, *McDonald's Blood Flow in Arteries: Theoretical, Experimental and Clinical Principles*, London: Hodder Arnold, 2005.
120. J. Nocedal and S. J. Wright, *Numerical Optimization*, New York : Springer, 1999.
121. A. Noordergraaf, *Circulatory System Dynamics*, New York: Academic Press, 1978.
122. M. F. O'Rourke, "Mechanical principles in arterial disease," *Hypertension*, vol. 26, pp.2-9, 1995.
123. M. F. O'Rourke, J. A. Staessen, C. Vlachopoulos, D. Duprez and G. E. Plante, "Clinical applications of arterial stiffness: definitions and reference values," *Am J Hypertens*, vol. 15, pp. 426-444, 2002.
124. B. Pannier, P. Brunel and W. El Aroussy, "Pulse pressure and echocardiographic findings in essential hypertension," *J Hypertens*, vol. 7, pp. 127-132, 1989.
125. N. Patel, M. Dodsworth and J. F. Mill, "Cardiac output measurement in newborn infants using the ultrasonic cardiac output infants using the ultrasonic cardiac output monitor: an assessment of agreement with conventional echocardiography, repeatability and new user experience," *Arch Dis Child Fetal Neonatal Ed*, 2010.
126. A. L. Pauca, M. F. O'Rourke and N. D. Kon, "Propective evaluation of a method for estimating ascending aortic pressure from the radial artery pressure waveform, " *Hypertension*, vol. 38, pp. 932-937, 2001.
127. A. C. Perrino Jr, "Cardiac output monitoring by echocardiography: should we pass on Swan-Ganz catheters," *Yale J Biol Med*, vol. 66, pp. 397-413, 1993.
128. R. Pini, M. C. Cavallini, F. Bencini, g. Silverstrini, E. Tonon, W. De Alfieri, N. Marchionni, M. Di Bari, R. B. Devereux, G. Masotti and M. J. Roman, "Cardiovascular remodeling is greater in isolated systolic hypertension than in diastolic hypertension in older adults: the insufficienza cardiaca negli anziani residenti (ICARE) a Dicomano study," *J Am Coll Cardiol*, vol. 40, pp. 1283-1289, 2002.

129. G. L. Pressman, P. M. Newgard, "A transducer for the continuous external measurement of arterial blood pressure" *IEEE Trans Biomed Electron*, vol. BME-10, pp. 73-81, 1963.
130. M. W. Rajzer, W. Wojciechowska, M. Klocek, I. Palka, M. Brzozowska-Kiszka and K. Kawecka-Jaszcz, "Comparison of aortic pulse wave velocity measured by three techniques: Complior, SphygmoCor and Arteriograph," *J Hypertens*, vol. 26, pp. 2001-2007, 2008.
131. C. H. Reinsch, "Smoothing by spline functions," *Numer Math*, vol. 10, pp. 177-183, 1967.
132. G. Rödiger, C. Prasser, C. Keyl, A. Liebold and J. Hobbhahn, "Continuous cardiac output measurement: pulse contour analysis vs thermodilution technique in cardiac surgical patients," *Br J Anaesth*, vol. 82, pp. 525-530, 1999.
133. W. J. Rogers, Y.-L. Hu, D. Coast, D. A. Vido, C. M. Kramer, R. E. Pyeritz and N. Reichek, "Age-associated changes in regional aortic pulse wave velocity," *J Am Coll Cardiol*, vol. 38, pp. 1123-1129, 2001.
134. M. J. Roman, P. S. Saba, R. Pini, M. Spitzer, T. G. Pickering, S. Rosen, M. H. Alderman and R. B. Devereux, "Parallel cardiac and vascular adaptation in hypertension," *Circulation*, vol. 86, pp. 1909-1918, 1992.
135. M. E. Safar, B. P. Pannier, P. J. Lacolley and B. I Levy, "Cardiac mass and aortic distensibility following calcium blockade in hypertension," *J Cardiovasc Pharmacol*, vol. 17(Suppl. 2), pp. S75-S80, 1991.
136. M. E. Safar, J. Blacher, B. Pannier, A. P Guerin, S. J. Marchais, P.-M. Guyonvarch'h, G. M. London, "Central pulse pressure and mortality in end-stage renal disease," *Hypertension*, vol. 39, pp. 735-738, 2002.
137. M. E. Safar, B. I. Levy, H. Struijker-Boudier, "Current perspectives on arterial stiffness and pulse pressure in hypertension and cardiovascular diseases," *Circulation*, vol. 107, pp. 2864-2869, 2003.
138. M. E. Safar, J. Blacher, A. Protogerou and A. Achimastos, "Arterial stiffness and central hemodynamics in treated hypertensive subjects according to brachial blood pressure classification," *J Hypertens*, vol. 26, pp. 130-137, 2008.

139. K. J. Salaymeh and A. Banerjee, "Evaluation of arterial stiffness in children with William syndrome: does it play a role in evolving hypertension?" *Am Heart J*, vol. 142, pp. 549–555, 2001.
140. G. G. S. Sandor, T. Hishitani, R. E. Petty, M. T. Potts, A. DeSouza, E. DeSouza and J. E. Potts, "A novel Doppler echocardiographic method of measuring the biophysical properties of the aorta in pediatric patients," *J Am Soc Echocardiogr*, vol. 16, pp. 745–750, 2003.
141. P. Segers, J. De Backer, D. Devos, S. I. Rabben, T. C. Gillebert, L. M. Van Bortel, J. De Sutter, A. De Paepe and P. R. Verdonck, "Aortic reflection coefficients and their association with global indexes of wave reflection in healthy controls and patients with Marfan's syndrome," *Am J Physiol Heart Circ Physiol* vol. 290, pp. 2385–2392, 2006.
142. P. Segers, E. R. Rietzchel, M. L. De Buyzere, D. De Bacquer, L. M. Van Bortel, G. De Backer, T. C. Gillebert and P. R. Verdonck, "Assessment of pressure wave reflection: getting the timing right," *Physiol Meas* vol. 28, pp. 1045–1056, 2007.
143. H. Senzaki, M. Akagi, T. Hishi, A. Ishizawa, M. Yanagisawa, S. Matsutani, T. Kobayashi and S. Awa, "Age-associated changes in arterial elastic properties in children," *Eur J Pediatr*, vol.161, pp. 547–551, 2002.
144. G. F. Sholler, C. M. Whight, and J. M. Celermajer, "Pulsed Doppler echocardiographic assessment, including use of aortic leaflet separation, of cardiac output in children with structural heart disease," *Am J Cardiol*, vol. 57, pp. 1195–1197, 1986.
145. G. F. Sholler, J. M. Celermajer, C. M. Whight, and A. E. Bauman, "Echo Doppler assessment of cardiac output and its relation to growth in normal infants," *Am J Cardiol*, vol. 60, pp. 1112–1116, 1987.
146. C. Slagt, J. Beute, M. Hoeksema, I. Malagon, J.-W. R. Mulder and J. A. B. Groeneveld, "Cardiac output derived from arterial pressure waveform analysis without calibration vs. thermodilution in septic shock: evolving accuracy of software versions," *Eur J Anaesthesiol*, vol. 27, pp. 550–554, 2010.
147. H. Smulyan, D. S. Siddiqui, R. J. Carlson, G. M. London and M. E. Safar, "Clinical utility of aortic pulses and pressures calculated from

- applanated radial-artery pulses,” *Hypertension*, vol. 42, pp. 150-155, 2003.
148. H. Smulyan, P. R. Sheehe and M. E. Safar ME, “A preliminary evaluation of the mean arterial pressure as measured by cuff oscillometry,” *Am J Hypertens*, vol. 21, pp. 166-171, 2008.
149. S. Söderström, G. Nyberg, M. F. O’Rourke, J. Sellgren and J. Pontén, “Can a clinically useful aortic pressure wave be derived from a radial pressure wave?” *Br J Anaesth*, vol. 88, pp. 481-488, 2002.
150. R. W. Stadler, W. C. Karl and R. S. Lees, “New methods for arterial diameter measurement from B-mode images,” *Ultrasound Med Biol*, vol. 22, pp. 25-34, 1996.
151. R. W. Stadler, J. A. Taylor and R. S. Lees, “Comparison of B-mode, M-mode and echo-tracking methods for measurement of the arterial distension waveform,” *Ultrasound Med Biol*, vol. 23, pp. 879-887, 1997.
152. C. W. Stetz, R. G. Miller, G. E. Kelly, and T. A. Raffin, “Reliability of the thermodilution method in the determination of cardiac output in clinical practice,” *Am Rev Respir Dis*, vol. 126, pp. 1001-1004, 1982.
153. P. Studinger, Z. Lénárd, R. Reneman and M. Kollai, “Measurement of aortic arch distension wave with the echo-track technique,” *Ultrasound Med Biol*, vol. 26, pp. 1285-1291, 2000.
154. K. Sutton-Tyrrell, S. S. Najjar, R. M. Boudreau, L. Venkitachalam, V. Kupelian, E. M. Simonsick, R. Havlik, E. G. Lakatta, H. Spurgeon, S. Kritchevsky, M. Pahor, D. Bauer and A. Newman, “Elevated aortic pulse wave velocity, a marker of arterial stiffness, predicts cardiovascular events in well-functioning older adults,” *Circulation*, vol. 111, pp. 3384-3390, 2005.
155. G. Swamy and R. Mukkamala, “Estimation of the aortic pressure waveform and beat-to-beat relative cardiac output changes from multiple peripheral artery pressure waveforms,” *IEEE Trans Biomed Eng*, vol. 55, pp. 1521-1529, 2008.
156. K. Tachibana, H. Imanaka, M. Takeuchi, Y. Takauchi, H. Miyano and M. Nishimura, “Noninvasive cardiac output measurement using partial carbon dioxide rebreathing is less accurate at settings of reduced

- minute ventilation and when spontaneous breathing is present,” *Anesthesiology*, vol. 98, pp.830-837, 2003.
157. H. L. Tan, M. Pinder, R. Parsons, B. Roberts and P. V. van Heerden, “Clinical evaluation of USCOM ultrasonic cardiac output monitor in cardiac surgical patients in intensive care unit,” *Br J Anaesth*, vol. 94, pp. 287-291, 2005.
 158. G. A. Tannenbaum, D. Mathews and C. Weissman, “Pulse contour cardiac output in surgical intensive care unit patients,” *J Clin Anesth*, vol. 5, pp. 471-478, 1993.
 159. B. Trachet, P. Reymond, J. Kips, A. Swillens, M. De Buyzere, B. Suys, N. Stergiopoulos and P. Segers, “Numerical validation of a new method to assess aortic pulse wave velocity from a single recording of a brachial artery waveform with an occluding cuff,” *Ann Biomed Eng*, vol. 38, pp. 876-888, 2010.
 160. S. M. Toy , J. Melbin and A. Noordergraaf, “Reduced models of arterial systems,” *IEEE Trans Biomed Eng*, vol. 32, pp. 174-176, 1985.
 161. L. M. Van Bortel, E. J. Balkestein, J. J. van der Heijden-Spek, F. H. Vanmolkot, J. A. Staessen, J. A. Kragten, J. W. Vredeveld, M. E. Safar, H. A. Struijker Boudier and A. P. Hoeks, “Non-invasive assessment of local arterial pulse pressure: comparison of applanation tonometry and echo-tracking,” *J Hypertens*, vol. 19, pp. 1037-1044, 2001.
 162. J. J. van der Heijden-Spek, J. A. Staessen, R. H. Fagard, A. P. Hoeks, H. A. Struijker Boudier and L. M. Van Bortel, “Effect of age on brachial artery wall properties differs from the aorta and is gender dependent: a population study,” *Hypertension*, vol. 35, pp. 637-642, 2000.
 163. S. Van Huffel and J. Vandewalle, *The total least squares problem: computation aspects and analysis*, Philadelphia: SIAM, 1991.
 164. L. E. M. van Lelyveld-Haas, A. R. H. van Zanten, G. F. Borm and D. H. T. Tjan, “Clinical validation of the non-invasive cardiac output monitor USCOM-IA in critically ill patients,” *Eur J Anaesthesiol*, vol. 25, pp. 917-924, 2008.

165. P. Van Overschee and B. De Moor, "N4SID: Subspace algorithms for the identification of combined deterministic-stochastic systems," *Automatica*, vol.30, pp. 75–93, 1994.
166. S. J. Vermeersch, E. R. Rietzschel, M. L. De Buyzere, D. De Bacquer, G. De Backer, L. M. Van Bortel, T. C. Gillebert, P. R. Verdonck and P. Segers, "Determining carotid artery pressure from scaled diameter waveforms: comparison and validation of calibration techniques in 2026 subjects," *Physiol Meas*, vol. 29, pp. 1267-1280, 2008.
167. F. Verbeke, W. Van Biesen, P. Peeters, L. M. Van Bortel and R. C. Vanholder, "Arterial stiffness and wave reflections in renal transplant recipients," *Nephrol Dial Trasplant*, vol. 22, pp. 3021-3027, 2007.
168. T. K. Waddell, A. M. Dart, T. L. Medley, J. D. Cameron, B. A. Kingwell, "Carotid pressure is a better predictor of coronary artery disease severity than brachial pressure," *Hypertension*, vol. 38, pp. 927-931, 2001.
169. F. J. Walther, B. Siassi, N. A. Ramadan, A. K. Ananda, and P. Y. K. Wu, "Pulsed Doppler determinations of cardiac output in neonates: normal standards for clinical use", *Pediatrics*, vol. 76, pp. 829–833, 1985.
170. H. R. Warner, H. J. C. Swan, D. C. Connolly, R. G. Tompkins and E. H. Wood, "Quantitation of beat-to-beat changes in stroke volume from the aortic pulse contour in man," *J Appl Physiol*, vol. 5, pp. 495-507, 1953.
171. H. Watanabe, M. Kawai, T. Sibata, M. Hara, H. Furuhashi and S. Mochizuki, "Noninvasive measurement of aortic pressure waveform by ultrasound," *Heart Vessels*, vol. 13, pp. 79-86, 1998.
172. K. H. Wesseling, B. de Wit, J. A. P. Weber and N. T. Smith, "A simple device for the continuous measurement of the cardiac output," *Adv Cardiovasc Phys*, vol. 5, pp. 16-52, 1983.
173. K. H. Wesseling, J. R. C. Jansen, J. J. Settels, and J. J. Schreuder, "Computation of aortic flow from pressure in humans using a nonlinear, three-element model," *J Appl Physiol*, vol. 74, pp. 2566–2573, 1993.

- 174. W. White, A. Berson, C. Robbins, M. Jamieson, L. Prisant, E. Roccella E and S. Sheps, "National standard for measurement of resting and ambulatory blood pressures with automated sphygmomanometers," *Hypertension*, vol. 21, pp. 504-509, 1993.
- 175. L. Xie and L. Ljung, "Estimate physical parameters by black-box modeling," in *Proc. 21st Chinese Control Conf.*, 2002, pp. 673-677.
- 176. K. Yamashita, T. Nishiyama, T. Yokoyama, H. Abe and M. Manabe, "Effects of vasodilation on cardiac output measured by pulseCO," *J Clin Monit Comput*, vol. 21, pp. 335-339, 2007.
- 177. M. Zamir, *The Physics of Pulsatile Flow*. New York: Springer-Verlag, 2005.

Appendix A

The Analogy between a Transmission Line and an Elastic Tube with Incompressible Flow

Pulsatile flow inside an elastic tube is governed by the Navier-Stokes equations. To derive the most general form of the Navier-stokes equations, two assumptions are made. First, it is assumed that the fluid is Newtonian, which means the velocity gradient inside the fluid is linearly related to the shear stress. It has been a long-standing debate whether blood is a Newtonian fluid. However, it has been shown that treating blood as a Newtonian fluid is adequate for the study of global dynamics of the circulation and the heart [177].

Second, it is assumed that the flow is laminar, which means the fluid elements only move in the direction of the flow, which is parallel to the axis of the tube. Blood flow is not always laminar inside the cardiovascular circulation. However, at the higher levels of the vascular tree, blood flow is mostly laminar [177].

The derivation of the most general form of the Navier-Stokes equations based on cylindrical coordinates is described in [177].

These equations can be further simplified into the one-dimensional Navier-Stokes equations given below. The derivation is also described in [177].

The equations describing a transmission line are given by:

$$-\frac{\partial V(x,t)}{\partial x} = RI(x,t) + L\frac{\partial I(x,t)}{\partial t} \quad (\text{A.1})$$

$$-\frac{\partial I(x,t)}{\partial x} = C\frac{\partial V(x,t)}{\partial t} \quad (\text{A.2})$$

where V is voltage, I is current, R is the line resistance, L is the line inductance, C is the line capacitance, and x and t are the spatial and temporal variables respectively.

Equations (A.1) and (A.2) are analogous to the one-dimensional Navier-Stokes equations describing pulsatile incompressible flow in an elastic tube, which are given by [177]:

$$-\frac{\partial P(x,t)}{\partial x} = R'Q(x,t) + \frac{\rho}{A} \frac{\partial Q(x,t)}{\partial t} \quad (\text{A.3})$$

$$-\frac{\partial Q(x,t)}{\partial x} = \frac{\partial A}{\partial P} \frac{\partial P(x,t)}{\partial t} \quad (\text{A.4})$$

where P is pressure, Q is flow, ρ is liquid density, A is the cross-sectional area of the tube, and R' is a resistive term dependent on the lumen area, and wall and liquid viscosity.

By comparing these two sets of equations, it can be seen that voltage corresponds to pressure, current corresponds to flow, line resistance corresponds to the resistive term R' , line inductance corresponds to ρ/A , and line capacitance corresponds to $\partial A/\partial P$. In addition, if the transmission line is terminated by a complex load (Figure 2.1), then the terminating condition is given by:

$$\left(C_L + C_L \frac{R_L}{R_T}\right) \frac{dV(l,t)}{dt} + \frac{V(l,t)}{R_P} = I + C_L R_L \frac{dI(l,t)}{dt} \quad (\text{A.5})$$

where C_L is the load capacitance, R_L is the load resistance, R_T is the terminating resistance and l is the length of the line.

Appendix B

Implementation of the Transmission Line Model using the Finite Element Method

The transmission line equations can be solved numerically using a finite element method [96]. The line is divided into a finite number of elements. Each element has points called interpolation nodes. The voltage and current are evaluated only at a finite number of nodes. Each voltage node is placed between two current nodes and each current node is placed between two voltage nodes. The leap-frog scheme is implemented to evaluate the voltage and current at certain time steps. The voltage is evaluated at half a time step before and after the current. Applying the finite element method to transmission line equations (A.1) and (A.2) gives the following equations:

$$I_j^{n+\frac{1}{2}} = K_1 I_j^{n-\frac{1}{2}} - K_2 (V_{i+1}^n - V_i^n) \quad (\text{B.1})$$

$$V_j^{n+1} = K_3 V_i^n - K_4 (I_{j+1}^{n+\frac{1}{2}} - I_j^{n+\frac{1}{2}}) \quad (\text{B.2})$$

where i and j indicate the nodes and n indicates the time step. K_1 to K_4 are given by:

$$K_1 = 1 \quad (\text{B.3})$$

$$K_2 = \frac{\Delta t}{L \Delta x} \quad (\text{B.4})$$

$$K_3 = 1 \quad (\text{B.5})$$

$$K_4 = \frac{\Delta t}{C \Delta x} \quad (\text{B.6})$$

For numerical stability, we require

$$u \leq \frac{\Delta x}{\Delta t} \quad (\text{B.7})$$

where u is the wave propagation speed. The terminating condition (A.5) is approximated as follows:

$$A_5 V_m^{n+1} = A_3 I_p^{n+\frac{1}{2}} + A_4 \frac{I_p^{n+\frac{1}{2}} - I_p^{n-\frac{1}{2}}}{\Delta t} + A_6 V_m^n \quad (\text{B.8})$$

where m indicates the last voltage node and p indicates the last current node. The last current node is located before the last voltage node. A_1 to A_6 are given as follows:

$$A_1 = C_L + C_L \frac{R_L}{R_T} \quad (\text{B.9})$$

$$A_2 = \frac{1}{R_T} \quad (\text{B.10})$$

$$A_3 = 1 \quad (\text{B.11})$$

$$A_4 = C_L R_L \quad (\text{B.12})$$

$$A_5 = \frac{A_1}{\Delta t} + \frac{A_2}{2} \quad (\text{B.13})$$

$$A_6 = \frac{A_1}{\Delta t} - \frac{A_2}{2} \quad (\text{B.14})$$

Appendix C

The Derivation of the Transfer Function from the Ascending Aortic Flow to the Radial Artery Pressure

For a uniform lossless transmission line,

$$P_o = P_i + P_r \quad (C.1)$$

$$Q_o = \frac{1}{Z_{ch}}(P_i - P_r) \quad (C.2)$$

$$P_t = P_i z^{-d} + P_r z^d \quad (C.3)$$

where P_o is the pressure at the beginning of the line, P_i is the incident wave at the beginning of the line, P_r is the reflected wave at the beginning of the line, Q_o is the flow at the beginning of the line, Z_{ch} is the characteristic impedance of the line, P_t is the pressure at the end of the line, n is the discrete time delay for the wave to travel from the beginning to the end of the line, z is the z -variable.

P_i and P_r are related by the wave reflection coefficient at the tube-load interface Γ as:

$$\Gamma = \frac{P_r z^d}{P_i z^{-d}} \quad (C.4)$$

Using equations (C.2)-(C.4), the transfer function ($M(z)$) from Q_o to P_t is then given by:

$$M(z) = \frac{P_t}{Q_o} = \frac{Z_{ch}(1 + \Gamma)z^n}{z^{2n} - \Gamma} \quad (C.5)$$

Γ is given by:

$$\Gamma = \frac{Z_L - Z_{ch}}{Z_L + Z_{ch}} \quad (C.6)$$

where Z_L is the impedance of the terminating load.

In terms on the s -variable (continuous-time), Z_L is given by:

$$Z_L = \frac{1 + C_L R_L s}{\frac{1}{R_T} + (C_L + \frac{C_L R_L}{R_T})s} \quad (C.7)$$

The s -variable is replaced by the z -variable (discrete-time) using the following approximation:

$$s = \frac{2F_s(z - 1)}{(z + 1)} \quad (C.8)$$

where F_s is the sampling frequency. Then Z_L is given by:

$$Z_L = \frac{A_Z z + B_Z}{C_Z z + D_Z} \quad (C.9)$$

where

$$A_Z = 1 + 2F_s C_L R_L \quad (C.10)$$

$$B_Z = 1 - 2F_s C_L R_L \quad (C.11)$$

$$C_Z = \frac{1}{R_T} + 2F_s (C_L + C_L \frac{R_L}{R_T}) \quad (C.12)$$

$$D_Z = \frac{1}{R_T} - 2F_s (C_L + C_L \frac{R_L}{R_T}) \quad (C.13)$$

Using equations (C.6), (C.9)-(C.13), Γ can be written as:

$$\Gamma = \frac{A_r z + B_r}{C_r z + D_r} \quad (C.14)$$

where

$$A_r = A_Z - Z_{ch} C_Z \quad (C.15)$$

$$B_r = B_Z - Z_{ch} D_Z \quad (C.16)$$

$$C_r = A_Z + Z_{ch} C_Z \quad (C.17)$$

$$D_r = B_Z + Z_{ch} D_Z \quad (C.18)$$

Using equations (C.5), (C.14)-(C.18), $M(z)$ can be written as:

$$M(z) = \frac{A_M z^{d+1} + B_M z^d}{C_M z^{2d+1} + D_M z^{2d} + E_M z + F_M} \quad (C.19)$$

where

$$A_M = Z_{ch}(A_r + C_r) \quad (C.20)$$

$$B_M = Z_{ch}(B_r + D_r) \quad (C.21)$$

$$C_M = C_r \quad (C.22)$$

$$D_M = D_r \quad (C.23)$$

$$E_M = -A_r \quad (C.24)$$

$$F_M = -B_r \quad (C.25)$$

In terms of C_L , R_L and R_T , equations (C.20)-(C.25) are given by:

$$A_M = 2Z_{ch}(1 + 2F_s C_L R_L) \quad (C.26)$$

$$B_M = 2Z_{ch}(1 - 2F_s C_L R_L) \quad (C.27)$$

$$C_M = \frac{Z_{ch}}{R_T} + 1 + 2F_s C_L (R_L + Z_{ch} + \frac{R_L Z_{ch}}{R_T}) \quad (C.28)$$

$$D_M = \frac{Z_{ch}}{R_T} + 1 - 2F_s C_L (R_L + Z_{ch} + \frac{R_L Z_{ch}}{R_T}) \quad (C.29)$$

$$E_M = \frac{Z_{ch}}{R_T} - 1 - 2F_s C_L (R_L - Z_{ch} - \frac{R_L Z_{ch}}{R_T}) \quad (C.30)$$

$$F_M = \frac{Z_{ch}}{R_T} - 1 + 2F_s C_L (R_L - Z_{ch} - \frac{R_L Z_{ch}}{R_T}) \quad (C.31)$$

$M(z)$ can also be written in the more common form as

$$M(z) = \frac{b_1 z^{-d} + b_2 z^{-d-1}}{1 + a_1 z^{-1} + a_2^{-2d} + a_3^{-2d-1}} \quad (C.32)$$

with

$$b_1 = \frac{2Z_{ch}(1 + 2F_s C_L R_L)}{\frac{Z_{ch}}{R_T} + 1 + 2F_s C_L (R_L + Z_{ch} + \frac{R_L Z_{ch}}{R_T})} \quad (C.33)$$

$$b_2 = \frac{2Z_{ch}(1 - 2F_s C_L R_L)}{\frac{Z_{ch}}{R_T} + 1 + 2F_s C_L (R_L + Z_{ch} + \frac{R_L Z_{ch}}{R_T})} \quad (C.34)$$

$$a_1 = \frac{\frac{Z_{ch}}{R_T} + 1 - 2F_s C_L (R_L + Z_{ch} + \frac{R_L Z_{ch}}{R_T})}{\frac{Z_{ch}}{R_T} + 1 + 2F_s C_L (R_L + Z_{ch} + \frac{R_L Z_{ch}}{R_T})} \quad (C.35)$$

$$a_2 = \frac{\frac{Z_{ch}}{R_T} - 1 - 2F_s C_L (R_L - Z_{ch} - \frac{R_L Z_{ch}}{R_T})}{\frac{Z_{ch}}{R_T} + 1 + 2F_s C_L (R_L + Z_{ch} + \frac{R_L Z_{ch}}{R_T})} \quad (C.36)$$

$$a_3 = \frac{\frac{Z_{ch}}{R_T} - 1 + 2F_s C_L (R_L - Z_{ch} - \frac{R_L Z_{ch}}{R_T})}{\frac{Z_{ch}}{R_T} + 1 + 2F_s C_L (R_L + Z_{ch} + \frac{R_L Z_{ch}}{R_T})} \quad (C.37)$$